Title

Simultaneous Quantitative Multiparametric MRI for In Vivo Tissue Characterization using Magnetic Resonance Multitasking: Methodology and Clinical Experience

Permalink

https://escholarship.org/uc/item/0d5369hr

Author

Ma, Sen

Publication Date

2020

UNIVERSITY OF CALIFORNIA
Los Angeles

Simultaneous Quantitative Multiparametric MRI for In Vivo Tissue Characterization using Magnetic Resonance Multitasking: Methodology and Clinical Experience

A dissertation submitted in partial satisfaction of the
requirements for the degree Doctor of Philosophy
in Bioengineering

by

Sen Ma

2020

ABSTRACT OF THE DISSERTATION

Simultaneous Quantitative Multiparametric MRI for In Vivo Tissue Characterization using Magnetic Resonance Multitasking: Methodology and Clinical Experience

by

Sen Ma
Doctor of Philosophy in Department of Bioengnieering
University of California, Los Angeles, 2020
Professor Debiao Li, Chair

In current clinical systems, magnetic resonance imaging scans for disease diagnosis and prognosis are dominated by qualitative contrast-weighted imaging. These qualitative MR images reveal regional differences in signal intensities between tissues with focal structural or functional abnormalities and tissues that are supposedly in healthy states, facilitating subjective determination for disease diagnosis. The administration of gadolinium-based contrast agents is prevalent in clinical MRI exams, which alternates the relaxation time of neighboring water protons and creates enhanced signal intensities from damaged tissues with high vascular density and thin vessel wall for better visualization. Nowadays, nearly 50% of the MRI studies were conducted with contrast agents. However, patients with renal insufficiency are at risk of developing nephrogenic system fibrosis if exposed to gadolinium-based contrast agents, and chronic toxic effects of possible gadolinium retention have been reported. In the meantime, qualitative contrast-weighted images have limited sensitivity to subtle alteration in tissue states, lack of biological specificity and multi-center reproducibility, and limited predictive values.

One promising alternative is quantitative multiparametric MRI, which contains various methods to quantify multiple parameters with interpretable physical units that are intrinsic to tissue properties. Most of these quantitative approaches do not involve the administration of contrast agents, therefore ensuring the safety of the application to a wide range of patients and reducing the costs of MRI. These quantitative parameters are highly reproducible, sensitive to subtle physiological tissue changes, and specific for disease pathologies. More importantly, each of these parameters reveal tissue properties in different aspects, having the potential to offer complementary information for comprehensive tissue characterization, and acting as biomarkers that are directly associated with diseases states. Despite the benefits to clinical studies, quantitative multiparametric MRI has yet to be widely adopted in routine clinical practices because of several major technical limitations including (i) long scan times that compromises image resolution and/or spatial coverage, (ii) motion artifacts, (iii) misaligned parametric maps due to separate acquisitions, and (iv) complicated clinical workflow. This dissertation aims to address some of these challenges by proposing a simultaneous quantitative multiparametric MRI approach with Magnetic Resonance Multitasking and focus on the quantification of T1, T2, T1ρ, and ADC, which serves as the start of the ultimate goal to provide a clinically translatable, multiparametric whole-body quantitative tissue characterization technique.

A novel approach to simultaneously quantifying T1, T2, and ADC in the brain was first developed using MR Multitasking in conjunction with a time-resolved phase correction strategy to compensate for the inter-shot phase inconsistencies introduced by physiological motion. It was implemented as a push-button, continuous acquisition that simplified the workflow. This technique was initially demonstrated in healthy subjects to efficiently produce distortion-free, co-registered T1, T2, and ADC maps with 3D brain coverage (100mm) in 9.3min. The resulting T1, T2, and

ADC measurements in the brain were comparable to reference quantitative approaches. Abrupt motion was manually identified and removed to yield T1, T2, and ADC maps that were free from motion artifacts and with accurate quantitative measurements. Clinical feasibility was demonstrated on post-surgery glioblastoma patients.

A motion-resolved, simultaneous T1, T2, and T1ρ quantification technique was then developed using MR Multitasking in a push-button 9min acquisition. Rigid intra-scan head motion was captured and simultaneously resolved along with the relaxation processes. This technique was first validated in healthy subjects to produce high quality, whole-brain (140mm) T1, T2, and T1ρ maps and repeatable T1, T2, and T1ρ measurements that were in excellent agreement with gold standard methods. Motion-resolved, artifact-free maps were generated under either in-plane or through-plane motion, which provided a novel avenue for handling rigid motion in brain MRI. Synthetic contrast-weighted qualitative images comparable to clinical images were generated using the parameter maps, demonstrating the significant potential to replace conventional MRI scans with a single Multitasking scan for clinical purposes. This technique was applied in a pilot clinical setting to perform tissue characterization in relapsing-remitting multiple sclerosis patients. The combination of T1, T2, and T1ρ significantly improved the accuracy of the differentiation of multiple sclerosis patients from healthy controls, compared to either single parameter alone, indicating the clinical utility of T1, T2, and T1ρ as quantitative biomarkers.

Lastly, the above two quantitative techniques were extended to other body organs for a preliminary demonstration of potential applications, where we 1) simultaneously quantified T1, T2, and ADC in the breast with whole-breast coverage (160mm) in 8min, incorporating a B1+-compensated multiparametric fitting approach to address the notable B1+ inhomogeneity across the bilateral breast FOV, and to provide distortion-free, co-registered whole-breast T1, T2, and

ADC maps with good in vivo repeatability; and 2) simultaneously quantified myocardial T1 and T1ρ in a single non-ECG, free-breathing acquisition, where cardiac motion and respiratory motion were retrospectively identified and simultaneously resolved to produce dynamic myocardial T1 and T1ρ maps of 20 cardiac phases with high temporal resolution (15ms) in a single, continuous acquisition of 1.5min per slice. Multitasking T1 and T1ρ measurements in the heart were comparable with gold standard techniques.

The dissertation of Sen Ma is approved.

Zhaoyang Fan

Peng Hu

Holden H. Wu

Debiao Li, Committee Chair

University of California, Los Angeles

2020

Dedicated to the ones I love,
who have unconditionally supported me
throughout my graduate studies:

My lovely parents: Yusheng Ma & Yueru Kang
My dear wife: Nan Wang

TABLE OF CONTENTS

LIST OF ABBREBIATIONS

Physics

T – tesla

mT – millitesla

m – meter

mm – millimeter

s – second

ms – millisecond

min – minute

Hz – hertz

Statistics

ICC – intra-class correlation coefficient

R – Pearson correlation coefficient

p – statistical significance

ANOVA – analysis of variance

ROC – receiver operator curve

AUC – area under the curve

CI – confidence interval

Mathematics

SVD – singular value decomposition

HOSVD – high-order singular value decomposition

ADMM – alternating direction method of multipliers

LRT – low-rank tensor

CBD – constrained blind deconvolution

Medicine

ECG – electrocardiogram

bpm – beats per minute

MTR – magnetic transfer rate

PDFF – proton density fat fraction

NSF – nephrogenic system fibrosis

MS – multiple sclerosis

RRMS – relapsing remitting multiple sclerosis

WM – white matter

GM – gray matter

CSF – cerebrospinal fluid

NAWM – normal appearing white matter

NAGM – normal appearing gray matter

Magnetic Resonance Imaging

MRI – magnetic resonance imaging

NMR – nuclear magnetic resonance

2D/3D – two dimension/three dimension

SNR – signal-to-noise ratio

CNR – contrast-to-noise ratio

FOV – field of view

RF – radiofrequency

B0 – main magnetic field

B1 – excitation radiofrequency field

B1+ – transmit excitation radiofrequency field

BIR – B1 insensitive rotation

TR – repetition time

TE – echo time

TI – inversion time

TM – mixing time

TSL – spin-lock time

FSL – spin-lock frequency

T1w – T1-weighted

T2w – T2-weighted

T1ρw – T1ρ-weighted

PD – proton density

PDw – proton density-weighted

DWI – diffusion-weighted imaging

ADC – apparent diffusion coefficient

SWI – susceptibility-weighted imaging

QSM – quantitative susceptibility mapping

DCE – dynamic contrast-enhanced

IR – inversion recovery

FLAIR – fluid attenuated inversion recovery

STIR – short-TI inversion recovery

DIR – double inversion recovery

SR – saturation recovery

DW-SSEPI – diffusion-weighed single-shot echo planar imaging

DW-RSEPI – diffusion-weighted readout-segmented echo planar imaging

ME– multi echo

SE – spin echo

TSE – turbo spin echo

FLASH – fast low angle shot

GRE – gradient echo

bSSFP – balanced steady-state free precession

MPRAGE – magnetization-prepared rapid gradient echo

T2-prep – T2 preparation

D-prep – diffusion preparation

T1ρ-prep – T1ρ preparation

T1ρ-FLASH – T1ρ-prepared fast low angle shot

T2-IR – T2 preparation/inversion recovery

T1ρ-IR – T1ρ preparation/inversion recovery

Techniques

MLEV – Malcom-Levitt

DESPOT1/DESPOT2 – driven equilibrium single pulse observation of T1/T2

MRF – magnetic resonance fingerprinting

MR Multitasking – magnetic resonance multitasking

DESS – dual-echo steady state

STEM – stimulated echo-based mapping

ZEBRA – Z-locations shuffling, multiple echoes, and b-interleaving for relaxometry diffusion acquisition

RESOLVE – readout segmentation of long variable echo trains

GRAPPA – generalized auto-calibrating partially parallel acquisitions

MOLLI – modified look-locker inversion recovery

shMOLLI – shortened MOLLI

SASHA – saturation recovery single shot acquisition

3D-QALAS – 3D-quantification using an interleaved Look-Locker acquisition sequence with T2 preparation pulse

CINE – cinematic imaging

CAIPIRINHA – controlled aliasing in parallel imaging results in higher acceleration

ESPIRiT – an eigenvalue approach for iterative self-consistent parallel imaging reconstruction from arbitrary k-space

Others

IRB – institutional review board

ISMRM – International Society for Magnetic Resonance in Medicine

NIST – National Institute of Standards and Technology

LIST OF TABLES

LIST OF FIGURES

ACKNOWLEDGEMENTS

It is my great honor and privilege to have Dr. Debiao Li as my PhD advisor. I would like to extend my deepest gratitude for his mentorship, guidance, and endless support throughout my entire graduate study. I am mostly grateful for the sufficient research resources that Dr. Li provided, including unlimited access to the MR scanners and clinical collaboration with radiologists and clinicians. Dr. Li's extensive experience and solid background in the field of MR research has assisted me to tackle many challenges on my projects. I benefited from numerous discussions in the collaborative and resourceful research environment that Dr. Li built in the Biomedical Imaging Research Institute (BIRI). Dr. Li's pursuit in academic excellence, his insightful vision, and his work attitude has influenced me beyond research and will certainly benefit my career after my PhD program.

I would also like to thank my doctoral committee, Dr. Zhaoyang Fan, Dr. Peng Hu, and Dr. Holden Wu for their valuable advice and instructions on my thesis and defense. Thanks to Dr. Daniel B. Ennis as well who served as my committee co-chair during my oral qualifying exam.

My special and sincerest appreciation goes to Dr. Anthony G. Christodoulou who mentored me even before both of us joined Dr. Li's group – in 2014 when I was conducting summer research activities at the University of Illinois at Urbana-Champaign. Dr. Christodoulou has provided more than enough assistance of signal processing, image reconstruction, and clarification on every aspect of MR Multitasking whenever I sought for them. Not only did I greatly benefit from his technical expertise, but also his excellent communication skills with extreme efficiency and patience – making him the first person I would consult when I needed. He is a respectful mentor, a trustworthy colleague, and a dear friend.

I am also deeply grateful to Dr. Christopher Nguyen who co-mentored me with Dr. Li since I joined the lab and guided me into the field of MR research. My first project was diffusion MRI reconstruction on which Dr. Nguyen shared his extensive knowledge and provided me hands-on experience of operating an MRI scanner. Moreover, Dr. Nguyen always encouraged me on critical and independent thinking, shared his experience on how to make research plans efficiently, and instructed me on grant writing and presentation, all of which were crucial aspects from which I greatly benefited throughout my PhD career after he left for Harvard Medical School. I sincerely hope he has a bright and successful career in academia.

Many thanks to our onsite Siemens scientists Dr. Xiaoming Bi and Dr. Fei Han, who provided me essential and critical aid on Siemens pulse sequence programming. Discussions with these intelligent scientists have greatly facilitated my research with substantial efficiency.

It has been my great pleasure to work with the entire BIRI group of talented researchers and friendly and helpful staffs, including but not limited to my fellow graduate students (Nan Wang (who joined the lab with me at the same time and became my wife eventually!), Yuhua Chen, Pei Han, Zhehao Hu, Tianle Cao, Xingmin Guan, Eric Johnson, Xinheng Zhang), past students (Dr. Zhengwei Zhou, Dr. Zixin Deng, Dr. Jaime Shaw), faculties (Dr. Zhaoyang Fan, Dr. Yibin Xie, Dr. Anthony G. Christodoulou, Dr. Randy Yang), MRI technologists (Edward Gill, Laura Smith, Jerry Zink), and support research staffs (Joselyn Ricafrente, Laura Chey, Amy Hoang, Eileen Da Vido, Johanna Kim, Joceline Mota, Grant Dagliyan, Natalin Aroyan). I specifically acknowledge Nan Wang and Tianle Cao for providing two figures for the demonstration of T2* and fat fraction in this dissertation.

Lastly, I am deeply indebted to my family – my lovely parents, Yusheng Ma and Yueru Kang, who have given me unconditional support during my PhD career, and my dear wife, Nan

Wang, whose love accompanied me in every precious moment of the past five years, and whose talent and creativity sparkled me in many aspects of my research. We joined the lab as strangers, and graduate as a dear couple.

VITA

Education:

- M.S., Department of Electrical Engineering, University of California, Los Angeles (2016)
- B.S., Department of Electrical Engineering, Tsinghua University, Beijing, China (2015)

Selected Journal Publications

- **Ma S**, Nguyen CT, Han F, Wang N, Deng Z, Binesh N, Moser FG, Christodoulou AG, Li D. Three-Dimensional Simultaneous Brain T1, T2, and Apparent Diffusion Coefficient Mapping with MR Multitasking. Magnetic Resonance in Medicine 2019;84(1): 72-88. DOI: 10.1002/mrm.28092.
- **Ma S**, Nguyen CT, Christodoulou AG, Luthringer D, Kobashigawa J, Lee S.-E, Chang H.-J, Li D. Accelerated Cardiac Diffusion Tensor Imaging Using Joint Low-Rank and Sparsity Constraints. IEEE Transactions in Biomedical Engineering 2018;65(10): 2219-2230. DOI: 10.1109/TBME.2017.2787111.
- **Ma S**, Wang N, Fan Z, Kaisey M, Sicotte NL, Christodoulou AG, Li D. Three-Dimensional Whole-Brain Simultaneous T1, T2, and T1ρ Quantification using MR Multitasking: Method and Initial Clinical Experience in Tissue Characterization of Multiple Sclerosis. Magnetic Resonance in Medicine. Under Review.
- **Ma S**, Wang N, Christodoulou AG, Li D. Motion-Resolved Imaging in Brain MRI with MR Multitasking: An Initial Study in Simultaneous Multiparametric Mapping. Magnetic Resonance in Medicine. In Preparation.

Selected Conference Abstracts

- **Ma S**, Christodoulou AG, Wang N, Kaisey M, Sicotte NL, Li D. Motion-Resolved, 3D Whole-Brain Simultaneous T1, T2, and T1ρ Mapping using Multitasking with Application to Multiple Sclerosis: A Pilot Study. In Proceedings of the 28th Annual Meeting of ISMRM, Paris, France, 2020. Abstract 6598. Oral Presentation.
- **Ma S**, Christodoulou AG, Wang N, Li D. Rapid 3D B1+-Compensated, Simultaneous Whole Breast T1, T2, and Apparent Diffusion Coefficient Quantification with MR Multitasking. In Proceedings of the 28th Annual Meeting of ISMRM, Paris, France, 2020. Abstract 4831. Digital Poster Presentation.
- Serry FM, **Ma S**, Li D, Christodoulou AG. Dual Flip-angle IR-FLASH for B1+ insensitive T1 Mapping: Application to T1 CMR Multitasking. In Proceedings of the 28th Annual Meeting of ISMRM, Paris, France, 2020. Abstract 2336. Oral Presentation.
- Cao T, Christodoulou AG, Wang N, **Ma S**, Xie Y, Gharabaghi S, Haacke EM, Li D. Simultaneous Quantitative Mapping of T1, T2*, and Susceptibility with Magnetic Resonance Multitasking. In Proceedings of the 28th Annual Meeting of ISMRM, Paris, France, 2020. Oral Presentation.
- **Ma S**, Christodoulou AG, Nguyen C, Han F, Wang N, Xie Y, Li D. Three-Dimensional Whole Brain Simultaneous T1, T2, and Apparent Diffusion Coefficient Mapping Using

MR Multitasking. In Proceedings of the 27th Annual Meeting of ISMRM, Montreal, Canada, 2019. Abstract 5416. Oral Presentation.

- **Ma S**, Nguyen C, Christodoulou AG, Lee SE, Chang HJ, Li D. Sparsely Sampled Cardiac Diffusion Tensor Imaging Using Phase-Corrected Joint Low-Rank and Sparsity Constraints. In Proceedings of the 26th Annual Meeting of ISMRM, Paris, France, 2018. Abstract 6436. Digital Poster Presentation.
- Nguyen CT, Christodoulou AG, Zhang N, **Ma S**, Deng Z, Fan Z, Li D. Preliminary Comparison between Intravoxel Incoherent Motion (IVIM) imaging with Quantitative Myocardial First Pass Perfusion (FPP) and Extracellular Volume (ECV) Mapping. CMR 2018, Barcelona, Spain, 2018. Abstract 378861. Digital Poster Presentation.
- **Ma S**, Nguyen C, Christodoulou AG, Luthringer D, Kobashigawa J, Li D. Accelerated Cardiac Diffusion Tensor Imaging Using a Joint Low-Rank and Sparsity Constraint. In Proceedings of the 25th Annual Meeting of ISMRM, Honolulu, HI, USA, 2017. Abstract 6603. Oral Presentation.
- Nguyen CT, **Ma S**, Bi X, Li D. Towards High Success Rate in vivo Cardiac DTI on a Clinical 3T Scanner: Considerations on Heart Rate, Body-to-Mass Index, and Free Breathing. In Proceedings of the 25th Annual Meeting of ISMRM, Honolulu, HI, USA, 2017. Abstract 2721. Digital Poster Presentation.

Awards

- ISMRM Merit Award (Magna Cum Laude): Three-Dimensional Simultaneous Whole-Brain T1, T2, and Apparent Diffusion Coefficient Mapping using MR Multitasking. 27th Annual ISMRM Scientific Meeting and Exhibition, Montreal, Canada, 2019. Abstract 5416.
- Meritorious Winner for Mathematical Contest in Modeling, 2014.
- Scholarship for Academically Excellent Undergraduates in Department of Electrical Engineering, Tsinghua University, 2013.
- Scholarship for Comprehensively Excellent Undergraduates in Department of Electrical Engineering, Tsinghua University, 2012.

Chapter I Introduction

1.1 Significance

For the past few decades, magnetic resonance imaging (MRI) has becoming a promising imaging technique in the clinical world to evaluate the structural and functional abnormalities of organs, tissues, and the skeletal system by producing three-dimensional, high resolution cross-sectional images. Compared to other popular imaging techniques such as computerized tomography, X-ray, or ultrasound, MRI has three major advantages: i) it is non-invasive; ii) it does not use ionizing radiation; and iii) it offers excellent soft tissue contrasts for the visualization of organ/tissue damages.

Currently, consensus MRI protocols for disease diagnosis almost solely rely on qualitative contrast-weighted imaging protocols with the assistance of contrast agent administration. Although the diagnostic utility of these conventional MRI protocols is indisputable, the limitations of qualitative MRI has been aware of to the clinical world, including the sensitivity to subtle physiological tissue changes, the biological specificity of different pathological substrates, and the multi-center reproducibility[1]. Furthermore, patients with renal insufficiency are unable to filter gadolinium-based contrast agents, facilitating the need for seeking non-contrast MRI protocols.

Quantitative MRI protocols that provide parameters with physical MR property and intrinsic to tissue information have long been a hot topic in MRI research. Unlike qualitative contrast-weighted images, quantitative parametric maps have potential to be more sensitive to alteration of tissue properties[2-4] and reproducible for multi-center studies[5,6]. Meanwhile, a lot of these parameters can be quantified without the need of contrast agent administration. If multiple parameters of interest are quantified and combined together, each of them will offer complementary tissue information, allowing comprehensive tissue characterization highly promising for risk stratification, early detection, staging, and treatment monitoring of diseases. What's more, with the development of advanced quantitative MRI techniques, multiple quantitative parameters can be acquired simultaneously, which significantly accelerates the MR exams, thus widely broadening the potential clinical application and pushing quantitative MRI towards routine clinical use.

1.2 Conventional Clinical MRI Practices

1.2.1 Pre-contrast MRI Protocols

MRI protocols implemented before contrast agent administration are referred to as pre-contrast MRI protocols. They include but are not limited to: T1-weighted (T1w) imaging, T2-weighted (T2w) imaging, fluid attenuated inversion recovery (FLAIR) imaging, diffusion-weighted imaging (DWI), and susceptibility-weighted imaging (SWI). Each of the protocol can reveal pathological abnormalities through relative signal intensity differences of different tissues, and several image protocols can be combined for diagnosis depending on the clinical recommendations for different disease types.

1.2.2 Post-contrast MRI Protocols

MRI protocols implemented after contrast agent administration are referred to as post-contrast MRI protocols. Nowadays, nearly half of the MRI studies are contrast-enhanced studies[7]. The most popular MRI contrast agent is paramagnetic gadolinium ion complexes which significantly shorten the T1 and/or T2 relaxation time of neighboring water protons, creating hyperintense T1w signals and /or hypointense T2w signals on abnormal or damaged tissues with high vascular density and thin vessel wall such as a majority of tumors[8,9]. Contrast-enhanced tumors usually appear significantly brighter on post-contrast T1w compared to pre-contrast T1w, allowing easy identification and diagnosis. Common post-contrast MRI protocols include but are not limited to T1w imaging, T2w imaging, and dynamic contrast enhanced (DCE) imaging. However, despite the ability of these conventional MRI protocols to reveal pathological tissue abnormalities, their sensitivity, specificity, reproducibility, and predictive values are rather limited[10,11].

1.3 Potential Risks of Contrast Agents

Despite proven greatly useful in clinical practices, the debate over the safety of gadolinium-based MRI contrast agents never ceases. The association between the exposure of gadolinium-based contrast agents during MRI and the development of nephrogenic system fibrosis (NSF) in renal insufficiency patients was first established in 2006[12]. The gadolinium deposition in body tissues has been a big concern in radiology. It has been reported that in vivo clinical exposure to gadolinium chelates may result in gadolinium deposition not only in kidney, but also in bone matrix and neuronal tissues for an extended period, even in patients with normal renal functions[13-16]. In addition, chronic toxic effects of possibly retained gadolinium were reported, including numbness, tingling, muscle twitching, skin conditions, and cognitive impairments[17]. Although the clinical evidence linking these post-MRI symptoms to gadolinium retention is limited, the administration of gadolinium-based contrast agents should proceed with caution, and sometimes it would raise patients' concern and unwillingness for contrast agent injection.

1.4 Non-contrast Quantitative Multiparametric MRI in Clinical Practices

Recent technological advances in both hardware and software has allowed the use of quantitative MRI in clinical research or even routine diagnosis. Most of the quantitative MRI approaches do not require the injection of contrast agents, making the MRI exams safer and reducing costs. As part of routine clinical practices, T1 and T2 mapping have been widely adopted in clinical cardiac MRI scans to image patients with various cardiovascular diseases such as cardiomyopathies, ischemic heart diseases, and more, for the evaluation of disease progression and treatment monitoring[18-20]. Apparent diffusion coefficient (ADC) mapping, which is available through DWI, has also been routinely implemented in clinical practices for early detection, diagnosis, and prognosis of almost all types of cancer including brain, breast, pancreas, prostate, and more[21-25].

A combination of multiple quantitative parameters can allow comprehensive assessment of tissue states. Table 1 shows some common diseases and their clinically associated quantitative tissue biomarkers.

Table 1. Common diseases and their clinically associated quantitative tissue parameters

	Diseases	T1	T2	T2*	T1ρ	ADC	SWI/ QSM	FF
Neuro	Stroke	+	+			+	+	
	Traumatic brain injury	+	+			+	+	
	Epilepticus	+	+			+	+	
	Multiple sclerosis	+	+	+	+	+	+	
	Glioblastoma	+	+	+		+	+	
	Parkinson's disease	+	+	+	+	+	+	
	Alzheimer's disease	+	+	+	+	+	+	
Cardiovascular	Iron overload cardiomyopathy	+	+	+				
	Myocarditis	+	+					
	Sarcoidosis		+					
	Intramyocardial hemorrhage		+	+			+	
	Myocardial infarction	+	+		+	+		
	Dilated cardiomyopathy	+	+					
	Hypertrophic cardiomyopathy	+	+			+		
	Amyloidosis	+						
	Systemic lupus erythematosus	+				+		
	Diabetic cardiomyopathy							+
	Cardiotoxicity	+						
Body	Liver iron overload	+	+	+			+	
	Cancer							
	Breast	+	+	+		+		
	Prostate	+	+			+	+	
	Liver	+	+	+		+	+	
	Liver fibrosis	+	+		+	+	+	+
	Hepatic carcinoma	+	+	+		+	+	
	Hepatic/pancreatic steatosis							+
Cartilage	Osteoarthritis	+	+	+	+	+	+	

In recent years' clinical research and studies, quantitative multiparametric MRI has becoming a growing trend for risk assessment, improving diagnostic accuracy, and prediction of treatment response. It has significant potential to improve image guided patient care through better diagnostic decision making. For example, T1 and T2 mapping documented much earlier signs (8 weeks before progression) of brain tumor progression before any obvious changes in conventional qualitative images[26,27]. T1, T2, and ADC mapping demonstrated the ability of differentiation and categorization of various brain tumor types[25,28]. In the pancreas, the combination of T1, T2, and ADC mapping yielded the best sensitivity, specificity, and diagnostic accuracy of pancreatic cancer compared to any single measurement[29]. In the prostate, the combination of T1, T2, and ADC produced the best differentiation between normal appearing and cancerous peripheral zone[30]. T1, T2*, and proton density fat fraction (PDFF) demonstrated good diagnostic performance of hepatic steatosis, hepatic inflammation and liver fibrosis across a range of disease severity and etiology[31-33]. Combining T1, T2, T2*, and magnetization transfer rate (MTR) increased the pathological specificity to white matter (WM) damage at early stage of multiple sclerosis (MS) and showed predictive power of patient motor and cognitive function at longitudinal follow-up[34]. T2, and T1ρ mapping allowed the detection and assessment of the degenerative pathological progression including inflammation, demyelination, and axonal damage in MS[35].

1.5 Technical Challenges of Quantitative Multiparametric MRI

Despite all the potential benefits of quantitative multiparametric MRI in clinical practices, a lot of quantitative parameters are not widely acquired in a clinical setting because of some major technical limitations.

First, quantitative MRI requires prolonged acquisition time because usually multiple set of images with specific timings or sequence parameters need to be collected to quantify one single tissue parameter. And because these image sets usually cannot be shared between different parameters, quantification of multiple tissue parameters will substantially increase the scan time and reduces the scan efficiency, which is not acceptable in most clinical MR exams due to patient care and cost issues. As a result, image resolution or spatial coverage will usually be traded for scan time reduction.

The second technical challenge is patient motion. Unexpected bulk motion typically requires reacquisition which further compromises scan efficiency and increases costs. Physiological motion can be eliminated or compensated with breath holds or synchronized acquisition with motion rhythms using electrocardiogram (ECG) or gating methods, but those may not work well on patients with specific diseases. Failure to compensate motion will cause image artifacts, leading to inaccurate quantification and loss of valuable diagnostic information.

Finally, multiparametric MRI is usually performed in separate scans, which leads to misaligned parametric maps due to inter-scan misplacement, complicating clinical image interpretation and the joint analysis of multiple parameters. Meanwhile, separate quantitative scans also complicate the workflow for technicians due to the manual settings of acquisition volumes, shimming, etc. As a result, a novel strategy that enables simultaneous quantitative multiparametric acquisitions with high imaging efficiency would be vastly desirable in clinical practices.

1.6 Specific Aims

The long-term objective of this dissertation will focus on whole-body tissue characterization with a novel contrast agent-free, simultaneous quantitative multiparametric MRI technique named as “Magnetic Resonance Multitasking”. As a starting point of the long-term goal, we present in this dissertation technical developments for i) simultaneous T1, T2, and ADC quantification, and ii) simultaneous T1, T2, and/or T1ρ quantification with potential application in the brain, breast, and heart, in an accelerated, push-button MR exam that simplifies acquisition workflow. Different motion handling strategies including motion-removed imaging and motion-resolved imaging will be introduced as part of the technical developments.

Chapter 2 provides basic contexts and background information of qualitative and quantitative MRI, basic MR physics of some common tissue parameters, and general introduction of MR Multitasking. Chapters 3-4 introduces the simultaneous T1, T2, and ADC quantification technique and the simultaneous T1, T2, and T1ρ quantification technique, respectively, with application in the brain. Chapter 5 introduces the extension of the developed techniques to the breast and heart as other potential applications. The two specific aims are as follows:

1.6.1 Aim 1: To develop an approach for 3D simultaneous T1, T2, and ADC quantification with in a clinically feasible scan time using MR Multitasking

Chapter 3 presents a novel technique for simultaneous T1, T2, and ADC quantification in the brain with 3D coverage in 9.3min. High quality, co-registered brain T1, T2, and ADC maps are generated. MR Multitasking conceptualizes different image contrasts to be quantified as different time dimensions. Substantial acceleration can be achieved by exploiting the strong spatiotemporal signal correlation along and across different dimensions using a low-rank tensor (LRT) image model. A time-resolved phase correction is incorporated to compensate for the inter-shot phase inconsistencies induced by physiological motion. A motion-removal strategy is employed to discard the data corrupted by bulk motion, producing clean quantitative maps without blurring and ghosting artifacts.

1.6.2 Aim 2: To develop a rigid motion-resolved, 3D simultaneous T1, T2, and T1ρ mapping technique using MR Multitasking with initial clinical study on a relapsing remitting multiple sclerosis patient cohort

Chapter 4 describes another application of MR Multitasking which produces simultaneously acquired, co-registered T1, T2, and T1ρ maps with 3D whole-brain coverage in 9min. We present a novel idea for handling rigid motion in brain MRI, where different motion states are simultaneously captured and resolved in an extra time dimension in the framework. Motion-resolved multiparametric maps are efficiently generated by jointly exploring the signal correlation along different parameter and motion dimensions. Thorough motion experiments are designed to investigate different types of rigid motion. Clinical validation is performed on a relapsing remitting multiple sclerosis patient cohort where the combination of T1, T2, and T1ρ demonstrates superior performance of tissue characterization in multiple sclerosis compared to using either single parameter alone.

Chapter II Backgrounds

2.1 Qualitative MRI

In current clinical systems, clinical MRI is mostly dominated by qualitative exams which measures different signal intensities with arbitrary units. On the collected MRI images, these signal intensities are represented as bright or dark contrasts which are a combination of multiple factors – parameters intrinsic to tissue properties and/or external experimental conditions. The relative signal contrasts between tissues can be sensitive to scanners, coils, image protocols, and times of the scan, posing challenges on multi-center studies and longitudinal evaluation of disease progression. Clinical diagnosis is made with visual examination of the regional differences in signal intensities between areas with gross morphological or focal abnormalities and areas that are "supposedly" normal, which relies on subjective determination as it lacks physiological evidence to confirm healthy tissues. Qualitative MRI may be insensitive to mild disease states or subtle tissue changes that affect an organ globally. It also inevitably lacks biological specificity, as different pathological conditions can produce similar signal intensities on the images. Clinical qualitative images of an MS patient are shown in Figure 1A where only relative signal intensities are available.

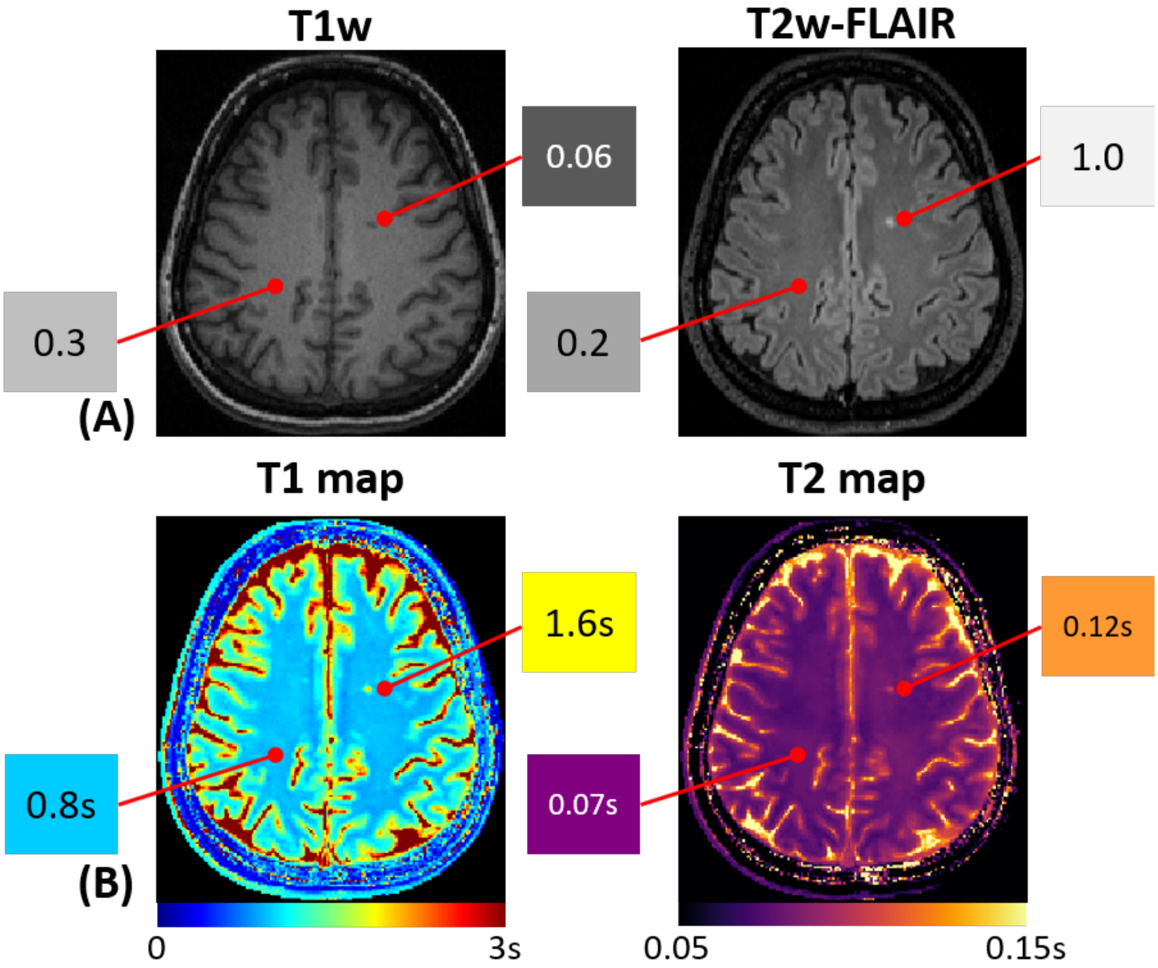

Figure 1. (A) Example clinical qualitative T1w and T2w-FLAIR images with unitless pixel values. (B) Corresponding quantitative T1 and T2 maps whose pixel values are with meaningful physical variables.

2.2 Quantitative MRI

The concept of quantitative MRI was first established in 1980's when the nuclear magnetic resonance (NMR) properties (proton density (PD), T1, T2, etc.) of tissues were quantified to differentiate biological tissues according to the exact values of these parameters. Nowadays, an MRI study is considered quantitative if parametric maps are obtained with meaningful physical or chemical variable that can be measured with interpretable physical units and can be compared between tissues and among subjects[1]. Quantitative measurement of tissue parameters has four major advantages over qualitative interpretation such that: i) quantitative measurements are highly reproducible[5,6], which allows direct comparisons of tissue properties across different sites, subjects, and times; ii) quantitative measurements can establish a normative range for healthy tissue states from a healthy control group, which provides the foundations for disease assessments[29,34,36]; iii) quantitative measurements are more sensitive to subtle physiological changes in tissue states and more specific for tissue characterization and disease diagnosis[2-4,37,38]; and (iv) quantitative MRI tissue parameters can act as candidate imaging biomarkers that are directly associated with disease states. Figure 1B demonstrates quantitative MRI with T1 and T2 maps of the same patient, where specific T1 and T2 values are available for each voxel within different tissues.

2.3 MR Physics of Tissue Parameters and Quantitative Methods

This section will review the concepts and physics of several commonly used tissue parameters and the typical methods to quantify these parameters. Among these parameters, T1, T2, T1ρ, and ADC will be the main focus in this dissertation. Other parameters can also be quantified with the proposed method described in this dissertation, as has been demonstrated in a few preliminary works from our group (which will be introduced in Chapter 7).

2.3.1 T1 relaxation time

T1 relaxation time, which is also known as spin-lattice relaxation time or longitudinal relaxation time, describes the recovery rate of the longitudinal magnetization (M_z) toward the thermal equilibrium (M_0) parallel to the main magnetic field (B0)[39]. The value of T1 is associated with the transfer rate of the energy flow between the spin system and the external environment such as nearby atoms, nuclei, and molecules. T1 is mathematically characterized as the time required for M_z to reach (1-1/*e*) or ~63% of M_0. Figure 2 describes the T1 relaxation process.

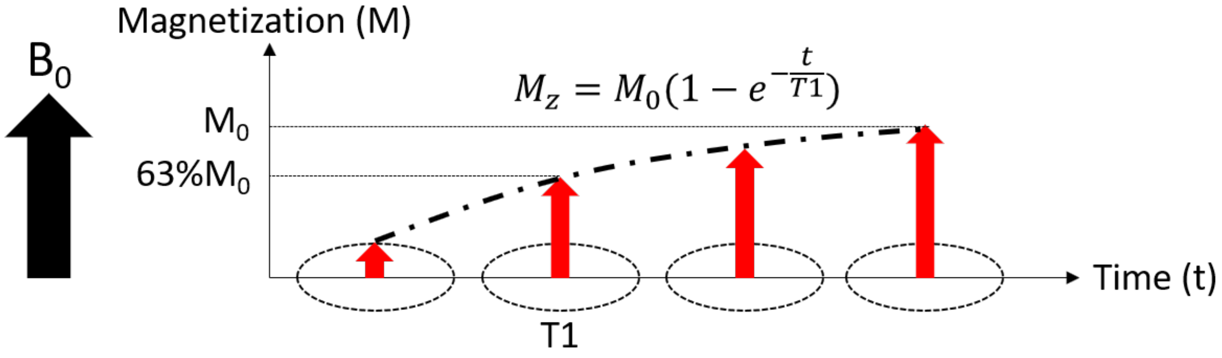

Figure 2. Demonstration of the T1 relaxation process.

T1 relaxation time is usually quantified with a saturation recovery (SR) or inversion recovery (IR) sequence[40-42]. By sampling the MR signals at several saturation times (TS) or inversion times (TI), T1 can be obtained through a three-parameter nonlinear fitting of a recovery model (we use IR as an example here):

$$M_z(n) = A \cdot (1 - (1 - B)e^{-\frac{TI(n)}{T1}}), \tag{2.1}$$

where $M_z(n)$ is the signal at the nth inversion time $TI(n)$, A absorbs proton density and coil receive sensitivity, and B denotes the inversion efficiency factor. Figure 3 illustrates the T1 fitting process with an IR example.

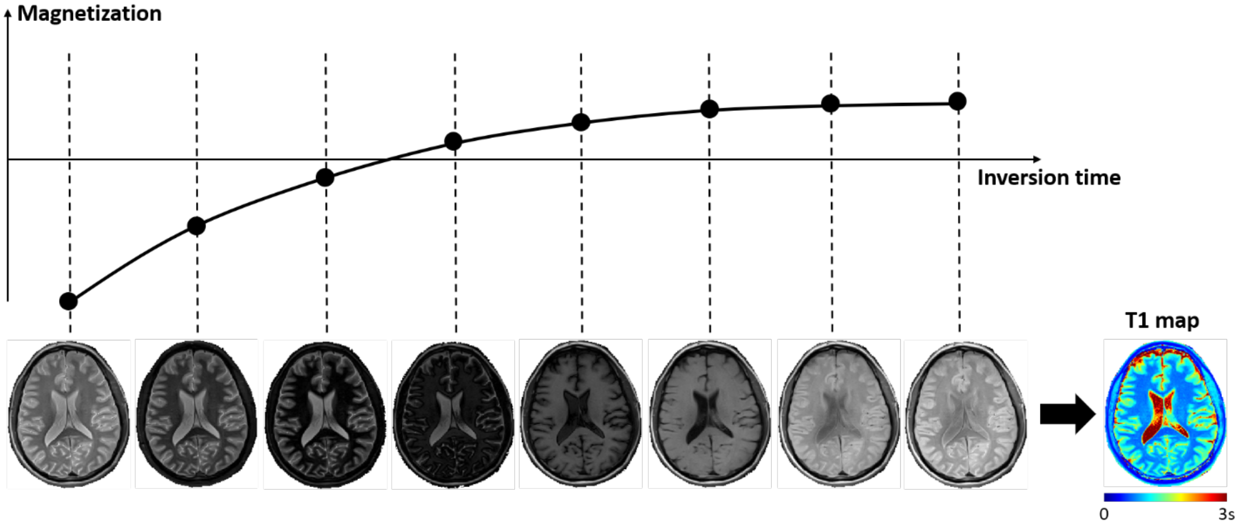

Figure 3. Demonstration of a typical T1 fitting process using IR, where multiple inversion recovery images are required for a voxel-wise T1 exponential fitting.

2.3.2 T2 relaxation time

T2 relaxation time, which is also known as spin-spin relaxation time or transverse relaxation time, describes the dephasing rate of the transverse magnetization (M_{xy}) toward zero after an excitation RF field (B1)[39]. The value of T2 is associated with the loss of phase coherence in the spin system. T2 is mathematically characterized as the time required for M_{xy} to fall to 1/*e* or ~37% of its initial value immediately after the RF excitation. Figure 4 describes the T2 relaxation process.

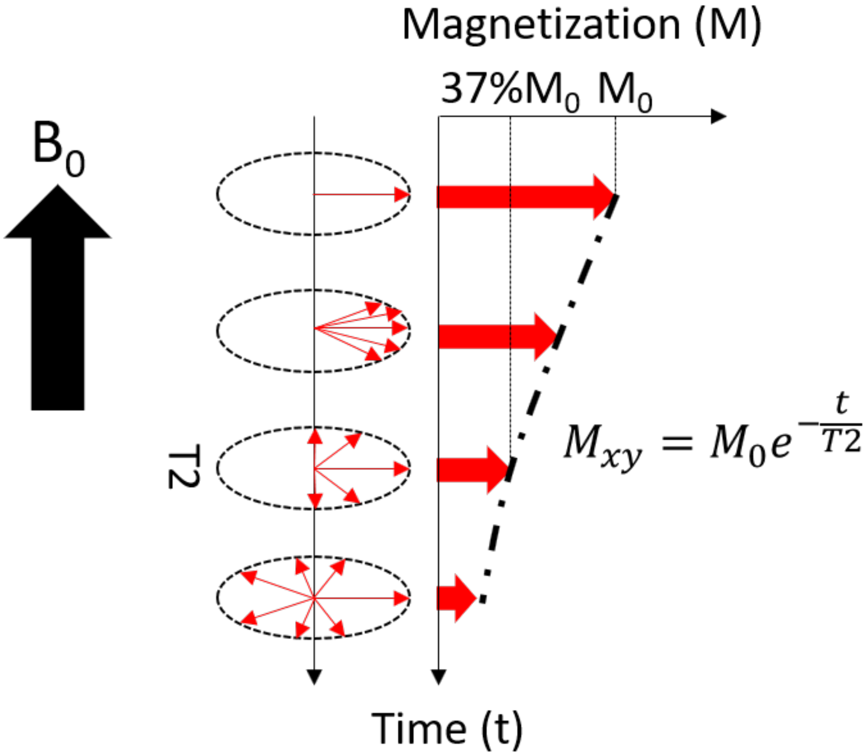

Figure 4. Demonstration of the T2 relaxation process.

T2 relaxation time is usually quantified with a spin echo (SE)-based or T2-preparation (T2-prep)-based sequence[43,44]. By sampling the MR signals at several echo times (TE) or using several T2-prep with different preparation durations, T2 can be obtained through a two-parameter nonlinear fitting of a decay model:

$$M_{xy}(n) = A \cdot e^{-\frac{TE(n)}{T2}}, \tag{2.2}$$

where $M_{xy}(n)$ is the signal at the nth echo time $TE(n)$, and A absorbs proton density and coil receive sensitivity. Figure 5 illustrates the T2 fitting process with a turbo spin echo (TSE) example.

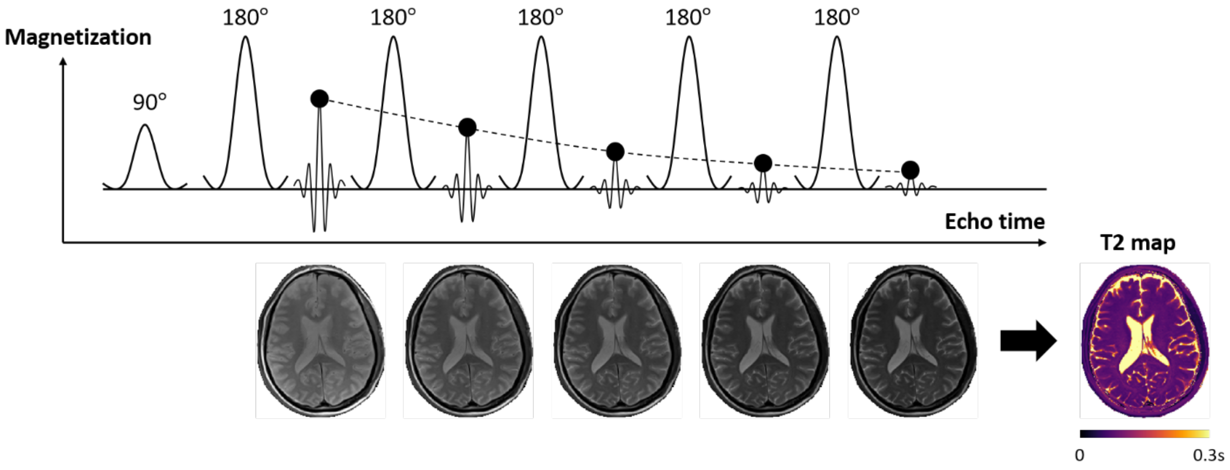

Figure 5. Demonstration of a typical T2 fitting process using TSE, where multiple T2W images corresponding to different TE are required for a voxel-wise T2 exponential fitting.

2.3.3 T2* relaxation time

T2* relaxation comes from the additive effect of spin-spin relaxation and local field inhomogeneities which includes the B0 inhomogeneity, the differences in magnetic susceptibility among various tissues, chemical shift, and spatial encoding gradients[45]. The presence of local field inhomogeneities causes additional dephasing in the spin system, resulting in a faster decay rate of M_{xy} characterized by T2* relaxation time. The relationship between T2* and T2 is represented as:

$$\frac{1}{T2^*} = \frac{1}{T2} + \gamma\Delta B, \tag{2.3}$$

where ΔB is the magnetic field inhomogeneity across a voxel. Figure 6 describes the T2* relaxation process.

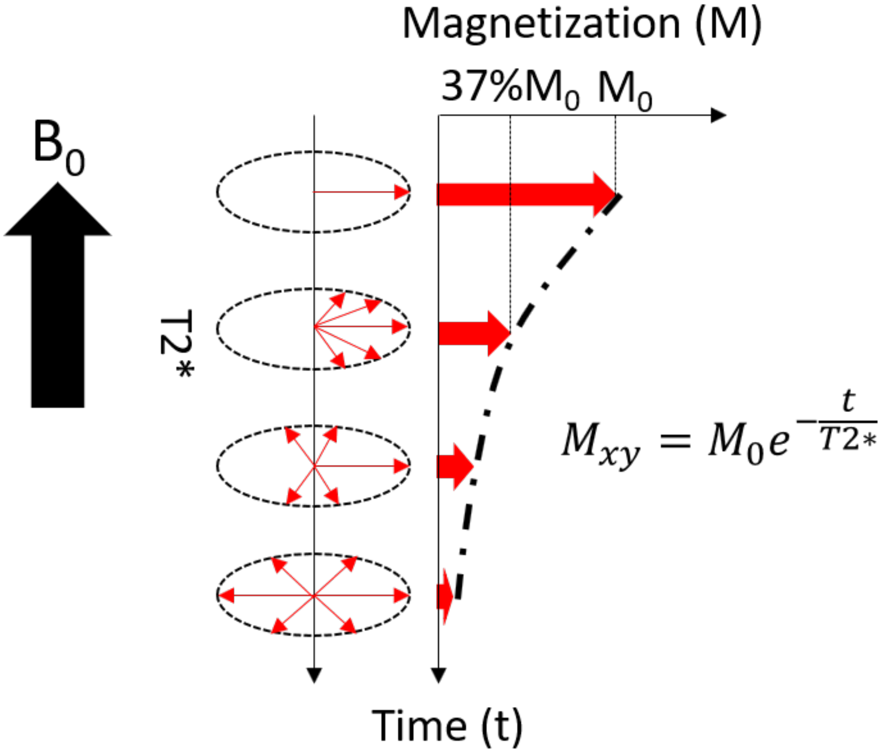

Figure 6. Demonstration of the T2* relaxation process. Note that T2* decay is faster compared to T2 decay as demonstrated in Figure 4, because of the extra dephasing induced by field inhomogeneities.

T2* relaxation time can be quantified with a gradient echo (GRE)-based sequence[19,45]. A multi-echo structure with gradient rephasing is usually implemented to sample signals at several TEs. T2* can be fitted similarly as T2 with the same decay model (i.e., Eq. (2.2)). Figure 7 illustrates the T2* fitting process with a simple GRE example.

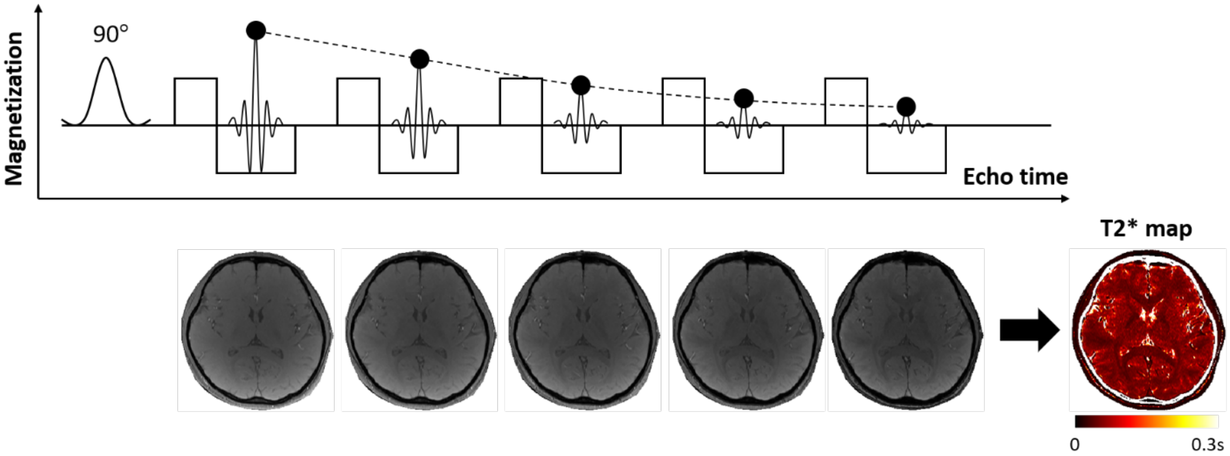

Figure 7. Demonstration of a typical T2* fitting process using multi-echo GRE, where multiple T2*-weighted images corresponding to different TE are required for a voxel-wise T2* exponential fitting. T2*-weighted images and T2* map courtesy to Tianle Cao.

2.3.4 Quantitative Susceptibility Mapping (QSM)

QSM is a novel technique that aims to map the spatial susceptibility distribution of tissues from the MRI phase and local field data, which quantifies the magnetic susceptibility and produces a unique susceptibility-weighted contrast to describe the change of magnetization within tissues in response to magnetic field inhomogeneities[46]. QSM has great promise for evaluating chemical and molecular composition of tissues such as water, myelin, iron, and calcium, and has been proven useful in traumatic injury assessment[47], differentiation between blood deposits and calcifications[48], and disease characterization of neurodegenerative pathologies[49,50].

Magnetic susceptibility can be quantified with a ME-GRE sequence which simultaneously allows the calculation of T2*. As a result, T2* imaging and QSM are usually performed in combination. Conversion from GRE images to QSM requires complicated processing, including sensitivity reconstruction, field map estimation, background field removal, and solving a field-to-susceptibility inverse problem[46]. Detailed QSM computation is beyond the scope of this section.

2.3.5 T1ρ relaxation time

T1ρ relaxation is also referred to as spin-lattice relaxation in the rotating frame[51]. T1ρ relaxation time describes the dephasing rate of M_{xy} in the presence of an external spin-lock RF pulse (B_{SL}) after B1 excitation. B_{SL} forces the spins to process around its direction in the rotating frame at the frequency of the spin-lock pulse denoted as spin-lock frequency (FSL). FSL is usually at the range of kilohertz which is far lower than the Larmor frequency at the range of megahertz, making T1ρ suitable to detect low frequency biochemical motional processes such as protein exchange between macromolecules and extracellular water. Note that the only difference between T2 and T1ρ relaxation is the existence of B_{SL}. As a result, T2 is a special case of T1ρ when B_{SL}=0.

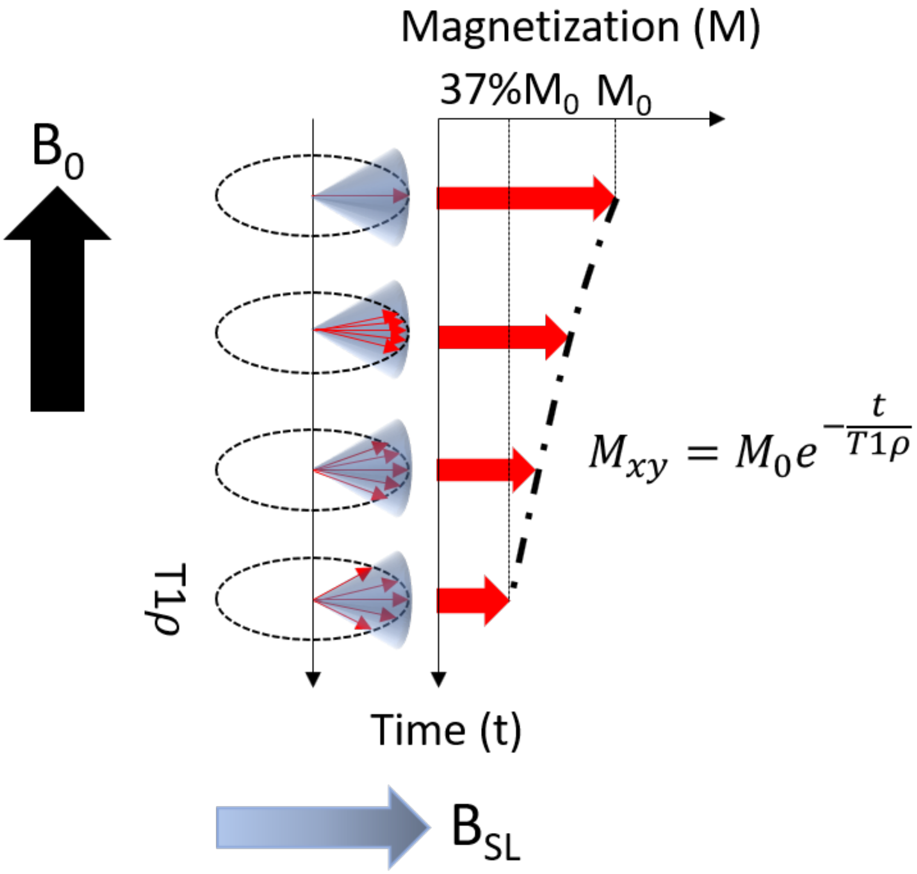

Figure 8. Demonstration of the T1ρ relaxation process. Note that T1ρ decay is usually slower compared to T2 decay as demonstrated in Figure 4, because of the spin-lock pulse along which the spins are forced to process.

Figure 8 describes the T1ρ relaxation process.

T1ρ relaxation time can be quantified with a T1ρ-preparation (T1ρ-prep)-based sequence[51]. Similar to T2 quantification with T2-prep, different T1ρ weightings can be generated using several T1ρ-prep with different preparation durations which is also known as spin-lock times (TSL). T1ρ can be obtained through a two-parameter nonlinear fitting of a similar decay model as in T2:

$$M_{xy}(n) = A \cdot e^{-\frac{TSL(n)}{T1\rho}}, \tag{2.4}$$

where $M_{xy}(n)$ is the signal sampled after the nth spin-lock time $TSL(n)$, and A absorbs proton density and coil receive sensitivity. Figure 9 illustrates the T1ρ fitting process with a single spin-lock pulse T1ρ-prep example.

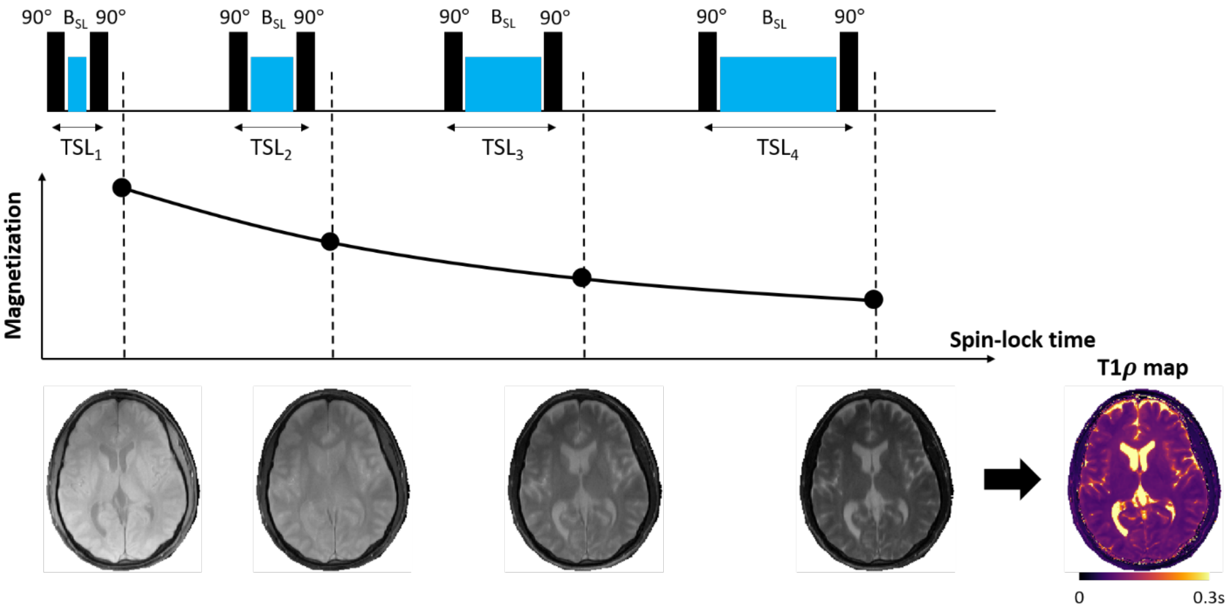

Figure 9. Demonstration of a typical T1ρ fitting process using a T1ρ-prep-based sequence, where multiple T1ρ-weighted images corresponding to different TSL are required for a voxel-wise T1ρ exponential fitting.

2.3.6 ADC

Diffusion MRI allows the measurement of molecular diffusion of water molecules in tissues, providing a unique solution to probe the microscopic tissue architecture in a non-contrast, non-invasive manner[52]. By applying a pair of diffusion-sensitizing gradients along one or more gradient axes which specifies a diffusion direction, the diffusion contrast can be generated with unique sensitivity to this direction:

$$S = S_0 e^{-bD}, \tag{2.5}$$

where S represents the diffusion-weighted signal, S_0 represents the non-diffusion signal acquired without diffusion gradients, b is the "b-value" that describes how much "diffusion weighting" was imparted, and D is the diffusion coefficient measuring the diffusing ability along this specific diffusion direction.

ADC measures the overall diffusing ability within the voxel. The common practice for quantifying ADC requires the acquisition of diffusion-weighted images along three orthogonal diffusion directions (without loss of generality, we assume x, y, z axes) using a diffusion-weighted single-shot echo planar imaging (DW-SSEPI) sequence[53], a diffusion-weighted readout-segmented echo planar imaging (DW-RSEPI) sequence[54], or a diffusion-preparation (D-prep)-based sequence[55,56]. ADC is then calculated as the average of the diffusion coefficients along those three orthogonal directions, and can be obtained with the geometric average of the three images:

$$S_{xyz} = \sqrt[3]{S_x S_y S_z} = S_0 e^{-b \cdot \frac{D_x + D_y + D_z}{3}} = S_0 e^{-b \cdot ADC}, \tag{2.6}$$

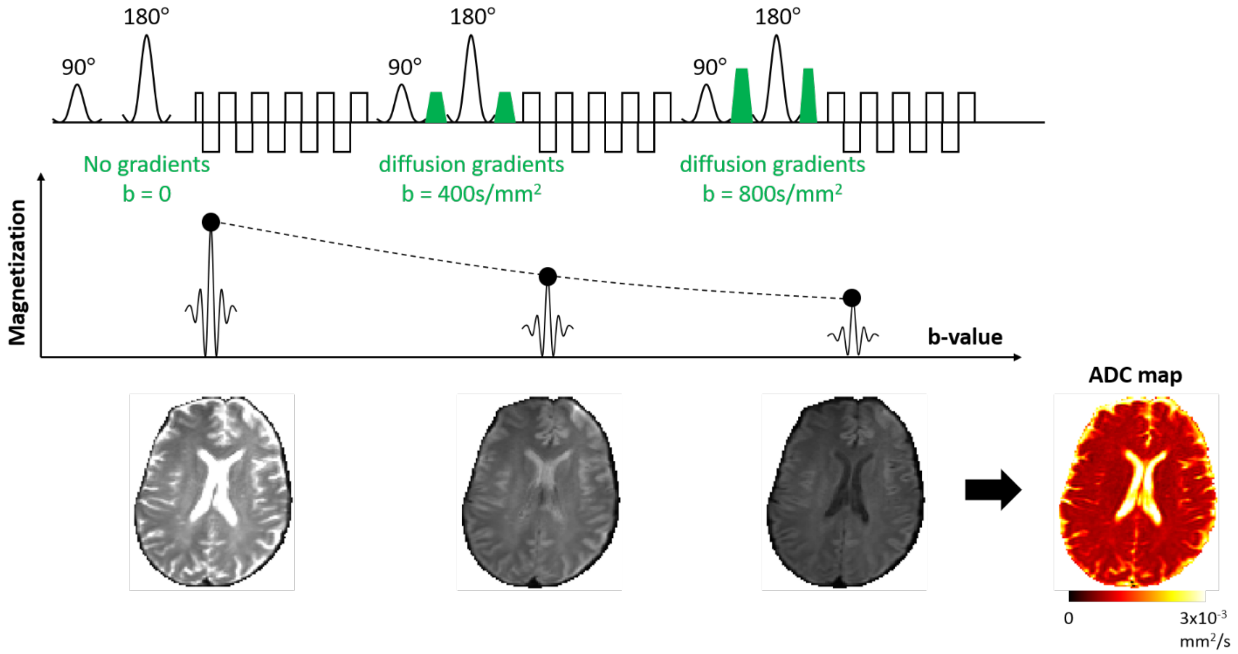

Figure 10. Demonstration of a typical ADC fitting process using a DW-SSEPI sequence with three diffusion-weightings — b=0 indicating no diffusion-weighting, b=400s/mm^2, and b=800s/mm^2.

where S_x, S_y, S_z are diffusion-weighted images sensitized to x, y, and z directions respectively, and D_x, D_y, and D_z are diffusion coefficients along x, y, and z directions respectively. Figure 10 illustrates the ADC fitting process with a DW-SSEPI example.

2.3.7 Proton Density Fat Fraction (PDFF)

PDFF is defined as the density of hydrogen protons attributable to fat, and is a meaningful tissue biomarker that is capable of revealing excessive intracellular fat accumulation in hepatocytes[33]. Therefore, PDFF has significant potential for the assessment of hepatic steatosis in nonalcoholic fatty liver disease patients for clinical care. PDFF is known for its high accuracy in the detection of hepatic steatosis, and is highly reproducible across readers, MR manufacturers, and field strengths[57].

To calculate PDFF, it is important to acquire both water signal W and fat signal F, so that:

$$PDFF = \frac{F}{W+F}. \quad (2.7)$$

In practice, this can be achieved by sampling signals at different TEs where the water and fat are in-phase and out-of-phase. Therefore, we can rewrite Eq. (2.7) as:

$$PDFF = \frac{IP-OP}{2IP}, \quad (2.8)$$

where $IP = W + F$ denotes in-phase signal, and $OP = W - F$ denotes out-of-phase signal[33]. PDFF is usually quantified with ME-GRE-based sequences with low flip angle to reduce the effect of T1 bias[33]. Figure 11 demonstrates typical water image, fat image, and PDFF map.

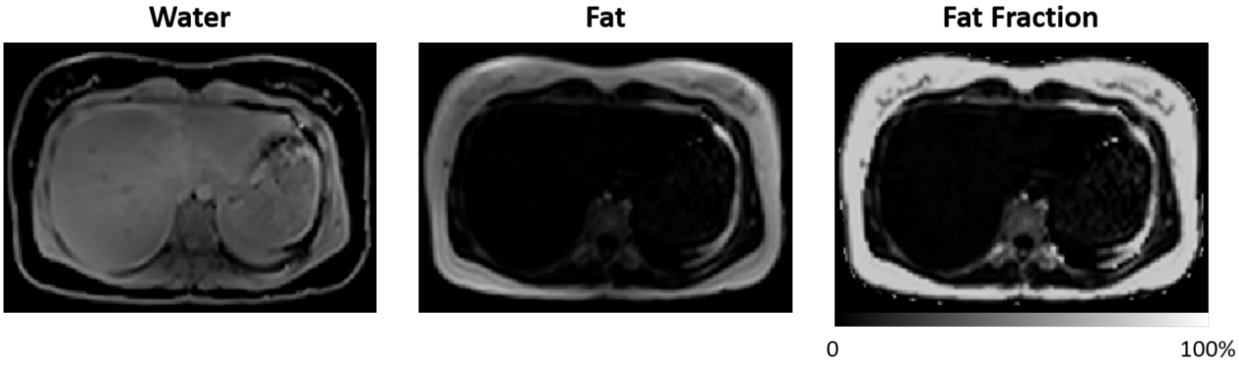

Figure 11. Example water image, fat image, and fat fraction map. Images courtesy to Nan Wang.

2.4 Simultaneous Quantitative Multiparametric MRI Overview

Over recent years, various novel techniques have been proposed to simultaneously quantify multiple tissue biomarkers for the purpose of comprehensive tissue characterization without the injection of contrast agents. These techniques simplify clinical workflows and provide co-registered multiparametric maps that are convenient for joint analysis.

Several parameter-specific quantitative methods are invented for a few target biomarkers. Deoni et al. proposed a hybrid T1/T2 quantification method named DESPOT1/DESPOT2, which consisted of a spoiled gradient echo sequence for T1 quantification followed by a subsequent steady state free precession (SSFP) sequence for T2 quantification, with prior knowledge of T1[58]. Metere et al. proposed a multi-echo magnetization-prepared 2 rapid gradient echoes sequence for joint T1, T2* and QSM quantification, where T1 was obtained with the overall IR structure and T2* and QSM were obtained with multiple gradient echoes embedded in each readout block[6]. Li et al. concatenated multiple T1ρ-prep and T2-prep in a single sequence structure for joint estimation of T2 and T1ρ[59]. Zhang et al. proposed a stimulated echo-based mapping approach for simultaneous T1, T2, and ADC mapping where various combinations of mixing time (TM), TE, and b-values were collected to densely sample the sequence parameter TM-TE-b space[60]. Marty et al. employed a bi-component extended phase graph fitting for joint T2 and FF quantification with a multi-slice multi-echo approach[61].

In 2013, a new imaging paradigm named magnetic resonance fingerprinting (MRF) was proposed for the purpose of simultaneous quantification of multiple parameters[62]. The key idea is that analogous to the biological traits of human where each person possesses a unique set of fingerprints, MR signals generated from tissues with varying tissue properties (i.e., T1, T2, etc.) also have unique signal evolutions (i.e., “fingerprints”), as long as multiple sequence parameters (i.e., TI, TR, TE, etc.) are simultaneously varying throughout the entire scan. A dictionary of anticipated signal courses is generated in advance following a signal model using the same sequence parameters as in the scan, as well as a range of feasible tissue properties. Pattern recognition is performed to compare the measured signal course with the simulated ones in the dictionary. For each voxel, the set of tissue properties corresponding to the signal course in the dictionary that resembles closest to the measured signal course is assigned to this voxel. It has been shown that the pattern recognition process is robust to undersampling artifacts, allowing significantly accelerated MRF scans with high signal-to-noise ratio (SNR) efficiency. Moreover, no additional constraints on sequence structures are posed to the MRF framework besides the pseudo-randomized sequence parameters, which enables flexible experiment design to target different combinations of tissue properties depending on specific clinical applications. Quantification of various tissue properties are demonstrated feasible with numerous attempts in the brain[28,62], breast[36], heart[63,64], abdomen[65], and prostate[30]. However, MRF is not inherently robust to motion. It has been shown that motion happening towards the end of the scan has less impact on the quantification[62]. Although multiple attempts have been made for different motion correction approaches, most of them are based on 2D imaging and show limitation in dealing with through-plane motion[66-68]. So far, most cardiac MRF studies are performed with ECG triggering to target specific cardiac phases[63,64].

2.5 Magnetic Resonance Multitasking

In 2018, our group developed a novel technique for simultaneous quantitative multiparametric MRI–MR Multitasking–which allows us to simultaneously resolve multiple overlapping image dynamics including varying contrasts induced by different tissue properties and different types of motion[69]. MR Multitasking establishes a multidimensional imaging framework where each image dynamic, which is also referred to as “task”, is assigned to a time dimension, and multiple time dimensions can be simultaneously and efficiently resolved using a low-rank tensor (LRT) image model which explores the spatiotemporal multidimensional signal correlation. MR Multitasking has high scanning efficiency, as the LRT image model significantly reduces the degrees of freedom of the underlying multidimensional image, thus also reducing the sampling requirements. It allows flexible implementation of different sequences so long as they fulfill certain sampling strategies to leverage low-rankness and compressed sensing. It simplifies clinical workflows by integrating multiple capabilities into a single scan, providing co-registered multiparametric maps to benefit comprehensive tissue characterization. Most importantly, MR Multitasking has inherent advantages over MRF to deal with motion, as it "embraces" motion, rather than avoiding them, by capturing different types of motion in one or more time dimensions, allowing motion-resolved imaging in a continuous acquisition without the use of external devices/algorithms for gating and/or triggering[69,70]. Other motion handling strategies such as motion compensation and motion rejection are also easily compatible with MR Multitasking[71-73].

2.5.1 Low-Rank Tensor Image Model

MR Multitasking conceptualizes overlapping image dynamics to be quantified in a multidimensional image function $x(\mathbf{r}, t_1, t_2, \dots, t_N)$ with $\mathbf{r}$ indexing the spatial dimension and $t_1, t_2, \dots, t_N$ indexing N time dimensions. Example time dimensions include but are not limited to cardiac motion, respiratory motion, rigid head motion, temporal evolution within one recovery period characterizing T1 relaxation, magnetization preparation index characterizing T2 relaxation, T1ρ relaxation, or diffusion process, and multi-echo index within one TR characterizing T2* relaxation. x is partially separable in space and time due to strong multidimensional spatiotemporal correlation[69,74], resulting in:

$$x(\mathbf{r}, t_1, t_2, \dots, t_N) = \sum_{j=1}^{J} u_j(\mathbf{r}) \varphi_j(t_1, t_2, \dots, t_N), \tag{2.9}$$

$$\varphi_j(t_1, t_2, \dots, t_N) = \sum_{j=1}^{J} \sum_{l_1=1}^{L_1} \dots \sum_{l_N=1}^{L_N} c_{j l_1 \dots l_N} v_{1,l_1}(t_1) \dots v_{N,l_N}(t_N), \tag{2.10}$$

where $\{u_j(\mathbf{r})_{j=1}^{J}$ are spatial basis functions spanning the spatial subspace, $\{v_{i,l_i}(t_i)\}_{l_i=1}^{L_i}$ are temporal basis functions spanning the N individual temporal subspaces, $c_{j l_1 \dots l_N}$ are the elements of a small core tensor $\mathcal{C} \in \mathbb{C}^{J \times L_1 \times \dots \times L_N}$ that governs the interaction between different dimensions, and $\{\varphi_j(t_1, t_2, \dots, t_N)\}_{j=1}^{J}$ are multidimensional temporal basis functions spanning the multidimensional temporal subspace modeling all the temporal dynamic processes.

Furthermore, x can be rearranged into an (N+1)-way tensor $\mathcal{X}$ with elements $X_{jl_1 \dots l_N} = x(r_j, t_{1,l_1}, \dots, t_{N,l_N})$. $\mathcal{X}$ is therefore an LRT due to the spatiotemporal correlation in x.[75] The LRT structure of $\mathcal{X}$ can be expressed via the Tucker form[76] of tensor decomposition:

$$\mathcal{X} = \mathcal{C} \times_1 \mathbf{U} \times_2 \mathbf{V}_1 \times_3 \mathbf{V}_2 \times_4 \dots \times_{N+1} \mathbf{V}_N, \tag{2.11}$$

where the $\times_i$ operator denotes the ith mode product[77], $\mathbf{U}$ is the spatial factor matrix containing spatial basis functions $\{u_j(\mathbf{r})\}_{j=1}^{J}$, and $\mathbf{V}_i$ are the temporal factor matrices of the ith time dimension containing temporal basis functions $\{v_{i,l_i}(t_i)\}_{l_i=1}^{L_i}$. In practice, the tensor decomposition form in Eq. (2.11) can be explicitly expressed in the corresponding matrix factorization form following Eqs. (2.9) and (2.10):

$$\mathbf{X}_{(1)} = \mathbf{U}\mathbf{\Phi}, \tag{2.12}$$

$$\mathbf{\Phi} = \mathbf{C}_{(1)}(\mathbf{V}_N \otimes \dots \otimes \mathbf{V}_1)^T, \tag{2.13}$$

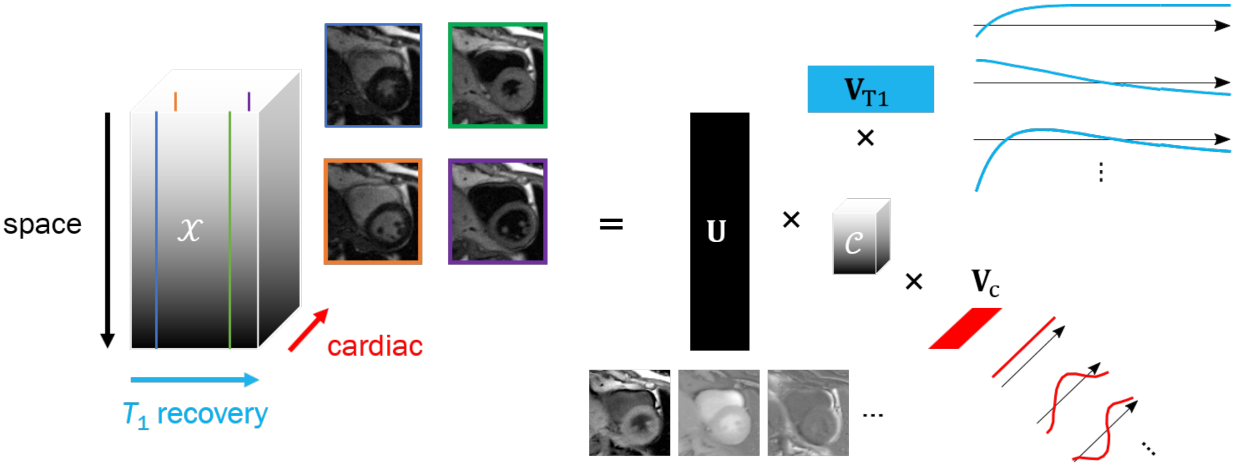

Figure 12. Illustration of multiple time dimensions and the tensor decomposition using the LRT image model. Here the 3-way tensor $\mathcal{X}$ with one spatial dimension and two time dimensions — one representing the T1 recovery and the other representing cardiac motion — can be factorized into three factor matrices containing respective basis functions that are weighted by a core tensor $\mathcal{C}$.

where the subscript (1) denotes mode-1 unfolding or flattening of of the tensor into a matrix[77], $\otimes$ denotes the Kronecker product, and $\mathbf{\Phi}$ is the multidimensional temporal factor matrix containing multidimensional temporal basis functions $\{\varphi_j(t_1, t_2, \dots, t_N)\}_{j=1}^{J}$. Figure 12 illustrates a typical 3-way myocardial image tensor formulation that consists of one spatial dimension and two time dimensions modeling the T1 recovery process and the cardiac motion process respectively, which can be decomposed into 3 factor matrices that are weighted by a core tensor.

The LRT image model allows MR Multitasking to bypass a common phenomenon in multidimensional imaging known as "curse of dimensionality", where the scan time and data storage memory grow exponentially with higher dimensions. Modeling $\mathcal{X}$ as an LRT drastically reduces the degrees of freedom in $\mathcal{X}$, as there are far fewer elements in the factor matrices and the core tensor than in the full image tensor $\mathcal{X}$, which significantly reduces the sampling requirements and allows sampling rate far beyond the Nyquist rate[69]. Under the LRT image model, the scan time and data memory grow linearly with higher dimensions as opposed to exponentially, which heavily reduces the overall scan time.

2.5.2 Sampling Strategies and Image Reconstruction

Despite that the LRT image model removes the burden of curse of dimensionality, the size of $\mathbf{X}_{(1)}$ still grows exponentially with the number of dimensions. As a result, both the memory required to store $\mathbf{X}_{(1)}$ and the computational resource required to solve $\mathbf{X}_{(1)}$ are impractical. As an alternative, MR Multitasking proposes to solve $\mathbf{U}$ and $\mathbf{\Phi}$ serially instead of directly solving $\mathbf{X}_{(1)}$ with an explicit tensor subspace strategy[69]:

$$\mathbf{U} = \arg\min_{\mathbf{U}} \|\mathbf{d} - \Omega(\mathbf{FSU\Phi})]\|^2 + R_s(\mathbf{U}), \tag{2.14}$$

where $\mathbf{d}$ denotes the collected k-space data, Ω is the sampling operator corresponding to the sampled k-space locations, **F** applies spatial Fourier encoding, **S** contains sensitivity information that applies multichannel encoding, and $R_s(\cdot)$ is an optional spatial regularization function that also leverages compressed sensing.

Image reconstruction according to Eq. (2.14) requires explicit knowledge of $\mathbf{\Phi}$. Because $\mathbf{\Phi}$ combines multiple temporal factor matrices that are weighted by the core tensor, it solely characterizes the temporal dynamic processes with little spatial knowledge. Therefore theoretically, $\mathbf{\Phi}$ can be extracted from a subset of k-space data with wealthy temporal information and limited spatial information. This subset of k-space data, which we refer to as "subspace training data" ($\mathbf{d}_{\text{tr}}$), are frequently and periodically collected only at the center k-space line which contains the strongest energy of k-space to capture the varying image dynamics throughout the entire scan to resolve the time dimensions.

The remaining part of k-space data, which we refer to as "imaging data", are used to recover the spatial information in $\mathbf{U}$. Therefore, the sampling pattern should have appropriate spatial coverage of the k-space to resolve the prescribed spatial resolution and the field of view (FOV). It is also important that the sampling pattern ensures incoherence between the sampling operator and the temporal factor matrices[69]. Therefore, any uniform or periodic sampling strategies that are synchronized with physiological dynamics (i.e., cardiac or respiratory motion) and the periodic repetition of magnetization preparations should be avoided. In practice, radial sampling with golden angle spoke reordering or randomized Cartesian sampling are preferred to guarantee incoherence.

2.5.3 Multidimensional Tensor Subspace Estimation

The periodically collected $\mathbf{d}_{\mathrm{tr}}$ are used to estimate $\boldsymbol{\Phi}$. To do so, the temporal indexes for each time dimension must first be determined for each data entry of $\mathbf{d}_{\mathrm{tr}}$. Physiological motion and bulk motion states can be determined from motion identification algorithms[69]. Temporal stamps within one recovery period, magnetization preparation indexes and multi-echo indexes can be determined according to the specific sequence structure. With the knowledge of these temporal indexes, $\mathbf{d}_{\mathrm{tr}}$ can be reshaped into an $(N+1)$-way tensor $\mathcal{D}_{\mathrm{tr}}$ in the $(\mathbf{k}, t_1, t_2, \ldots, t_N)$-space, where $\mathbf{k}$ indexes the k-space locations (i.e., in this case, only the center k-space line). The nonzero entries in $\mathcal{D}_{\mathrm{tr}}$ cover various combinations of different image dynamics experienced throughout the scan. However, it is likely that not all such combinations are covered in $\mathcal{D}_{\mathrm{tr}}$. For example, a T1 relaxation index does not necessarily experience all cardiac phases and all respiratory positions in a cardiac MR exam. As a result, $\mathcal{D}_{\mathrm{tr}}$ contains zeros entries indicating the missing combinations. However, as $\mathcal{D}_{\mathrm{tr}}$ only consists of the most frequently sampled k-space lines with very limited spatial information, it has far fewer size and much more densely sampled than the entire imaging data, allowing it to be completed via a small-scale LRT completion problem[69]:

$$\mathcal{D}_{\mathrm{tr}} = \arg\min \|\mathbf{d}_{\mathrm{tr}} - \Omega_{\mathrm{tr}}(\mathcal{D}_{\mathrm{tr}})\|^2 + +\lambda \sum_{i=1}^{N+1} \left\|\mathbf{D}_{\mathrm{tr},(i)}\right\|_* + R(\mathcal{D}_{\mathrm{tr}}), \tag{2.15}$$

where Ω_{tr} retains only the sampled combinations in $\mathcal{D}_{\mathrm{tr}}$, λ is the rank regularization parameter, $\|\cdot\|_*$ denotes the nuclear norm, and $R(\cdot)$ is an optional regularization function that enforces other properties of $\mathcal{D}_{\mathrm{tr}}$ (for example, temporal smoothness). Once $\mathcal{D}_{\mathrm{tr}}$ is determined, the core tensor and the temporal factor matrices $\mathbf{V}_1, \ldots, \mathbf{V}_N$ can be extracted from $\mathcal{D}_{\mathrm{tr}}$ via high-order SVD (HOSVD)[78].

Chapter III Three-Dimensional Simultaneous Brain T1, T2, and ADC Mapping with MR Multitasking

3.1 Introduction

Quantitative multi-parametric mapping of relaxation and diffusion has the potential for comprehensive tissue characterization, which is clinically promising for the identification, diagnosis, and follow-up assessment of various neurological diseases, and more. For example, mapping the relaxation parameters T1 and T2 is promising for monitoring tumors in glioblastoma patients and brain tumor characterization[27,28,79,80]. The quantification of diffusion parameters, e.g., ADC, not only differentiates normal brain tissue and brain tumors[81], but also contributes to brain tumor characterization and may also be useful in grading astrocytic tumors[82,83].

Although there are significant clinical benefits of quantifying multiple relaxation and diffusion parameters, T1/T2/ADC mapping are typically performed in separate scans which are not only time-consuming, but also subject to intra-scan mis-registrations due to subject motion. Additionally, the clinical DWI scans used to map ADC mostly adopt single-shot multi-slice EPI acquisition, leading to image distortion and additional challenges in image registration. Simultaneous T1/T2/ADC mapping approaches that produce distortion-free, co-registered maps would be vastly desirable in the clinic.

Joint T1/T2 mapping has recently been achieved using MR Fingerprinting[62], which has been validated in many clinical applications[28,30]. Our group has recently developed a quantitative imaging framework, MR Multitasking, which allows motion-resolved or motion-robust quantitative imaging, including joint T1/T2 mapping, but has yet to be used to quantify ADC[69,70]. Joint T1/T2/ADC mapping methods have also been proposed, such as the dual-echo-steady-state

(DESS) protocol[84]. However, DESS can be significantly sensitive to physiological motion because it relies on the gradients that are placed within each TR to generate diffusion contrast. MR-Fingerprinting-based[85] and stimulated-echo-based (STEM)[60] approaches are also proposed. However, these methods do not provide a comprehensive quantification of ADC because they only measure diffusion along a single direction. Hutter et al. proposed an integrated approach (ZEBRA)[86] to quantify T1/T2*/ADC simultaneously which demonstrated the efficiency and sampling flexibility but employed single-shot EPI readout that may suffer from B0-inhomogeneity which compromises high resolution image quality and leads to image distortion.

In this work we extend the MR Multitasking framework to achieve a 3D simultaneous brain T1/T2/ADC mapping in <10min which is a feasible duration for clinical practice. This augmentation of the MR Multitasking framework conceptualizes the overlapping image dynamics to be quantified as different temporal dimensions[69] and uses a low-rank tensor (LRT) model[75] to accelerate imaging by exploiting the high spatiotemporal correlation of images corresponding to different T1 weightings, T2-prep durations, b-values and diffusion directions. A time-resolved phase correction technique, which is allowed by the high temporal resolution of the Multitasking framework, is applied along with a separate "real-time" low-rank matrix imaging model to compensate for the inter-shot phase inconsistencies resulting from physiological motion and/or eddy currents, by modeling the phase inconsistencies in a time-resolved phase map[87,88]. We demonstrate that the proposed method enables fully quantitative T1/T2/ADC mapping of the brain with clinically acceptable image resolution ($1.5 \times 1.5 \times 5 \text{mm}^3$) and scan time (<10min).

3.2 Methods

3.2.1 Sequence Design

In this work, we generate multiple T1-T2-diffusion weighting by concatenating a series of T2-prep with different durations τ and a series of D-prep with a fixed duration but different b-values b and diffusion directions d (Figure 13A). The duration of one of the T2-prep matches the duration of the D-prep, so that this T2-prep also serves as a b=0 D-prep. For all the D-prep, two unipolar diffusion-weighted gradients are placed on each side of the 180° adiabatic refocusing pulse. A 3D segmented fast low angle shot (FLASH) readout is used to sample the k-space data.

The magnetization preparation module uses a 90° tip-up pulse to store the prepared signal in the longitudinal magnetization. The accumulated phase generated by the preparation will also be tipped onto z-axis, adding a cosine term to the magnitude. In practice, even two identical preparations may generate different phase patterns because of physiological motion and bulk motion, which is especially common for diffusion-preparations[89]. Consequently, such inconsistent phase patterns would convert to magnitude inconsistency that can never be recovered[89,90]. We employ a crusher gradient scheme that has been proposed to address this issue[55,56,89-91]. An 8π crusher gradient is placed immediately before the 90° tip-up pulse to completely dephase the transverse magnetization, creating a uniform phase dispersion. The same crusher gradient with opposite polarity is placed immediately after each FLASH pulse to rephase the transverse magnetization that was stored in the z-axis and encoded with the phase of the preparation, and to remove the longitudinal magnetization that arises from free relaxation, thus forming the echo that retains the phase of the preparation and maintains the magnitude consistency[90]. However, the penalty of using the crusher gradient scheme is a loss of SNR because the spoiler gradient removes half of the overall signal (those remaining in the transverse plane), and the longitudinal magnetization that contributes to the echo formulation (those encoded with the phase of the preparation) follows a monotonic T1 decay[91]. To counteract this loss in SNR, we add a gap in acquisition immediately prior to each preparation, to allow sufficient signal recovery of long-T1 tissues towards thermal equilibrium. The resulting signal equations after T2-prep and D-preparation are:

$$S_n = \frac{1}{2} \cdot A \cdot e^{-\frac{TR}{T_1}} \cdot \left(e^{-\frac{TR}{T1}} \cos(\alpha)\right)^{n-1} \cdot e^{-\frac{\tau}{T2}} \cdot \sin(\alpha), \tag{3.1}$$

and

$$S_n = \frac{1}{2} \cdot A \cdot e^{-\frac{TR}{T_1}} \cdot \left(e^{-\frac{TR}{T1}} \cos(\alpha)\right)^{n-1} \cdot e^{-\frac{\tau}{T2}} \cdot e^{-bD} \cdot \sin(\alpha), \tag{3.2}$$

respectively, where A absorbs overall coil sensitivity, proton density and T2* weighting, n is the readout index (resetting with each preparation pulse) indicating different T1 weightings, α is the FLASH flip angle, D represents the diffusion coefficient associated with d. By employing the crusher gradient scheme, the magnitude consistency is guaranteed. Some shot-to-shot phase inconsistency still remains, which we address in our proposed imaging model.

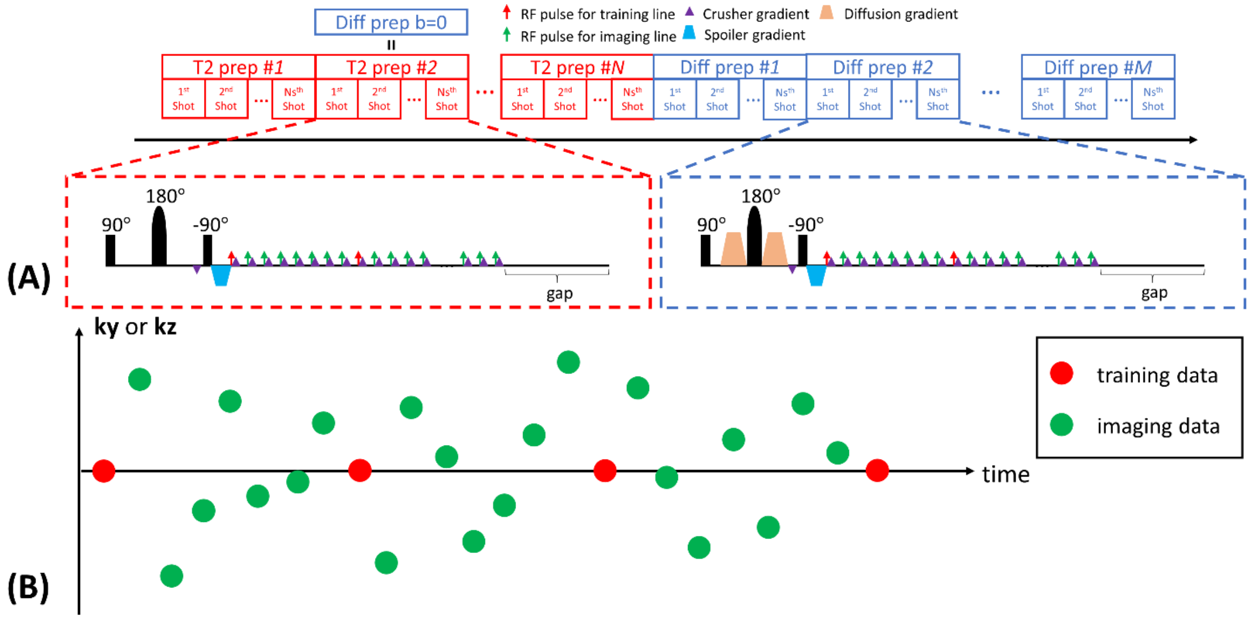

Figure 13. (A) The sequence diagram of the Multitasking framework. A series of T2preps with different durations are concatenated with a series of diffusion-preparations with different b-values and directions. The duration of one of the T2prep matches the duration of the diffusion prep, so that this T2prep also serves as a b=0 diffusion prep. The crusher gradient scheme is used to avoid tipping inconsistent phase errors onto the longitudinal magnetization and maintain the magnitude consistency by complete dephasing before the tip-up pulse and subsequent rephasing immediately before each readout. A 3D segmented FLASH readout is used for data acquisition. A gap is placed immediately prior to each preparation to allow sufficient signal recovery. (B) The k-space sampling illustration. Imaging data are collected using 3D random Cartesian trajectory with Gaussian variable density along phase encoding (ky) and partition encoding (kz) direction. Subspace training data are collected every 8 readouts for temporal subspace estimation.

3.2.2 Image Model

The underlying image can be represented as a 5-way tensor $\mathcal{X}$ with the first dimension concatenating all voxel locations $\mathbf{r} = [x, y, z]$) , and the other four dimensions indexing the four timing/parameter variables n, τ, b, and d respectively. The illustration of the multidimensional low-rank tensor is shown in Figure 14. This LRT structure of $\mathcal{X}$ can be explicitly expressed through matrix factorization as:

$$\mathbf{X}_{(1)} = \mathbf{U}\mathbf{\Phi}, \tag{3.3}$$

$$\mathbf{\Phi} = \mathbf{C}_{(1)}(\mathbf{H} \otimes \mathbf{G} \otimes \mathbf{W} \otimes \mathbf{V})^T, \tag{3.4}$$

where the columns of $\mathbf{U}$, $\mathbf{V}$, $\mathbf{W}$, $\mathbf{G}$, $\mathbf{H}$ are factor matrices containing basis functions spanning the spatial, T1, T2, b-value and diffusion direction subspaces, respectively, and the J rows of $\mathbf{\Phi}$ span the multi-dynamic subspace.

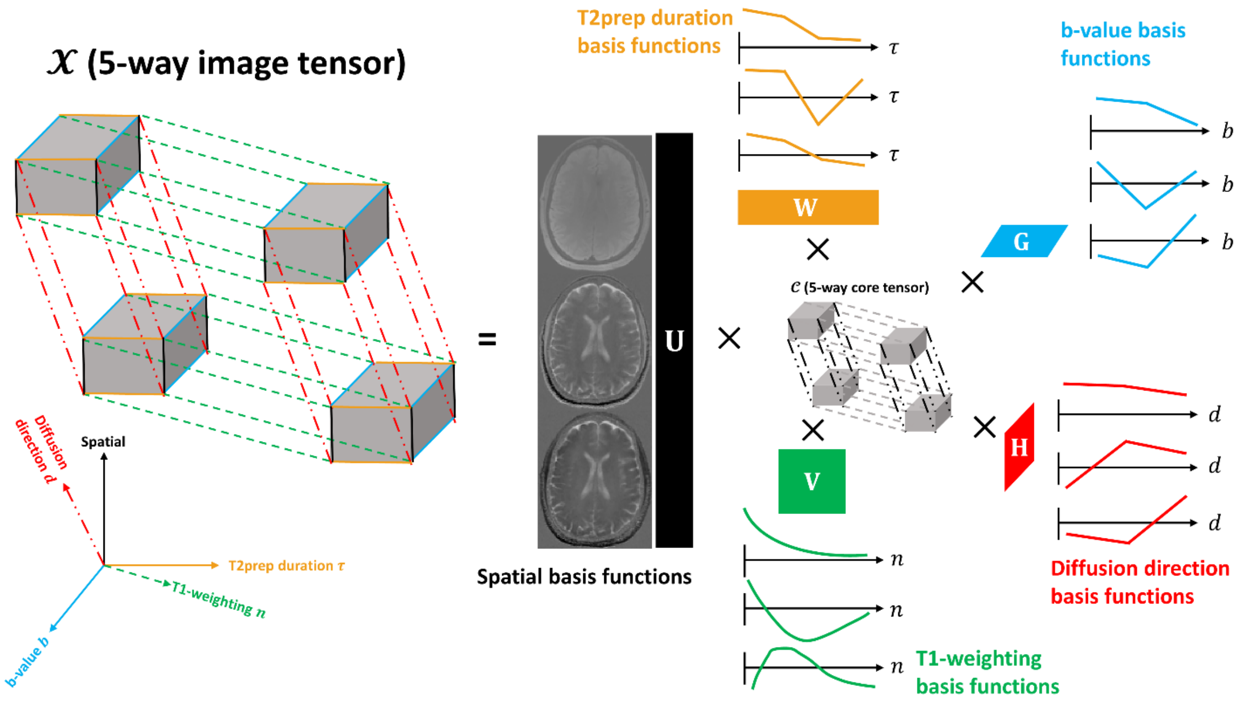

Figure 14. Illustration of multiple temporal dimensions of the 5-way low-rank tensor for simultaneous T1, T2, and ADC mapping. The 5-way image tensor contains spatial, T1-weighting, T2-prep duration, b-value and diffusion direction dimensions. The low-rank tensor structure can be explicitly expressed through tensor factorization between 5 sets of basis functions assigned to each dimension and the 5-way core tensor governing the interaction between different basis functions. Here only the three most significant basis functions describing each dimension of the tensor are provided.

In practice, $(\mathbf{k}, t)$-space data are collected with a single "real-time" dimension t from an underlying image $x_{\mathrm{rt}}(\mathbf{r}, t) = p(\mathbf{r}, t)x\big(\mathbf{r}, n(t), \tau(t), b(t), d(t)\big)$, which experiences phase inconsistencies over time, as modeled by a unit-magnitude phase map $p(\boldsymbol{r}, t)$. Note that the functions $n(t)$, $\tau(t)$, $b(t)$, and $d(t)$ describe the timing/parameter schedule throughout the experiment. Low-rank structure of x_{rt} in the so-called “real-time” domain can also be expressed, as:

$$\mathbf{X}_{\mathrm{rt}} = \mathbf{U}_{\mathrm{rt}}\mathbf{\Phi}_{\mathrm{rt}}, \tag{3.5}$$

where $\mathbf{X}_{\mathrm{rt}}$ is the image matrix corresponding to $x_{\mathrm{rt}}(\mathbf{r}, t)$; where the J' rows of $\mathbf{\Phi}_{\mathrm{rt}}$ span the real-time subspace (as they describe the continuous dynamic processes of the measured signals); and where the J' columns of $\mathbf{U}_{\mathrm{rt}}$ span the spatial subspace containing the real-time image. We note that because $\mathbf{X}_{\mathrm{rt}}$ includes the contribution of phase inconsistencies over time, whereas $\mathcal{X}$ and $\mathbf{X}_{(1)}$ do not, Eqs. (3.3) and (3.5) represent two different image models, both of which will be useful during different stages of image reconstruction.

Phase inconsistencies reduce image correlation and increase image rank[88], so the real-time subspace is generally higher-dimensional than the multi-dynamic subspace, i.e., $J' > J$. Here, the time-resolved, unit-magnitude phase map $p(\mathbf{r}, t)$ is represented in matrix form as $\mathbf{P} \in \{\mathbb{C}^{N_v \times N_t}: |P_{jk}| = 1, \forall j, k\}$, where N_v and N_t denote the number of voxels and number of time stamps respectively, similarly to what we previously proposed for cardiac diffusion tensor imaging[88]. The approximation connecting the real-time subspace model and the multi-dynamic subspace model is therefore:

$$\mathbf{U}_{\mathrm{rt}}\mathbf{\Phi}_{\mathrm{rt}} \approx \mathbf{P} \circ \left(\mathbf{X}_{(1)}\mathbf{R}\right) = \mathbf{P} \circ (\mathbf{U}(\mathbf{\Phi}\mathbf{R})), \tag{3.6}$$

where $\circ$ denotes Hadamard (elementwise) multiplication. The multi-dynamic to real-time reordering matrix is $\mathbf{R} \in \mathbb{R}^{(N_n N_\tau N_b N_d) \times N_t}$ where N_n, N_τ, N_b, N_d denotes the total number of T1-weightings, T2-prep durations, b-values and diffusion directions, respectively. R_{jk} is equal to 1 if the (n, τ, b, d) sequence parameter combination corresponding to the j-th column of $\mathbf{X}_{(1)}$ was collected by the k-th readout and equal to 0 otherwise.

3.2.3 K-Space Sampling

In this work, the imaging data ($\mathbf{d}_{\mathrm{img}}$) are collected using a 3D Cartesian trajectory with Gaussian random variable density along the phase encoding direction ($\mathbf{k}_y$) and partition encoding direction ($\mathbf{k}_z$) to increase sampling incoherence. The subspace training data ($\mathbf{d}_{\mathrm{tr}}$) are frequently collected at the k-space center line (i.e., $\mathbf{k}_y = \mathbf{k}_z = 0$) every 8 readouts to capture the overlapping image dynamics containing T1 weightings, T2-prep durations, b-values and diffusion directions (Figure 13B).

3.2.4 Image Reconstruction

In this work we augment the reconstruction strategy described in the original MR Multitasking framework[69] with an additional time-resolved phase correction component. We propose to serially estimate **P**, **Φ** and **U** following four steps:

1) Estimate a heuristic **P**: The time-resolved phase map **P** is estimated from $\mathbf{I}_0$, a preliminary least-squares reconstruction enforcing the real-time subspace model (i.e., Eq. (3.5)):

$$\mathbf{P} = \angle \mathbf{I}_0 \text{ with } \mathbf{I}_0 = \mathbf{U}_{\mathrm{rt},0}\boldsymbol{\Phi}_{\mathrm{rt},0} \text{ and } \mathbf{U}_{\mathrm{rt},0} = \arg\min_{\mathbf{U}_{\mathrm{rt},0}} \left\| \mathbf{d}_{\mathrm{img}} - \Omega(\mathbf{FSU}_{\mathrm{rt},0}\boldsymbol{\Phi}_{\mathrm{rt},0}) \right\|^2, \quad (3.7)$$

where the real-time temporal basis functions $\boldsymbol{\Phi}_{\mathrm{rt},0}$ are estimated from the singular value decomposition (SVD) of the subspace training data $\mathbf{d}_{\mathrm{tr}}$, Ω denotes the undersampling operator, **F** performs Fourier encoding, and **S** represents the coil sensitivity matrix.

2) Pre-determine T1 factor matrix **V**: Because the T1 relaxation is physically governed by the Bloch equations, a set of feasible signal curves following a T1 decay pattern can be pre-

determined ahead of time to generate a T1 relaxation training dictionary[92-94] using a range of T1 values and flip angles. Specifically, we use 101 T1 values logarithmically spaced from 100ms to 3000ms, and 15 FLASH flip angles equally spaced from 0.5 ° to 7.5 ° representing 90% underestimation to 50% overestimation of the prescribed flip angle covering a possible range of B1 inhomogeneities. A total of 1515 T1 decay signal curves are generated to construct a training dictionary, the SVD of which produces the T1 decay basis functions in $\mathbf{V}$.

3) Estimate a heuristic multi-dynamic $\mathbf{\Phi}$: In the original MR Multitasking framework, the subspace training data $\mathbf{d}_{\text{tr}}$ are binned (i.e., mapped from the real-time domain to the multi-dynamic domain) to form a training tensor $\mathcal{D}_{\text{tr}}$[69]. However, in this work, naively mapping $\mathbf{d}_{\text{tr}}$ from the real-time $(\mathbf{k}, t)$-space to the multi-dynamic $(\mathbf{k}, n, \tau, b, d)$-space without accounting for the inconsistent phase patterns would result in signal cancellation in $\mathcal{D}_{\text{tr}}$. As an alternative, we use features extracted from the real-time magnitude images $|\mathbf{I}_0|$ as the new subspace training data, i.e., we define a matrix of training data $\mathbf{T} \in \mathbb{C}^{J' \times N_t}$ from the $J' > J$ most significant right singular vectors of $|\mathbf{I}_0|$. The training tensor $\mathcal{D}_{\text{tr}}$ can be solved via a Bloch-constrained small-scale LRT completion problem:

$$\hat{\mathcal{D}}_{\text{tr}} = \arg\min_{\mathbf{D}_{\text{tr},(2)} \in \text{range}(\mathbf{V})} \left\|\mathbf{T} - \mathbf{D}_{\text{tr},(1)}\mathbf{R}\right\|^2 + \lambda\left(\left\|\mathbf{D}_{\text{tr},(1)}\right\|_* + \textstyle\sum_{n=3}^{5}\left\|\mathbf{D}_{\text{tr},(n)}\right\|_*\right) + R(\mathcal{D}_{\text{tr}}), \quad (3.8)$$

where $R(\cdot)$ penalizes total variation (TV) along the diffusion direction dimension. Once $\hat{\mathcal{D}}_{\text{tr}}$ is completed, $\mathbf{\Phi} = \mathbf{C}_{(1)}(\mathbf{H} \otimes \mathbf{G} \otimes \mathbf{W} \otimes \mathbf{V})^T$ can be quickly extracted from $\hat{\mathcal{D}}_{\text{tr}}$ via HOSVD[78].

4) Obtain the spatial factor matrix $\mathbf{U}$. With the heuristic $\mathbf{P}$ and $\mathbf{\Phi}$, the remaining unknown $\mathbf{U}$ could in principle be directly recovered by incorporating the phase correction into the multi-dynamic imaging model (i.e., Eq. (3.6)):

$$\hat{\mathbf{U}} = \arg\min_{\mathbf{U}} \left\| \mathbf{d}_{\mathrm{img}} - \Omega(\mathbf{FS}[\mathbf{P} \circ (\mathbf{U}[\mathbf{\Phi R}])) \right\|^2 + R_s(\mathbf{U}), \tag{3.9}$$

where $R_s(\cdot)$ is an optional additional spatial constraint, e.g., which also leverages compressed sensing. However, solving this iterative optimization problem directly as posed above would involve storing and manipulating many real-time $N_v \times N_t$ matrices—not just **P** but also auxiliary variables used during optimization—and can therefore require large amounts of memory.

In practice, rather than solving Eq. (3.9), we instead solve an alternative optimization problem that additionally relies on the memory-efficient image model in Eq. (3.5). We first enforce the real-time subspace model to obtain a phase-varying $\mathbf{\Phi}_{\mathrm{rt}}$ (which incorporates some phase variation from $\mathbf{P}$) and $\mathbf{U}_{\mathrm{rt}}$, then we obtain **U** by mapping the result back to the multi-dynamic subspace model according to Eq. (3.6). This is achieved via three sub-steps:

4.1) Map $\mathbf{\Phi}$ back to the phase-varying real-time subspace by incorporating phase information from **P** into a heuristic $\mathbf{\Phi}_{\mathrm{rt}}$. Note that as is, $\mathbf{\Phi}$ lies in the phase-corrected multi-dynamic domain, which is free from phase inconsistencies. We first map $\mathbf{\Phi}$ onto the phase-corrected real-time subspace as $\mathbf{\Phi R}$, then we project the phase-free $|\mathbf{I}_0|$ onto this subspace. This provides the best approximation of the initial magnitude image in the phase-corrected real-time subspace:

$$\mathbf{I}_{\mathrm{rt}} = |\mathbf{I}_0|(\mathbf{\Phi R})^{+}(\mathbf{\Phi R}), \tag{3.10}$$

where $^{+}$ denotes the pseudoinverse. We then apply the time-resolved phase map **P** to include the phase-varying information, and finally calculate the SVD of the resulting phase-varying real-time image, i.e.,

$$\mathbf{\Phi}_{\mathrm{rt}} \leftarrow \mathrm{SVD}(\mathbf{P} \circ \mathbf{I}_{\mathrm{rt}}), \tag{3.11}$$

This new basis $\mathbf{\Phi}_{\mathrm{rt}}$ reflects the phase inconsistencies in the real-time subspace as well as the multi-dynamic modeling performed in step (3).

4.2) Recover $\mathbf{U}_{\mathrm{rt}}$ using the real-time subspace model (i.e., Eq. (3.5)). With heuristic $\mathbf{\Phi}_{\mathrm{rt}}$, the coordinates in the phase-varying real-time subspace, $\mathbf{U}_{\mathrm{rt}}$, can be recovered as:

$$\mathbf{U}_{\mathrm{rt}} = \arg\min_{\mathbf{U}_{\mathrm{rt}}} \left\| \mathbf{d}_{\mathrm{img}} - \Omega(\mathbf{FSU}_{\mathrm{rt}}\mathbf{\Phi}_{\mathrm{rt}})) \right\|^2 + R_s(\mathbf{U}_{\mathrm{rt}}), \tag{3.12}$$

which without the explicit phase map can be entirely solved in the J'-dimensional real-time subspace rather than the much more memory-intensive $(\mathbf{r}, t)$-space, due to the block diagonal structure of $A(\cdot) = \Omega^*\Omega\big((\cdot)\mathbf{\Phi}_{\mathrm{rt}}\big)\mathbf{\Phi}_{\mathrm{rt}}^{H}$[95,96]. Here $R_s(\cdot)$ is chosen as a spatial TV penalty.

4.3) Obtain $\mathbf{U}$. We map the spatial coefficients from the J'-dimensional phase-varying real-time subspace to the J-dimensional phase-corrected multi-dynamic subspace, i.e., $\mathbf{U}_{\mathrm{rt}} \rightarrow \mathbf{U}$. This mapping is based on Eq. (3.6), and is performed as:

$$\mathbf{U} \approx [\mathbf{P}^* \circ (\mathbf{U}_{\mathrm{rt}}\mathbf{\Phi}_{\mathrm{rt}})](\mathbf{\Phi}\mathbf{R})^+. \tag{3.13}$$

Note that Eq. (3.13) relies on both image models described in Eq. (3.3) and Eq. (3.5), whereas Eq. (3.9) only uses the multi-dynamic image model described in Eq. (3.3). Eq. (3.13) therefore does not directly approximate Eq. (3.9), but rather finds alternative coordinates in the phase-corrected multi-dynamic subspace by a mapping from coordinates in the phase-varying real-time subspace. The operations in Eqs. (3.10) and (3.13) map between two distinct image models: the multi-dynamic subspace model and the phase-varying real-time subspace model. A solution satisfying both models typically only exists when J' is selected high enough to fully represent the phase variation in $p(\mathbf{r}, t)$; however, for lower values of J' as used in practice, a solution exactly satisfying both models may not exist, and the mappings in Eqs. (3.10) and (3.13) modify the solution.

3.2.5 Phantom Study

To evaluate the T1/T2/ADC mapping accuracy of the proposed method, an ISMRM/NIST T1/T2 phantom (Model 130, High Precision Devices) and a diffusion phantom (Model 128, High Precision Devices) were scanned on a 3T scanner (MAGNETOM Vida, Siemens Healthineers) using a 64-channel head coil. Because the T1/T2 phantom lacked ADC variety, we performed ADC mapping on the diffusion phantom as well. Reference T1/T2/ADC maps were obtained via an inversion recovery turbo spin echo (IR-TSE) sequence, a multi-echo spin echo (ME-SE) sequence and a DW-SSEPI sequence, respectively. The Multitasking sequence was implemented with 7 T2-prep and 6 D-prep. Each preparation is repeated 10 times before the next preparation is implemented. The detailed imaging protocol is in Table 2.

Table 2. Phantom imaging protocols and scan parameters for simultaneous brain T1/T2/ADC mapping.

Phantom Imaging Protocols	
IR-TSE (17.5min)	FOV=280x280mm^2, in-plane resolution=1.5x1.5mm^2, slice thickness=5mm, number of slices=10, TR=3500ms, TE=8.3ms, TIs=[50,100,200,275,350,500,650,800,950,1200,1500,1800,2100,2500,3000,3500]ms
ME-SE (5.0min)	FOV=240x240mm^2, in-plane resolution=1.7x1.7mm^2, slice thickness=5mm, number of slices=10, TR=3050ms, TEs=[20,40,60,80,100,120,140]ms
SS-EPI (1.7min)	FOV=240x240mm^2, in-plane resolution=1.5x1.5mm^2, slice thickness=5mm, number of slices=10, TR=5800ms, TE=88ms, b-values=[0,400,800]s/mm^2, averages=[2,2,2]
Multitasking (6.1min)	FOV=240x240mm^2, in-plane resolution=1.5x1.5mm^2, slice thickness=5mm, number of partitions=10, FLASH TR/TE=5.78/2.8ms, flip angle=5°, readout lines per shot=320, TR per shot=2800ms, gap=1s, T2prep durations=[13.62,31.4,45,64,80,100,120]ms, b-values =[400,800]s/mm^2, 3 diffusion directions: [1 1 -1], [1 -1 1], [-1 1 1]

3.2.6 In Vivo Study

The in vivo study was approved by the institutional review board (IRB) of our institute. All volunteers/patients gave written informed consent before the study. Sixteen healthy volunteers were recruited and were scanned also on Vida scanner. Localizers were implemented to locate the volume of interest which covered from the top of the brain to the pons. Reference T1/T2/ADC maps were obtained via IR-TSE, ME-SE, and DW-SSEPI respectively. The total scan time of references was 19min. The Multitasking sequence was implemented with 4 T2-prep and 6 D-prep. Each preparation is repeated 20 times before the next preparation is implemented, resulting in a total scan time of 9.3min. The approximately maximum diffusion encoding gradient amplitude (55mT/m) was turned on to shorten the diffusion-preparation duration (31.4ms) for SNR purposes. The slice positions of all scans matched exactly. The detailed imaging protocol is in Table 3.

Table 3. In vivo imaging protocols and scan parameters for simultaneous brain T1/T2/ADC mapping.

In Vivo Imaging Protocols	
IR-TSE (12.5min)	FOV=280x280mm^2, in-plane resolution=1.5x1.5mm^2, slice thickness=5mm, number of slices=20, TR=3500ms, TE=8.3ms, TI=[50,100,200,275,350,425,500,1200,1500,1800,2100,2500]ms
ME-SE (5.0min)	FOV=240x240mm^2, in-plane resolution=1.7x1.7mm^2, slice thickness=5mm, number of slices=20, TR=3050ms, TE=[20,40,60,80,100,120,140]ms
SS-EPI (1.7min)	FOV=240x240mm^2, in-plane resolution=1.5x1.5mm^2, slice thickness=5mm, number of slices=20, TR=5800ms, TE=88ms, b-value=[0,400,800]s/mm^2, averages=[2,2,2]
Multitasking (9.3min)	FOV=240x240mm^2, in-plane resolution=1.5x1.5mm^2, slice thickness=5mm, number of partitions=20, FLASH TR/TE=5.78/2.8ms, flip angle=5°, readout lines per shot=320, TR per shot =2800ms, gap=1s, T2prep durations for healthy volunteer study=[13.62,31.4,80,110]ms, T2prep durations for patient study=[13.62,39.6,80,110]ms, b-values =[400,800]s/mm^2, 3 diffusion directions: [1 1 -1], [1 -1 1], [-1 1 1]

In addition, 3 post-surgery patients who were previously diagnosed with a brain tumor and were likely to possess residual/recurrent tumor were scanned on a 3T scanner (MAGNETOM Skyra, Siemens Healthineers) using a 20-channel head coil. The Multitasking scan was incorporated in a clinical brain MRI scan aimed for follow-up assessment before the administration of contrast agents. The clinical protocols included pre-contrast T1w-magnetization prepared rapid gradient echo (MPRAGE), pre-contrast T2w-FLAIR, DW-RSEPI with Siemens' RESOLVE protocol, post-contrast T2w-TSE, and post-contrast T1w-MPRAGE. A relaxed diffusion gradient amplitude (35mT/m) was used to protect the gradient system, resulting in a 39.6ms diffusion-preparation duration.

3.2.7 Exploration of Motion Effects

Head movement is commonly seen during clinical scans because of patient discomfort, which will lead to mis-registration or image artifacts if not properly addressed. Furthermore, the bulk motion will not only affect the magnetization preparation, but also damage the refocusing crusher gradients, resulting in uncorrelated signal or significant signal loss.

We explored the motion effects on our method in four healthy volunteers. For each volunteer, a motion-free scan was performed followed by a motion-corrupted scan. A sticker was placed on the inside of the coil right on top of the subject's nose to fix the initial position. The motion-free scan contained one Multitasking protocol (9.3min), during which the subject was clearly instructed not to move their head. The motion-corrupted scan contained two consecutive Multitasking protocols (18.6min) to span the scan duration so that the subject was likely to move multiple times. The subject was instructed beforehand that he/she could move at will during the motion-corrupted scan, meaning that he/she could perform any type of motion (e.g., itching face, adjusting head position, deep breath, etc.) at any time, instead of being instructed to perform only certain types of motion at certain times explored in Fingerprinting studies[67,68]. This aimed to mimic realistic motion scenario in an actual clinical scan. There are many options for motion handling in the Multitasking framework, including motion-removed imaging, motion-resolved imaging, and motion-compensated imaging. In this study, we performed motion removal to simplify data processing, so the subjects were asked to return to the initial position after each movement.

The motion-free data were reconstructed as a reference. For each of the two motion-corrupted datasets, we identified the amount of corrupted data based on the real-time image series $\mathbf{I}_0$ via manual inspection. Specifically, within each motion-corrupted dataset, all the shots that were observed with the occurrence of motion artifacts were considered motion-corrupted. The percentage of the corrupted data was thus:

$$p_i = \frac{N_{m,i}}{200}, \;\; i = 1,2, \tag{3.14}$$

where $N_{m,i}$ is the number of motion-corrupted shots in the i-th motion-corrupted dataset. We only reconstruct the $\hat{\imath}$-th dataset, where $\hat{\imath} = \arg\max_i p_i$ (i.e., the worse of the two motion-corrupted datasets). Motion removal was performed by removing all $N_{m,\hat{\imath}}$ shots in the $\hat{\imath}$-th dataset from $\mathbf{d}_{\text{tr}}$ and $\mathbf{d}_{\text{img}}$ along with the corresponding sampling locations from Ω and **R**.

3.2.8 Image Analysis

All the reconstructions were performed on a Linux workstation with a 2.70GHz dual 12-core Intel Xeon processor equipped with 256GB RAM and running MATLAB 2017a. Reconstruction parameters (rank of respective dimensions, λ, etc.) are in Table 4.

Table 4. Reconstruction parameters for simultaneous brain T1/T2/ADC mapping.

Reconstruction Parameters	Phantom Study	In vivo Study
Number of voxels N_v	256000	512000
Number of time points N_t	41600	64000
Rank of spatial dimension J (for multi-dynamic subspace modeling)	4	14-16
Rank of spatial dimension J' (for real-time subspace modeling)	5	22-26
Rank of T1-weighting dimension K	5	5
Rank of T2prep duration dimension L	7	4
Rank of b-value dimension M	3	3
Rank of diffusion direction dimension N	3	3
Nuclear norm penalty λ	$5\text{x}10^{-5}$	$1\text{x}10^{-4}$

In this work, the λ used to weight the nuclear norm penalties was chosen based on the discrepancy principle[97] for one dataset and then used for all datasets. The ranks of the spatial and T1 weighting dimensions were determined from the -40dB threshold on the normalized singular value curves of the training dictionary and the full training data respectively. The ranks of the T2-prep duration, b-value, and diffusion direction dimensions were not truncated, as the nuclear norm low-rank constraint implemented for the training tensor completion already performed a soft constraint on the tensor ranks for those dimensions.

For each healthy subject, 3 slices located in the upper, mid, and lower regions of the acquired 3D volume were chosen for voxel-by-voxel multi-parametric fitting of A, α, T1, T2, and the diffusion coefficients of 3 directions D_1, D_2 and D_3 based on Eqs. (3.1) and (3.2). ADC is then derived by:

$$\mathrm{ADC} = (D_1 + D_2 + D_3)/3. \tag{3.15}$$

For qualitative analysis, the following comparisons were made:

1) The proposed method versus no phase correction (i.e., assuming $\mathbf{P} = \mathbf{I}$ and using $\mathbf{d}_{\mathrm{tr}}$ directly for tensor subspace estimation) to evaluate the effectiveness of the proposed phase correction strategy.
2) The proposed method versus reference protocols to evaluate quantification.
3) Motion-free maps, motion-corrupted maps and motion-removed maps to evaluate the motion effect and the behavior of motion removal.

For quantitative analysis in the phantoms, the regions of interest (ROI) were drawn for each vial, and the mean and standard deviation for T1/T2/ADC values in each vial were calculated and compared between Multitasking and the references. In addition, the SNR of each measurement of each vial is assessed as the respective mean value over standard deviation in the vial. The multi-parametric SNR efficiency for Multitasking is assessed as SNR per $(T_{\text{multitasking}}/3)^{1/2}$, where $T_{\text{multitasking}}$ represents the Multitasking scan time. The multi-parametric SNR efficiency for one reference method is assessed as SNR per $(T_{\text{reference}})^{1/2}$, where $T_{\text{reference}}$ represents the specific reference scan time. The $\sqrt{3}$ factor for the multitasking SNR efficiency accounts for all three parameters being of interest but acquired in one single scan.

For quantitative analysis in healthy subjects, 12 regions of interest (ROI) were drawn on the frontal, parietal, and occipital regions of the gray matter (GM) and WM of both left and right hemispheres of the mid slice[98]. ROI of the reference protocols and the Multitasking protocol were drawn at the same locations.

For each patient, the surgery/tumor region was manually identified on the standard clinical protocols. Three slices surrounding the surgery/tumor region were chosen for the multi-parametric fitting and were compared with the standard clinical protocols on approximately matched slice positions.

3.2.9 Statistical Analysis

T1/T2/ADC values of the GM and WM of frontal, parietal, and occipital regions were calculated as the mean values of the corresponding ROIs of the left and right lobes. A three-way repeated measures ANOVA was performed using IBM SPSS Statistics. Specifically, the two tissue types, the three regions and the two methods are all set as within subject variables. The significance level was set as $P<0.05$. Intra-class correlation coefficient (ICC) was calculated using IBM SPSS Statistics with a two-way mixed model and a confidence level of 95% to demonstrate the consistency between Multitasking and the references. Bland-Altman analysis was performed between Multitasking and the references to demonstrate the bias.

3.3 Results

3.3.1 Phantom Study

The proposed Multitasking approach provides good phantom image quality (Figure 15). Multitasking quantitative maps are free from the image distortion present in the DW-SSEPI ADC reference. The measured T1/T2/ADC are in substantial quantitative agreement with references, with $R^2 = 0.999$ and ICC>0.998 for T1/T2/ADC. On average, simultaneous acquisition of T1/T2/ADC using Multitasking provides 2.41x, 1.59x, and 0.72x the multi-parametric SNR efficiency compared to separate acquisition using the respective reference methods (Figure 16). We note that the reference methods were chosen for their accepted accuracy but may not have the optimal SNR efficiency[58].

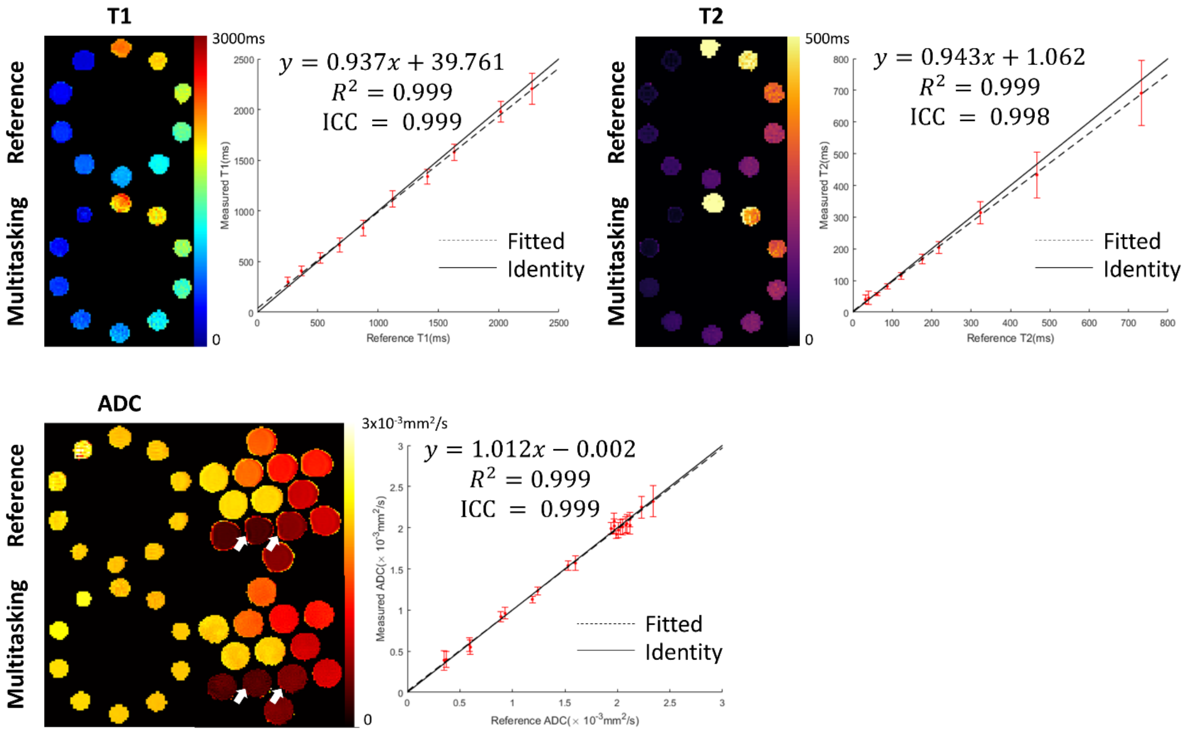

Figure 15. Comparison of T1/T2/ADC mapping between Multitasking and the references. Multitasking provides good image quality with substantial correlation with references and is free from image distortion present in SS-EPI ADC references (white arrows). The solid line represents identity while the dotted line represents the linear fitting. ICC between Multitasking and the references indicates substantial consistency.

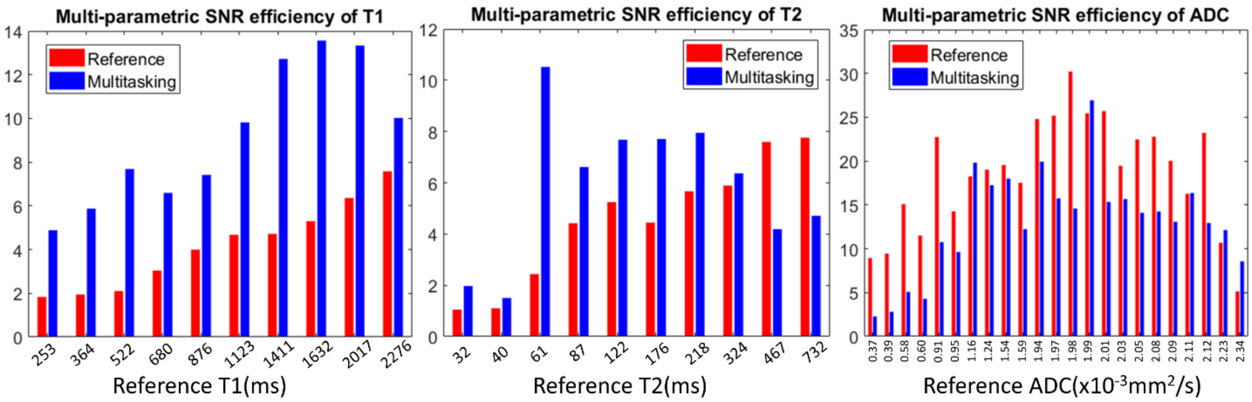

Figure 16. The comparison of the multi-parametric SNR efficiency of T1, T2, and ADC measurements between the reference and Multitasking for each vial. On average, simultaneous acquisition of T1/T2/ADC using Multitasking provides 2.41x, 1.59x, and 0.72x multi-parametric SNR efficiency compared to separate acquisition using the respective reference methods.

3.3.2 In Vivo Study

Figure 17 shows the multidimensional image tensor formulation with respect to each time dimension, which individually demonstrates the dynamic processes of T1 decay, T2 decay, diffusion decay following different b-values, and the change between diffusion directions. When showing image dynamics along one time dimension, the other three time dimensions were at fixed temporal indexes.

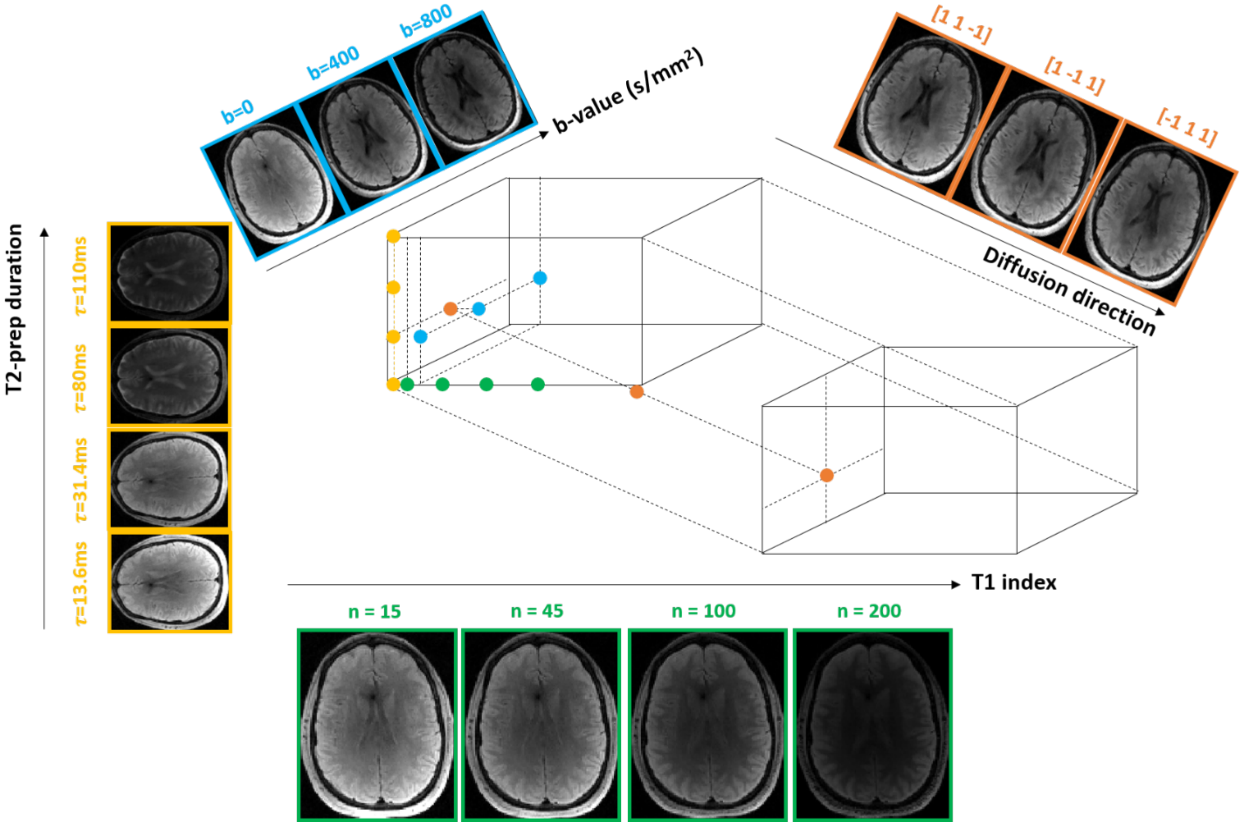

Figure 17. Demonstration of the multidimensional tensor formulation for simultaneous T1, T2, and ADC mapping in the brain. Green color represents different T1 weightings. Yellow color represents different T2 weightings. Blue color represents different diffusion weightings (b-values). Orange color represents different diffusion directions. Solid dots represent the locations of the displayed images in the tensor.

The phase measured at the first time point after each preparation (i.e., $n = 1$) can be extracted from the full time-resolved phase map as a good representation for the phase resulting from the preparation. The phase resulting from the 1st, 10th, and 20th preparation of each type of T2-prep and D-prep demonstrates very little shot-to-shot phase inconsistency between T2-prep and substantial shot-to-shot phase inconsistency between D-prep (Figure 18). The reconstructed T1 and T2 maps using Multitasking with and without phase correction agree with the references. Multitasking ADC maps only agree with the reference when phase correction is used; the ADC maps without phase correction show elevated ADC values across all slices (Figure 19).

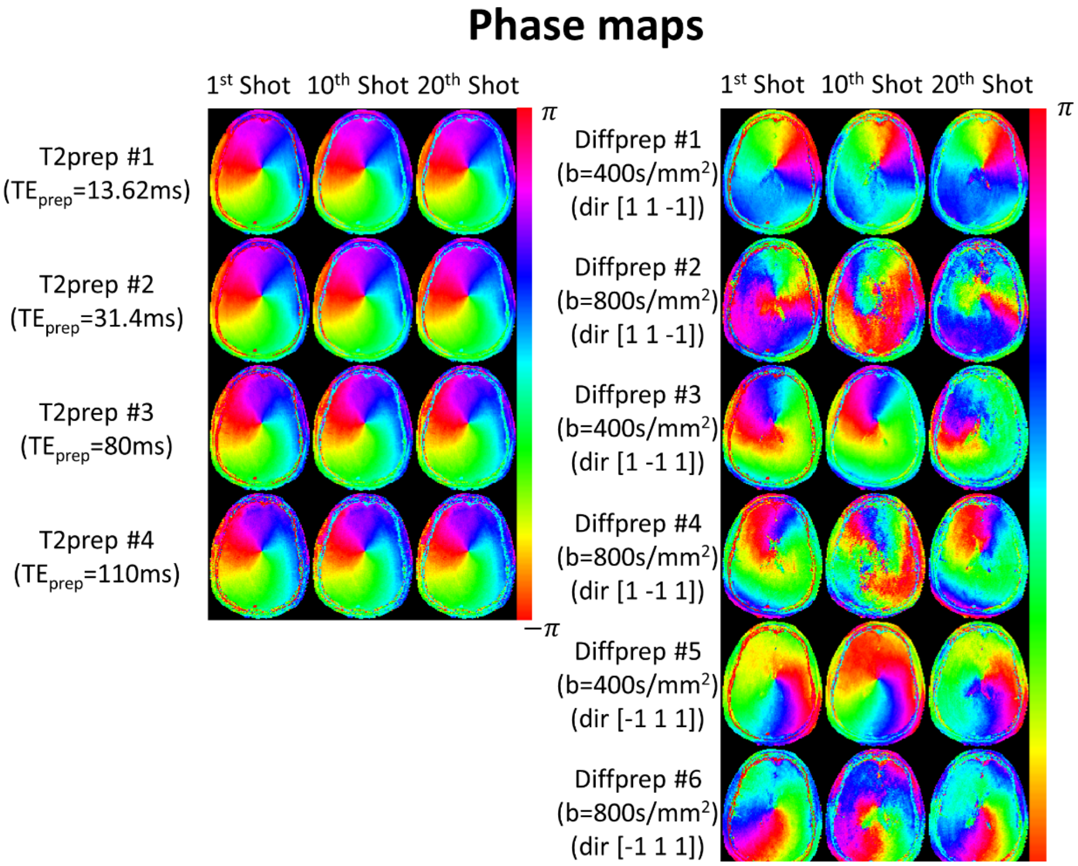

Figure 18. Phase maps at n=1 of the 1st, 10th, and 20th shot of the 4 T2-prep and 6 D-prep extracted from the full time-resolved phase map. For T2-prep, little phase inconsistency can be observed between shots or between different T2-prep. For D-prep, substantial phase inconsistency can be observed between shots or between different D-prep.

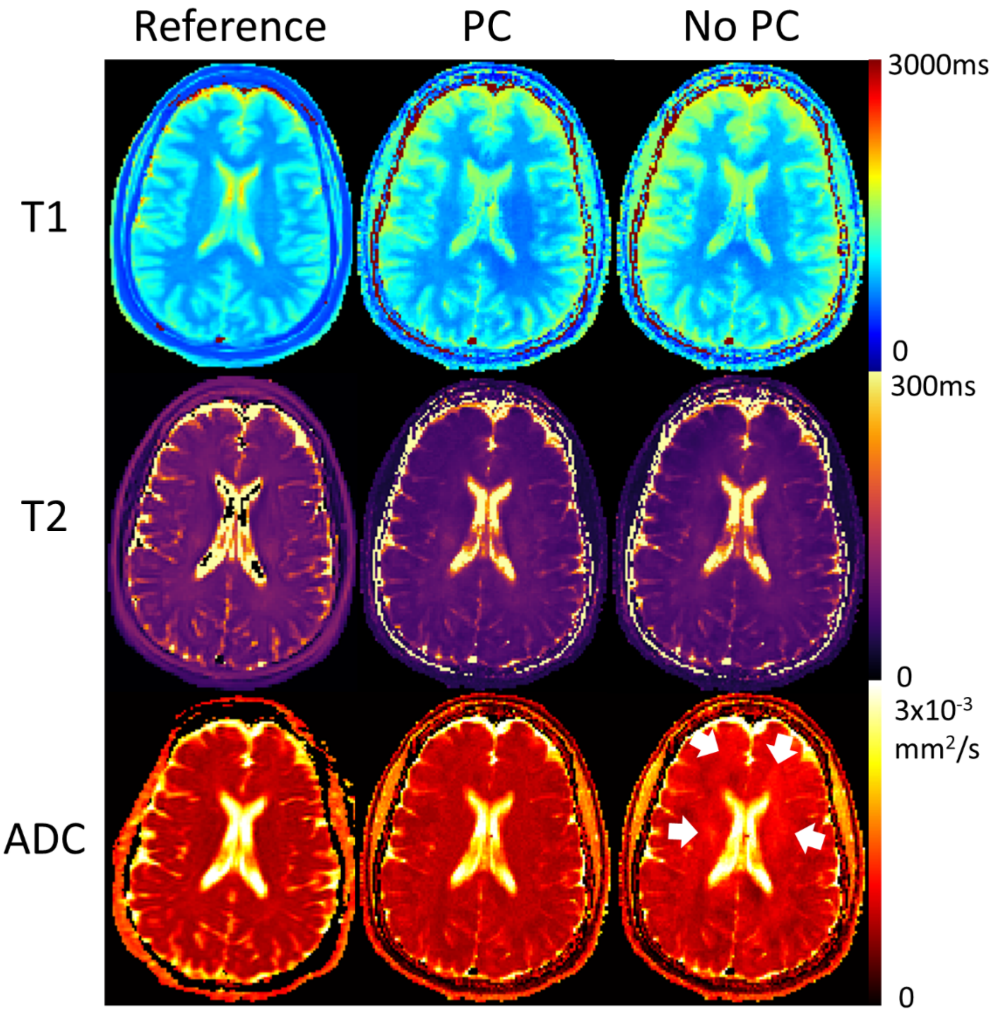

Figure 19. Representative T1/T2/ADC mapping with references, Multitasking with the proposed time-resolved phase correction (PC), and Multitasking without phase correction (No PC). White arrows point to regions with substantial elevation of ADC without phase correction.

Multitasking produces perfectly co-registered and distortion-free T1/T2/ADC maps that qualitatively agree with the references (Figure 20) and produces similar distributions of T1/T2/ADC measurements of GM and WM (Table 5). Some T1 values appear higher compared to IR-TSE, particularly very long T1 species around the brain sulci and fissures. For T2 maps, GM, WM, and cerebrospinal fluid (CSF) are distinguishable but appear slightly lower than ME-SE. ADC values of CSF and around the brain sulci and fissures are also slightly lower than DW-SSEPI. Despite these differences, all the measurements are within the literature range (GM T1:

968-1820ms; WM T1: 750-1110ms; GM T2: 71-132ms; WM T2: 56-84ms; GM ADC: 0.78-1.09x10^{-3}mm^2/s; WM ADC: 0.60-1.05x10^{-3}mm^2/s)[98-101].

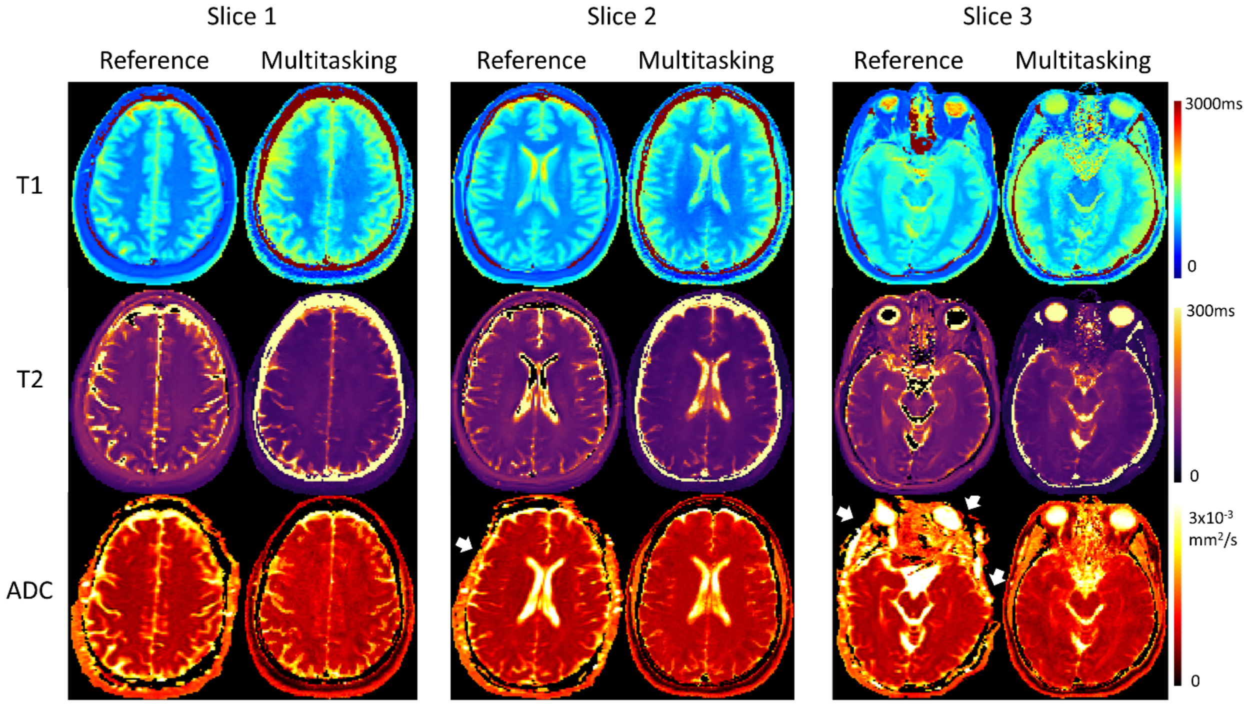

Figure 20. Representative in vivo T1/T2/ADC mapping of 3 slices using Multitasking and the respective reference protocols for a healthy volunteer. Multitasking provides T1/T2/ADC maps with good qualitative agreement with the references, and without image distortion (white arrows) which can be observed on SS-EPI ADC maps.

Table 6 shows the complete three-way ANOVA table, indicating nonsignificant differences between regions for T1 (p=0.248), T2 (P=0.097), and ADC (P=0.328), significant differences between tissues for all parameters (P<0.001), and significant differences of T1 (P=0.03), T2 (P<0.001), and ADC (P=0.001) biases between Multitasking and the respective references. Despite the statistical significance of these biases, the Bland-Altman plots show that the mean bias estimates are small ($\Delta T1\% < 5\%$, $\Delta T2\% < 7\%$, $\Delta ADC\% < 5\%$) (Figure 21), and all ICC measurements are >0.82, well within the established "excellent" range (ICC>0.75)[102] (Table 7).

Table 5. Frontal, parietal, and occipital gray matter and white matter T1/T2/ADC measurements of 16 healthy volunteers using Multitasking and the references.

Gray Matter Measurements (n=16)						
	Frontal		Parietal		Occipital	
	Multitasking	Reference	Multitasking	Reference	Multitasking	Reference
T1(ms)	1250.6±52.5	1225.9±40.9	1231.8±40.5	1223.9±39.8	1205.8±43.1	1205.4±40.4
T2(ms)	97.8±5.7	105.8±5.7	96.9±5.5	104.8±5.2	98.7±6.1	104.1±5.0
ADC(x10^{-3}mm^2/s)	0.95±0.05	0.92±0.04	0.92±0.08	0.91±0.06	0.95±0.08	0.93±0.07
White Matter Measurements (n=16)						
	Frontal		Parietal		Occipital	
	Multitasking	Reference	Multitasking	Reference	Multitasking	Reference
T1(ms)	807.4±39.1	792.9±45.1	811.9±40.6	811.3±40.4	820.2±41.0	814.5±38.7
T2(ms)	71.3±4.8	78.5±4.6	78.2±4.2	82.1±4.9	74.4±4.5	80.3±3.4
ADC(x10^{-3}mm^2/s)	0.80±0.03	0.77±0.03	0.80±0.04	0.77±0.04	0.78±0.04	0.75±0.04

Identifying motion from $\mathbf{I}_0$ is straightforward, as motion-corrupted images are subject to significant signal loss and image artifacts. After motion removal, artifacts and signal voids are removed (Figure 22). T1/T2/ADC mapping from two subjects are shown. For the first subject, 20% of the measured data are corrupted by motion. Specifically, 39% T2-prep are corrupted, and 8% D-prep are corrupted. With motion-corrupted data left in for reconstruction, the T1 map exhibits blurring artifacts, the T2 map and the ADC map show elevated T2 and ADC values, resulting in root-mean-squared-error (RMSE) of 140.40ms, 14.85ms, and 0.17x10^{-3}mm^2/s respectively. After

Table 6. Three-way repeated measures ANOVA table for T1, T2, and ADC indicating nonsignificant differences between regions and significant differences between tissues and acquisition methods.

	Source	Sum of Squares	Degrees of Freedom	Mean Square	F	P
T1	Region	2659.042	2	1329.521	1.462	0.248
	Tissue	8229492.188	1	8229492.188	2592.094	<0.001
	Method	3745.333	1	3745.333	5.707	0.030
T2	Region	69.064	2	34.532	3.140	0.097
	Tissue	28643.198	1	28643.198	456.974	<0.001
	Method	2074.413	1	2074.413	491.658	<0.001
ADC	Region	0.006	2	0.003	1.159	0.328
	Tissue	1.049	1	1.049	126.833	<0.001
	Method	0.035	1	0.035	50.133	0.001

Region: Frontal, parietal, occipital; Tissue: Gray matter, white matter; Method: Multitasking and the reference

motion removal, T1 features are restored and motion artifacts are removed. Abnormal T2 and ADC values on most regions are restored. RMSE drop to 92.83ms, 7.60ms, and 0.13x10^{-3}mm^{2}/s respectively (Figure 23). For the second subject, 33% of data are corrupted by motion. Specifically, 21% T2-prep are corrupted, and 40% D-prep are corrupted. T1 and T2 maps with motion do not exhibit substantial differences compared against the motion-free case. However, significantly elevated ADC values result from motion. RMSE are 97.07ms, 8.58ms, and 0.23x10^{-3}mm^{2}/s

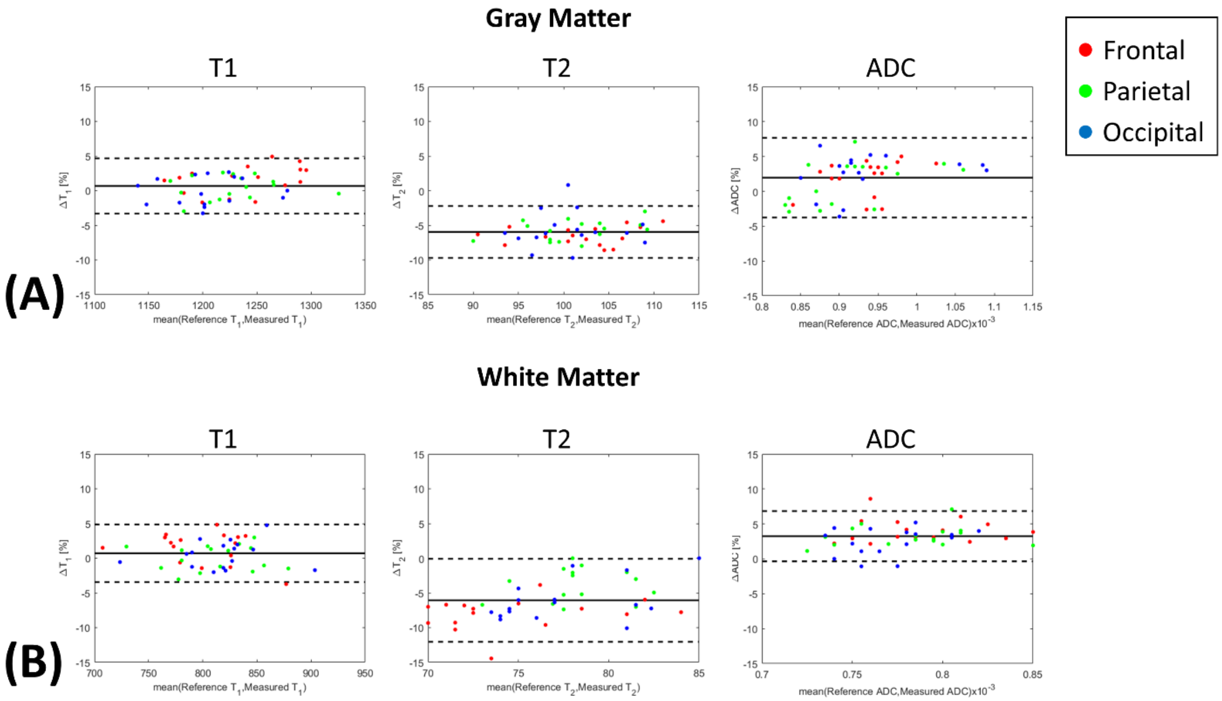

Figure 21. (A) Gray matter and (B) white matter Bland-Altman plots of frontal, parietal, and occipital T1/T2/ADC.

Table 7. Intra-class correlation coefficients of frontal, parietal, occipital gray matter and white matter T1/T2/ADC between Multitasking and the references.

Gray Matter Intra-Class Correlation Coefficients			
	Frontal	Parietal	Occipital
T1	0.88	0.93	0.86
T2	0.98	0.97	0.88
ADC	0.89	0.93	0.95
White Matter Intra-Class Correlation Coefficients			
	Frontal	Parietal	Occipital
T1	0.92	0.95	0.93
T2	0.88	0.82	0.87
ADC	0.94	0.91	0.87

respectively under motion. After motion removal, ADC values in most regions are again restored and RMSE drop to 89.51ms, 7.11ms, 0.10x10^{-3}mm^2/s respectively (Figure 24).

One patient example is shown in Figure 25. The patient was diagnosed with glioblastoma and underwent chemoradiation and surgery for tumor resection prior to this imaging session. A surgical cavity is present in the right anterior frontal lobe. A nodular enhancement area is present at the inferior lateral margin of the cavity, which was confirmed to represent recurrent tumor by MR spectroscopy. The recurrent tumor, the surgical cavity and the surrounding edema appear dark on pre-contrast T1w-MPRAGE, indicating long T1, in agreement with the Multitasking T1 map. The tumor and surgical cavity appear dark on T2w-FLAIR, indicating that such regions are occupied by fluid with less tissue structures and more unrestricted diffusion, confirmed by the clinical ADC map using DW-RSEPI. The surrounding edema shows higher ADC. The Multitasking ADC map is consistent with the clinical ADC map. The tumor, the surgical cavity and the edema appear bright on T2w-TSE, indicating long T2. Specifically, the fluid in the tumor and cavity shows even longer T2 compared to the edema.

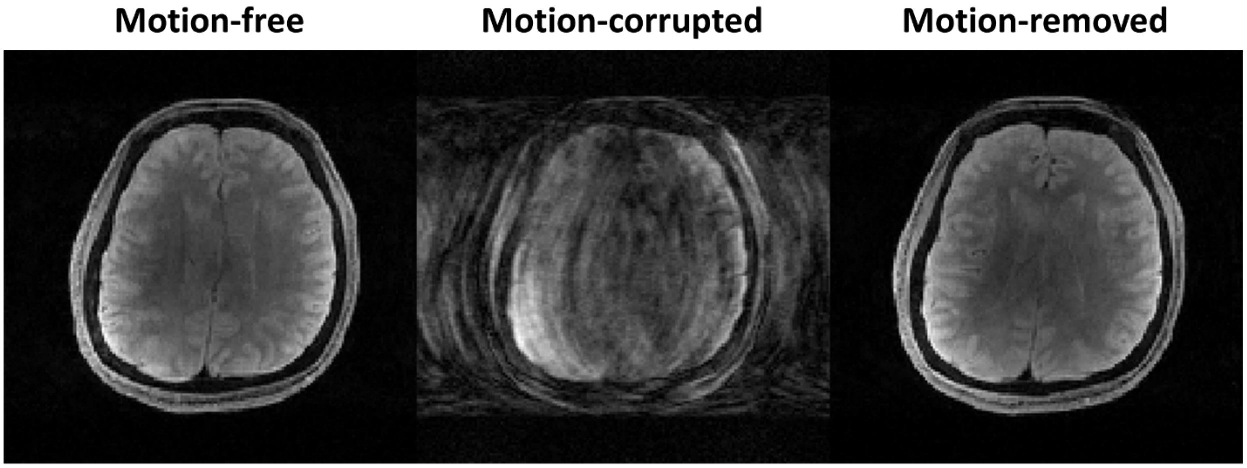

Figure 22. Example clean motion-free image with clear brain tissue, motion-corrupted image with blurring artifacts and significant signal loss, and clean motion-removed image with restored tissue structures corresponding to the sequence parameter combination $(\boldsymbol{n}, \boldsymbol{\tau}, \boldsymbol{b}, \boldsymbol{d}) = (\mathbf{50}, \mathbf{1}, \mathbf{1}, \mathbf{1})$.

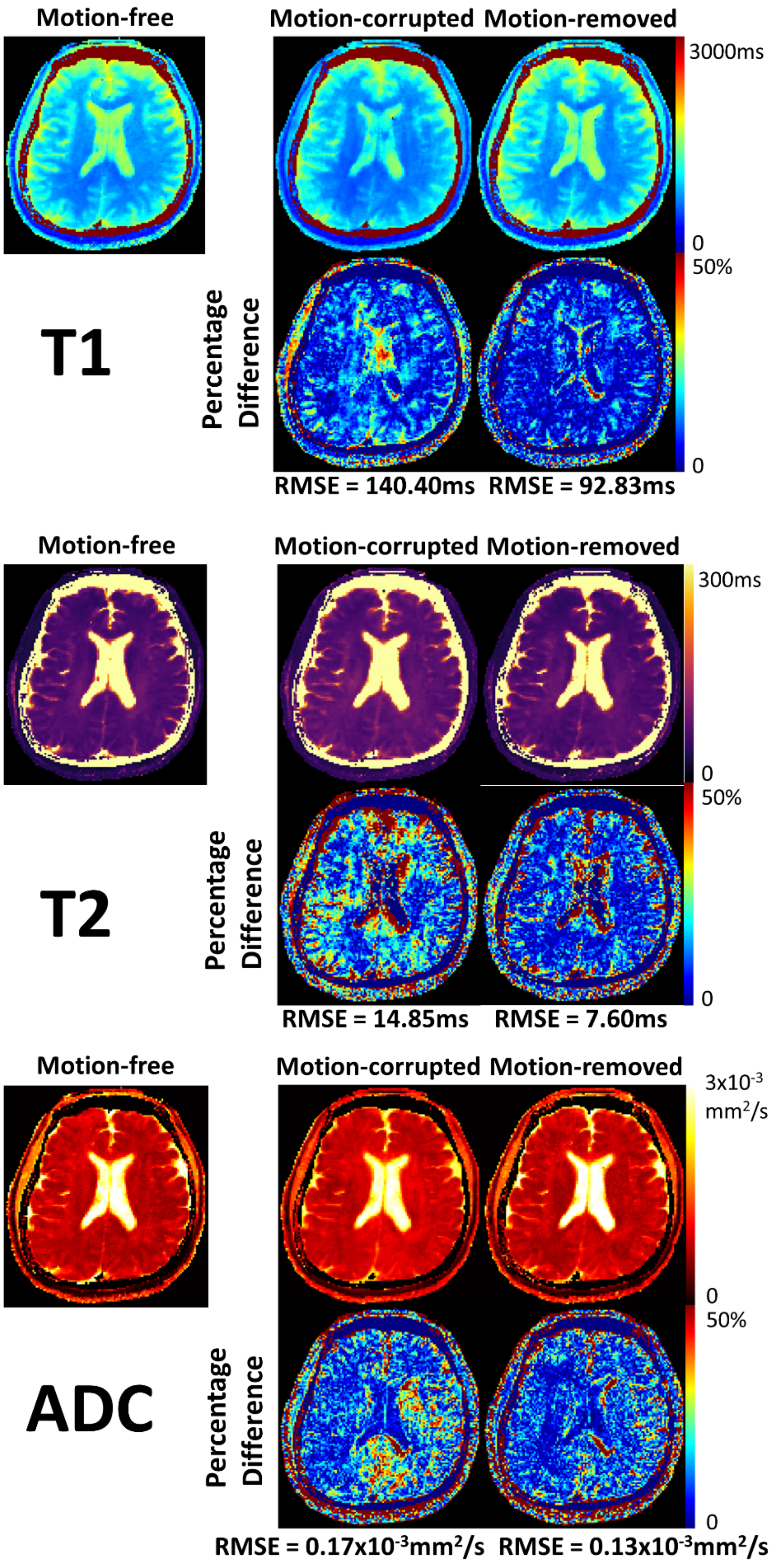

Figure 23. Motion effect exploration for subject 1, where 39% T2preps and 8% diffusion-preparations (20% data in total) are corrupted and removed. Comparison between motion-free, motion-corrupted, and motion-removed quantitative T1/T2/ADC maps, as well as the respective percentage difference maps against the motion-free reference are shown. The percentage difference map is generated by normalizing the absolute difference with the motion-free map. The motion results in substantial blurring artifacts in the T1 map, as well as elevated T2 and ADC values. After motion removal, the artifacts are removed and the biased T2 and ADC measurements are restored, resulting in lower root-mean-squared errors (RMSE) for all measurements.

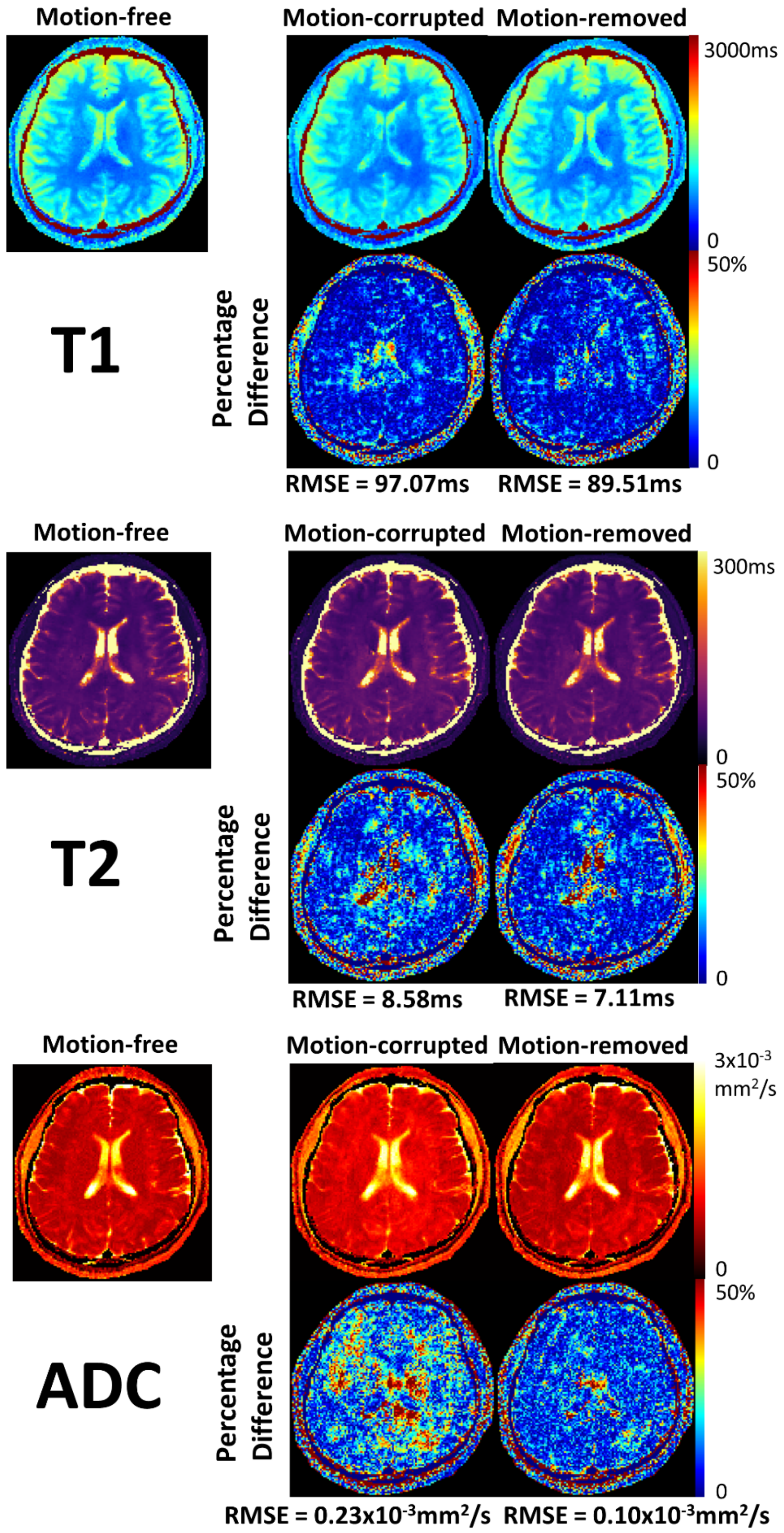

Figure 24. Motion effect exploration for subject 2, where 21% T2preps and 40% diffusion-preparations (33% data in total) are corrupted and removed. Comparison between motion-free, motion-corrupted, and motion-removed quantitative T1/T2/ADC maps, as well as the respective percentage difference maps against the motion-free reference are shown. The percentage difference map is generated by normalizing the absolute difference with the motion-free map. Motion-corrupted and motion-removed T1/T2 maps do not show much differences with the motion-free maps. ADC values are substantially elevated due to motion. After motion removal, most biased ADC measurements are restored, resulting in slightly reduced root-mean-squared errors (RMSE) for T1 and T2, as well as substantially reduced RMSE for ADC.

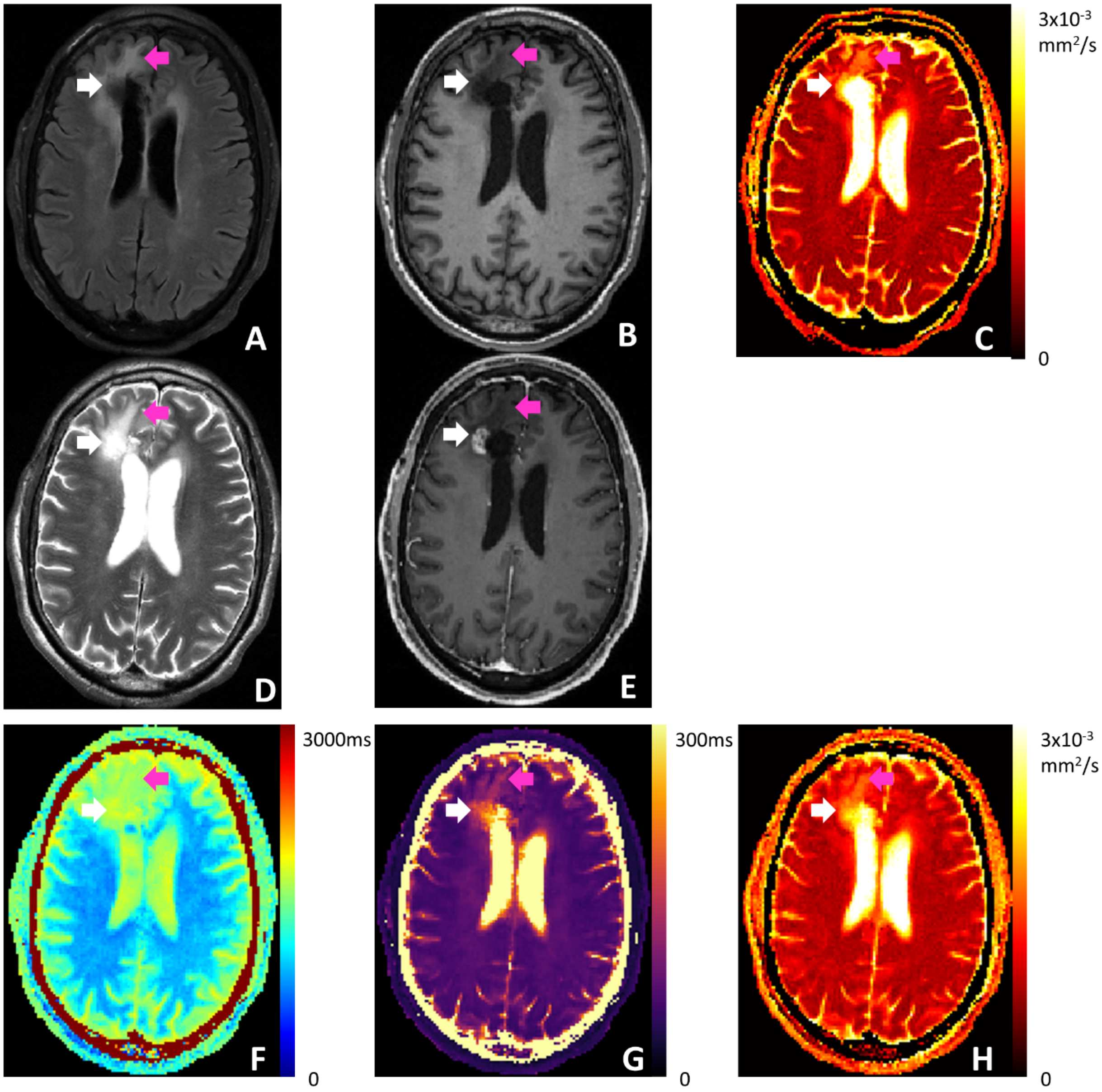

Figure 25. Clinical images and Multitasking T1/T2/ADC maps of a patient who was previously diagnosed with glioblastoma and underwent chemoradiation and surgery for tumor resection. (A) T2 FLAIR. (B) Pre-contrast T1 MPRAGE. (C) Clinical ADC map using RESOLVE. (D) T2 TSE. (E) Post-contrast T1 MPRAGE. (F-H) T1/T2/ADC maps obtained from Multitasking. White arrows point to the nodular enhancement area identified on post-contrast T1 MPRAGE. Purple arrows point to the surrounding edema. Multitasking T1/T2 maps reflect the tissue characteristics indicated by the clinical qualitative images. Multitasking ADC map is consistent with the clinical ADC map.

3.4 Discussion

We propose a novel approach to achieve 3D simultaneous brain T1/T2/ADC mapping by incorporating diffusion-preparation and phase correction into the MR Multitasking framework. This method enables full quantification of T1/T2/ADC in a single 9.3min scan for 100mm brain coverage. Phantom experiments and healthy volunteer experiments were performed for validation, showing substantial consistency and "excellent" agreement of T1/T2/ADC measurements between the proposed method and reference protocols by ICC. Multitasking produced co-registered T1/T2/ADC maps free from image distortion. Motion robustness was demonstrated via simple motion removal. Three post-surgery patients who were previously diagnosed with brain tumor and were likely to possess residual/recurrent tumor were scanned to demonstrate clinical feasibility. The Multitasking T1/T2/ADC maps were consistent with the clinical protocols and were able to reflect the tissue characteristics and contrasts indicated by the qualitative clinical images.

Since the emergence of MRF, simultaneous multi-parametric quantification has drawn substantial interest due to its great promise for clinical applications[28,30,36]. The Multitasking framework has several advantages over previous methods in simultaneous T1/T2/ADC mapping. We generate T1-T2-diffusion contrast using a concatenation of separate T2preps and diffusion-preparations, which because only the preparation modules are sensitive to physiological motion (as opposed to each readout), mitigating physiological motion sensitivity in comparison to DESS[84]. In addition, compared to MRF[85] and STEM[60], we achieve a comprehensive T1/T2/ADC quantification in three noncolinear diffusion directions, which matches the clinical DWI protocol. The proposed method achieves 100mm coverage (20 slices) in 9.3min, which outperforms DESS (32slices, 32mm coverage in 23min), Fingerprinting (1 slice in 60s) and STEM (2slices with 5mm thickness in 13min20s) in terms of acquisition efficiency. ZEBRA has higher acquisition efficiency (28slices with 2.6mm thickness in 2min42s) but it quantifies T2* rather than T2 and is limited to 2D acquisition[86]. Furthermore, we use a 3D segmented FLASH readout which produces co-registered quantitative maps free from image distortion, as compared to the SS-EPI readout employed in STEM and ZEBRA.

The proposed method yields consistent GM and WM T1/T2/ADC measurements with substantial agreement compared to the references, with all ICC in the range of 0.82 to 0.98, considered “excellent”. T1 and ADC were accurately measured with <5% bias. T2 is underestimated with <7% bias which is far less than the difference of T2 values between normal tissue and brain tumors (>50%)[26] and therefore should not affect differentiation in clinical studies. Possible sources of differences in measurements between Multitasking and the references are the difference in T1 signal evolution (i.e., the T1-decay model in Multitasking vs the inversion-recovery model in IR-TSE), insufficient removal of phase inconsistencies resulting in a reduced diffusion-weighted signal (and therefore ADC overestimation), and the effect of B1 inhomogeneities on T2-prep (incomplete refocusing or reduced tip-down/tip-up efficiency) that results in a reduced signal (and therefore T2 underestimation)[103].

The existence of shot-to-shot (inter-shot) phase variation[88,104-106] in diffusion-prepared MRI is well-known and has previously been addressed by approaches such as navigator-based phase estimation[104,107-109] and navigator-free phase correction[110-112]. Here, our time-resolved phase correction compensates for the inter-shot phase inconsistencies by performing model-based phase correction[87,88] at each timepoint. We observed that the diffusion-preparations may produce completely different phase patterns; T2-prep, however, consistently produce approximately the same phase pattern. As a result, the phase inconsistencies will lead to severe cancellation of signals mostly in diffusion-weighted signals, resulting in significantly increased ADC measurements if uncorrected. T1 and T2 are less affected because i) the T1 fitting is primarily dominated by the signal evolution following the shortest T2-prep, and ii) the signals encoded with different T2 weightings do not experience these phase inconsistencies.

Motion effects were explored by identifying corrupted shots on the preliminary real-time images and performing data removal. Advanced motion compensation approaches will be included in future work to make sure no re-acquisition is necessary in clinical settings. Compared to MRF studies where the quantitative mapping accuracy is affected by exactly *when* the motion occurs during the scan[67,68], our Multitasking framework appears less sensitive to the timing of motion. The sensitivity to the timing of motion can potentially be further reduced by interleaving the T2-prep and D-prep (i.e., one acquisition block contains 4 T2-prep and 6 D-prep, and the whole acquisition block repeats). For this evaluation, manual inspection identified motion-corrupted images, as the image artifacts and signal loss are significant. An automatic data removal algorithm may be included in future work, similar to a method which successfully identified the abnormal segments of data using the real-time temporal basis functions[72]. Here, Multitasking T1/T2/ADC mapping was robust to motion when up to 39% T2preps are corrupted or up to 40% diffusion-preparations are corrupted. The effectiveness of simple data removal indicates that even shorter scan times may be achievable by cutting down the number of repetitions for each preparation.

Separate ADC acquisition using SS-EPI showed higher SNR efficiency than the ADC from Multitasking; however, Multitasking has the additional benefit of producing distortion-free ADC maps which are co-registered with T1 and T2 maps, which could potentially benefit machine-learning-based radiomic algorithms to provide predictive biomarkers for diagnosis and prognosis[113,114]. In scenarios where ADC SNR efficiency is preferred, an alternative approach to achieve efficient T1/T2/ADC mapping could be simultaneous T1/T2 mapping with

Multitasking[69,115] followed by a separate fast, distorted DWI acquisition[116]. The best acquisition strategy remains an open question, and it can be for the clinicians to determine which strategy to adopt in a specific clinical practice.

In general, a major limitation of this simultaneous T1, T2, ADC mapping technique is the long reconstruction time which is primarily contributed from the inclusion of the time-resolved phase correction. Although the LRT image model reduces the memory and accelerates computation of the image tensor, it has no effect on the full-size time-resolved phase map because the phase function cannot be modeled as a partially separable spatiotemporal function. Successive generation of workstations and computational hardware improvements may also speed up the computation. Another limitation is the inherent low SNR determined by the sequence structure, where the crusher gradients remove half of the signal and lead to an exponential T1 decay signal course. For organs with deeper penetration distance from the receive coils such as prostate, other readouts (i.e., SSFP) or sequence structures (i.e., EPI) with higher SNR are also worth exploring.

3.5 Conclusion

We have proposed a novel MR Multitasking framework to achieve 3D simultaneous brain T1/T2/ADC mapping in <10min. The proposed method provides co-registered images without distortion, quantifies T1/T2/ADC measurements with substantial agreement with reference protocols, and demonstrates clinical feasibility. Extending this work to leverage the established ability of the Multitasking framework to obtain motion-resolved quantitative mapping is a potential avenue to achieve simultaneous T1/T2/ADC mapping of the abdomen and heart.

Chapter IV Motion-Resolved, 3D Whole-Brain Simultaneous T1, T2, and T1ρ Quantification with MR Multitasking: Method and Initial Clinical Experience

4.1 Introduction

MRI relaxometry reveals biological tissue properties by characterizing the excited spin dynamics in the presence of external magnetic fields. For example, quantifying T1/T2 in the brain is clinically promising for tissue characterization, early detection, staging, and treatment monitoring of various brain tumors[26-28,80] and neurologic pathologies such as MS[117-121], Alzheimer's disease[122-124], Parkinson's disease[125-127], and more. T1ρ is an emerging relaxometry mechanism described as the spin-lattice relaxation in the rotating frame, which measures the decay of the transverse magnetization in the presence of an external "spin-locking" B1 field, and is most commonly used in articular cartilage imaging so far, showing promise for early detection of subtle cartilage matrix degeneration of osteoarthritis patients due to its high sensitivity to the collagen-proteoglycan matrix damage[128-131]. A few studies have also explored the value of T1ρ in pathological activities of degenerative neurologic diseases and provided useful image biomarkers for the evaluation and early diagnosis of Alzheimer's disease[132,133], Parkinson's disease[134,135], stroke[136], and MS[35,137].

Despite the great potential of quantitative MR relaxometry to allow comprehensive evaluation of tissue states, multiparametric mapping of T1/T2/T1ρ is time-consuming and may be impractical in clinical settings. This is especially true for T1ρ imaging, which can be slow and inefficient due to the necessary delay time for magnetization restoration, the multiple spin-lock times, and the multiple spin-lock frequencies required. Moreover, if measured in separate acquisitions, these parameter maps may be subject to misalignment due to patient movement. Consequently, efficient and simultaneous quantification of multiple relaxation parameters is highly desirable for clinical practice.

Motion is one of the most challenging issue in clinical brain MR exams especially for the elderly or those with specific types of diseases (i.e., Parkinson's disease). Nearly 30% inpatient MR scans suffered from motion artifacts[138]. Intra-scan motion causes ghosting artifacts that may lead to a loss of valuable diagnostic information, while inter-scan motion produces misaligned images that poses difficulty for clinical interpretation. The most common strategy to deal with motion is reacquisition but it greatly lengthens the scan time, costing approximately $115,000 per scanner per year for hospitals[138]. Other approaches to handling motion include navigator- and image-based motion tracking[139-141], prospective motion correction[139,142], and retrospective motion correction[139,143]. However, despite all these efforts, it seems to note that there doesn't exist a single method generalizable enough to tackle all the motion issues, but rather a toolbox of partial solutions depending on specific imaging experiments and motion types[144]. As a novel imaging framework, MR Multitasking handles motion in various ways, allowing either motion-resolved imaging by modeling motion as an extra dimension and leveraging the correlation between motion states[69,70] or motion-removed imaging by motion detection and rejection of motion-corrupted data[71,72].

In this work, we demonstrate simultaneous quantification of T1/T2/T1ρ with whole-brain coverage in 9 minutes, which is accomplished by extending the original Multitasking framework to also incorporate novel hybrid T1ρ-preparation/inversion recovery (T1ρ-IR) pulses. Our framework conceptualizes the multiple relaxation processes (e.g., T1, T2, and T1ρ) as multiple time dimensions to establish a multidimensional image tensor. We design motion experiments to demonstrate the effectiveness of the proposed imaging framework under both in-plane "shaking" motion and through-plan "nodding" motion. In addition to mapping, we also demonstrate the feasibility of generating six synthetic contrast-weightings from the T1/T2/T1ρ maps. Repeatability of quantitative measurements and the agreement with reference approaches are evaluated on a phantom and in healthy controls. Clinical validation is performed on a relapsing-remitting MS (RRMS) patient cohort, hypothesizing that each relaxometry mapping offers complementary tissue information and the integration of three parameters allows better detection and assessment of the degenerative pathologic progression in multiple sclerosis.

4.2 Methods

4.2.1 Pulse Sequence Design

Our pulse sequence generates T1/T2/T1ρ contrasts by cycling through several B0- and B1-insensitive hybrid T2-preparation/inversion recovery (T2-IR) pulses with different durations τ and several B0- and B1-insensitive T1ρ-IR pulses with different spin-lock times τ_{SL}. This structure builds upon our previously developed Multitasking pulse sequences[69] by introducing novel T1ρ-IR pulses. The T2-IR pulse is modified from an adiabatic T2-prep module with 180° BIREF1 refocusing pulses in an MLEV phase pair scheme[145], replacing the 90° tip-up pulse by a 90° tip-down pulse after refocusing to achieve the inversion effect[146]. The T1ρ-IR pulse follows a similar scheme: it is modified from a paired self-compensated adiabatic T1ρ-preparation module[147], also replacing the 90° tip-up pulse by a 90° tip-down pulse after refocusing to achieve the inversion effect. 3D FLASH excitations fill the entire recovery period between preparation pulses for data readouts. Detailed illustration of the pulse sequence and signal evolution is shown in Figure 26A-26C.

4.2.2 k-Space Sampling

The entire k-space data collection can be divided into two sets (Figure 26D). Firstly, imaging data ($\mathbf{d}_{\text{img}}$) are collected with a 3D Gaussian-density random Cartesian trajectory along both phase-encoding ($\mathbf{k}_y$) and partition-encoding ($\mathbf{k}_z$) directions. Secondly, subspace training data ($\mathbf{d}_{\text{tr}}$) are periodically embedded into the imaging data collection at the k-space center location (i.e., $\mathbf{k}_y = \mathbf{k}_z = 0$) every 8 readouts. The subspace training data will serve dual purposes: i) for motion

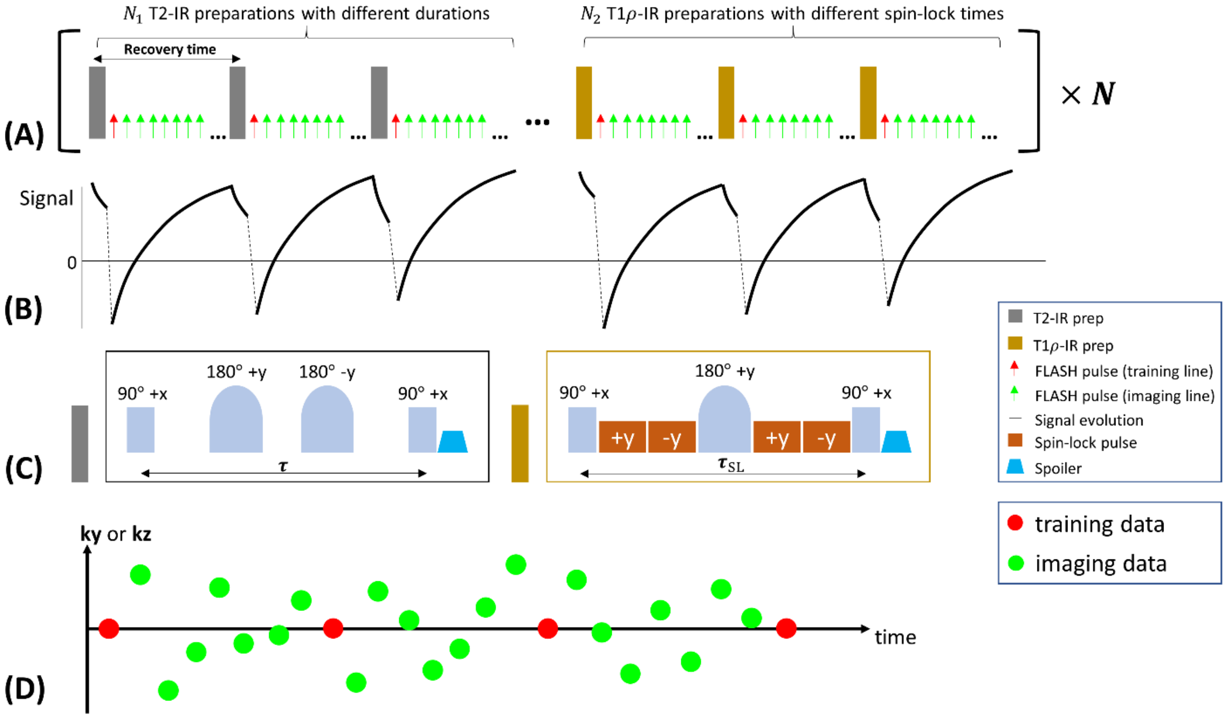

Figure 26. (A) General sequence structure with interleaved T2-IR pulses and T1ρ-IR pulses. 3D FLASH readouts fill the entire recovery period. (B) Demonstration of signal evolution. The signal follows an exponential decay during the preparations and follows a look-locker inversion recovery during FLASH readouts. (C) Construction of T2-IR preparation pulses and T1ρ-IR preparation pulses, where T2-IR uses BIREF adiabatic refocusing pulses in an MLEV phase pair scheme and T1ρ-IR uses a paired self-compensated scheme. (D) K-space sampling demonstration. Imaging data are sampled from the entire k-space with Gaussian density. Training data periodically samples the center k-space line every 8 readouts.

identification clustering, and ii) for estimating the temporal basis functions of motion and other image contrasts dimensions that will be used in the LRT image model.

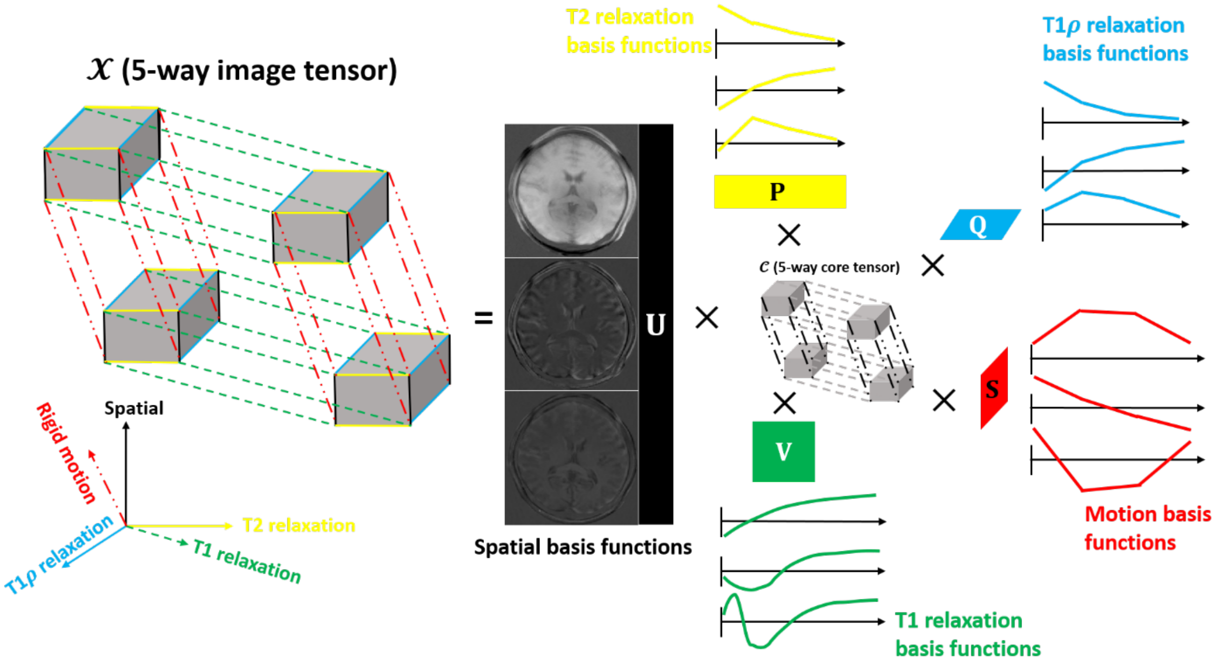

Figure 27. Illustration of multiple temporal dimensions of the 5-way low-rank tensor for simultaneous T1, T2, and T1ρ mapping in the brain. The 5-way image tensor contains spatial, T1 relaxation, T2 relaxation, T1ρ relaxation and rigid motion dimensions. The low-rank tensor structure can be explicitly expressed through tensor factorization between 5 sets of basis functions assigned to each dimension and the 5-way core tensor governing the interaction between different basis functions. Here only the three most significant basis functions describing each dimension of the tensor are provided.

4.2.3 Image Model

We model the underlying image sequence as a 7-dimensional function $x(\mathbf{r}, n, \tau, \tau_{\mathrm{SL}}, s)$ with $\mathbf{r} = [x, y, z]$ indexing three spatial dimensions, while n, τ, τ_{SL}, and s index four time dimensions characterizing the dynamic processes of T1 recovery, T2 decay, T1ρ decay, and bulk motion respectively. The image function x can be further represented in discretized form as a 5-way tensor $\mathcal{X}$ with elements $X_{ijkl} = x(r_i, n_j, \tau_k, \tau_{\mathrm{SL},l}, s_m)$, which can be explicitly expressed as:

$$\mathbf{X}_{(1)} = \mathbf{U}\boldsymbol{\Phi}, \tag{4.1}$$

$$\boldsymbol{\Phi} = \mathbf{C}_{(1)}(\mathbf{S} \otimes \mathbf{Q} \otimes \mathbf{P} \otimes \mathbf{V})^T, \tag{4.2}$$

where the factor matrix $\mathbf{U}$ contains spatial basis functions, the factor matrices $\mathbf{V}$, $\mathbf{P}$, $\mathbf{Q}$, $\mathbf{S}$ contain temporal basis functions spanning the four temporal subspaces corresponding to T1, T2, T1ρ, and bulk motion, and the rows of $\boldsymbol{\Phi}$ span the multidimensional temporal subspace. An illustration of different time dimensions is shown in Figure 27.

4.2.4 Image Reconstruction

MR Multitasking allows accelerated imaging as well as rapid and memory-efficient reconstruction by serially recover the tensor factor matrices composing $\mathcal{X}$. A schematic flowchart is shown in Figure 28. Specifically, this can be achieved in four stages:

Figure 28. Schematic diagram of the Multitasking image reconstruction. Example 3DNAV image series are shown, which contain mixed dynamic processes of T1 recovery, T2/T1ρ decay, and motion. The last frame of each recovery period is picked out to construct the series $\mathbf{X}_s$ which will be used for motion state clustering. Example motion weightings, training data residuals and motion states assignments are shown. High residuals (low motion weightings) correspond to the transition between different motion states, which tackles the misidentified or outlier motion.

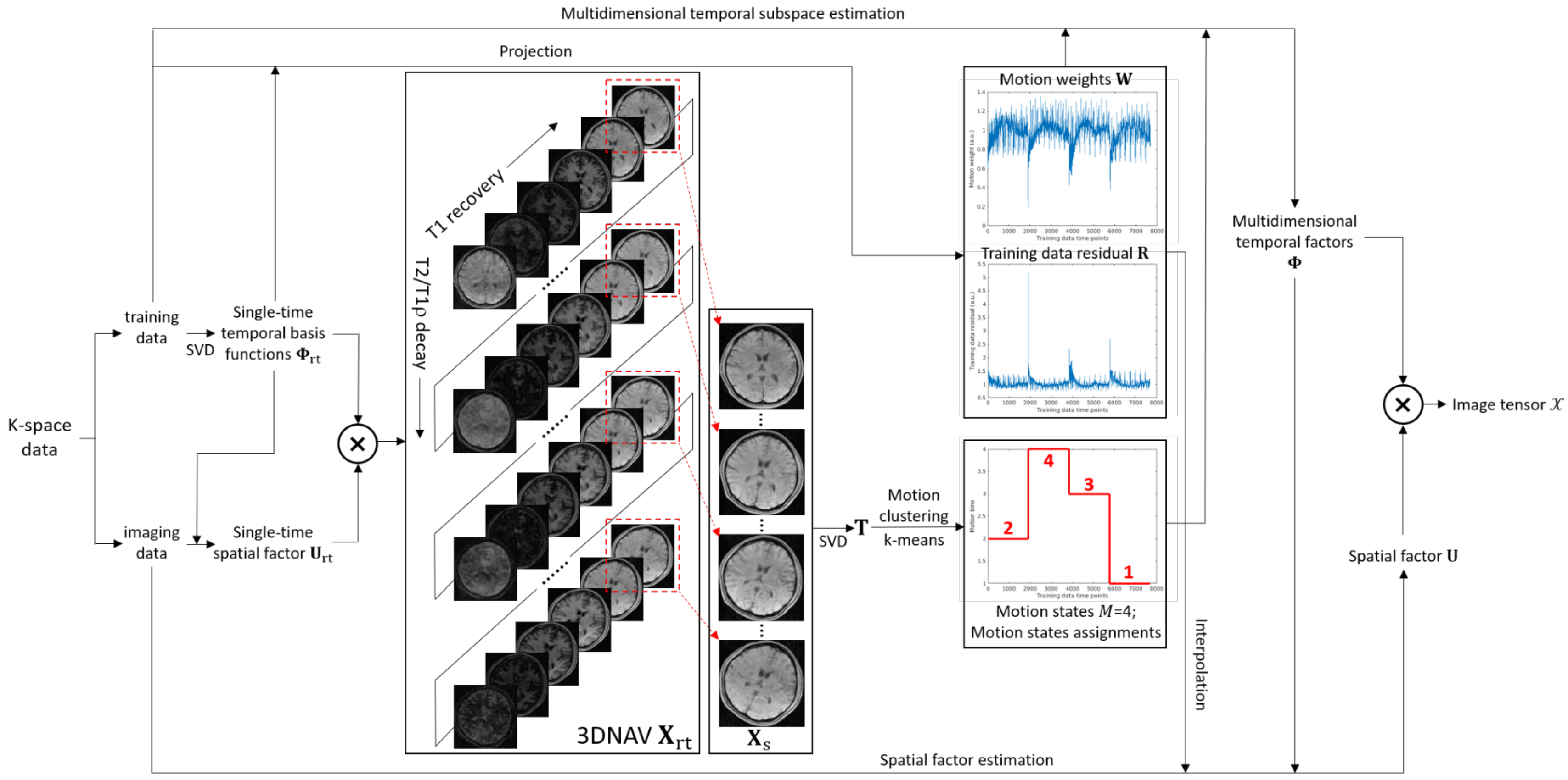

4.2.4.1 Single-time 3D navigator (3DNAV) Reconstruction

Considering the situation where $\mathcal{X}$ is a matrix with only two dimensions: one spatial dimension and one elapsed, single time dimension t indexing the total sampled time points with a mixture of all the image dynamics (i.e., T1, T2, T1ρ, and motion), the LRT model described in Eqs. (4.1)-(4.2) is reduced to a simplified matrix factorization form

$$\mathbf{X}_{\mathrm{rt}} = \mathbf{U}_{\mathrm{rt}}\mathbf{\Phi}_{\mathrm{rt}}, \tag{4.3}$$

where $\mathbf{\Phi}_{\mathrm{rt}}$ contains the temporal basis functions for the single-time dimension, and $\mathbf{U}_{\mathrm{rt}}$ is the single-time spatial factor matrix. $\mathbf{X}_{\mathrm{rt}}$ will be used as a 3DNAV for rigid motion clustering, and can be reconstructed in a two-step process: i) extract $\mathbf{\Phi}_{\mathrm{rt}}$ via the singular value decomposition (SVD) of $\mathbf{d}_{\mathrm{tr}}$, and ii) recover $\mathbf{U}_{\mathrm{rt}}$ by fitting $\mathbf{\Phi}_{\mathrm{rt}}$ to the imaging data:

$$\mathbf{U}_{\mathrm{rt}} = \arg\min_{\mathbf{U}_{\mathrm{rt}}}\left\|\mathbf{d}_{\mathrm{img}} - \Omega(\mathbf{F}\mathbf{S}\mathbf{U}_{\mathrm{rt}}\mathbf{\Phi}_{\mathrm{rt}})\right\|^2, \tag{4.4}$$

where $\Omega(\cdot)$ is the undersampling operator, $\mathbf{F}$ applies spatial encoding, and $\mathbf{S}$ applies multichannel encoding.

4.2.4.2 Rigid Motion State Clustering

A subset of $\mathbf{X}_{\mathrm{rt}}$, denoted as $\mathbf{X}_{\mathrm{s}}$, corresponding to the last time point of each recovery period will be used to identify motion and cluster motion states, assuming that all the images within the same recovery period belong to the same motion state which can be represented by the motion state of the last time point of this recovery period. $\mathbf{X}_{\mathrm{s}}$ is chosen to minimize the effect of the changing image contrast (i.e., T1 recovery, T2 decay, T1ρ decay) on the subsequent motion clustering, as the signals approach to the FLASH steady state immediately before the next preparation pulse is played. Image features $\mathbf{T} = (\mathbf{t}_1, \mathbf{t}_2, \dots, \mathbf{t}_{N_s})$ are extracted from $\mathbf{X}_{\mathrm{s}}$ via SVD, where N_s denotes the number of recovery periods, and a k-means algorithm will be performed on

$\mathbf{T}$ for motion state clustering. To select the number of motion states/clusters K, the algorithm is performed for K=1,2,…,10, and for each K we calculate the total Euclidean distance to the centroids:

$$d_K = \sum_{k=1}^{K} \sum_{\mathbf{t}_s \in C_k} \|\mathbf{t}_l - \mathbf{c}_k\|^2, l \in \{1,2,\dots,N_s\}, \tag{4.5}$$

where $\mathbf{c}_k$ is the centroid of the kth cluster C_k. We choose the final K at the elbow of the (K, d_k) plot.

4.2.4.3 Multidimensional Tensor Subspace Estimation

In this stage, we propose to estimate the factor matrices $\mathbf{V}$, $\mathbf{P}$, $\mathbf{Q}$, $\mathbf{S}$ as well as the unfolded core tensor $\mathbf{C}_{(1)}$. This can be achieved in a two-step process:

1) Predetermine the temporal factor matrix $\mathbf{V}$ for the T1 relaxation dimension. We generate a training dictionary of physically feasible IR-FLASH signal curves governed by the Bloch equations, with a range of feasible T1 values and B1 inhomogeneities, as demonstrated in our previous work[69]. Specifically, we use 101 T1 values logarithmically spaced between 100ms and 4000ms, 15 FLASH flip angles equally spaced between 0.5° to 7.5°, and 21 efficiency factors controlling the B1 inhomogeneities of the preparation pulses and the incomplete approach to the FLASH steady state, equally spaced between -1 to -0.5. Therefore, the dictionary comprises 31815 feasible signal curves. The T1 relaxation basis functions in $\mathbf{V}$ are estimated from the SVD of this training dictionary. Basis functions for the T2 and T1ρ relaxation dimensions are not predetermined due to the complexity of modeling B0 inhomogeneities and will instead be calculated from the training data in the second step.

2) Determine $\mathbf{P}$, $\mathbf{Q}$, $\mathbf{S}$, $\mathbf{C}_{(1)}$, and the multidimensional factor matrix $\mathbf{\Phi}$. With the identified motion states, $\mathbf{d}_{\mathrm{tr}}$ can be reshaped into a small scale training tensor $\mathcal{D}_{\mathrm{tr}}$ in the $(\mathbf{k}, n, \tau, \tau_{\mathrm{SL}}, s)$-

space, where $\mathbf{k}$ indexes the k-space location. This training tensor can be further completed via a Bloch-constrained small-scale LRT completion problem:

$$\hat{\mathcal{D}}_{\text{tr}} = \arg\min_{\mathbf{D}_{\text{tr},(2)}\in\text{range}(\mathbf{V})} \|\mathbf{W}[\mathbf{d}_{\text{tr}} - \Omega_{\text{tr}}(\mathcal{D}_{\text{tr}})]\|^2 + \lambda \sum_{i=1,3,4} \left\|\mathbf{D}_{\text{tr},(i)}\right\|_* + R(\mathcal{D}_{\text{tr}}), \tag{4.6}$$

where $R(\cdot)$ applies total variation (TV) regularization along the motion dimension, and $\mathbf{W}$ is a diagonal weighting matrix that reweights each auxiliary k-space line to reduce the effect of misidentified or outlier motion from the transient motion states. Here $\mathbf{W}$ is calculated from the single-time auxiliary data residual $\mathbf{R}$:

$$\mathbf{R} = \mathbf{d}_{\text{tr}} - \mathbf{d}_{\text{tr}}\mathbf{\Phi}_{\text{rt}}^{\dagger}\mathbf{\Phi}_{\text{rt}}, \tag{4.7}$$

and

$$W_{jj} = \left(\sum_{i=1}^{N_v \times N_c} \left|R_{ij}\right|^2\right)^{-1/2}, \tag{4.8}$$

where N_v, N_c represent the number of voxels and coils. The core tensor $\mathbf{C}_{(1)}$ and the remaining temporal factor matrices can be quickly extract from the completed $\hat{\mathcal{D}}_{\text{tr}}$ via HOSVD[78], yielding $\mathbf{\Phi} = \mathbf{C}_{(1)}(\mathbf{S} \otimes \mathbf{Q} \otimes \mathbf{P} \otimes \mathbf{V})^T$.

4.2.4.4 Spatial Factor Estimation

The final stage estimates the spatial factor matrix $\mathbf{U}$ by fitting the multidimensional temporal factor matrix $\mathbf{\Phi}$ to the imaging data, with a similar motion-weighting scheme:

$$\hat{\mathbf{U}} = \arg\min_{\mathbf{U}} \left\|\mathbf{W}_{\text{interp}}[\mathbf{d}_{\text{img}} - \Omega(\mathbf{FSU\Phi})]\right\|^2 + R_s(\mathbf{U}), \tag{4.9}$$

where $R_s(\cdot)$ applies spatial TV regularization that leverages compressed sensing, and $\mathbf{W}_{\mathrm{interp}}$ is the diagonal motion-weighting matrix linearly interpolated from $\mathbf{W}$, which reweights each imaging readouts to also tackle the misidentified or outlier motion.

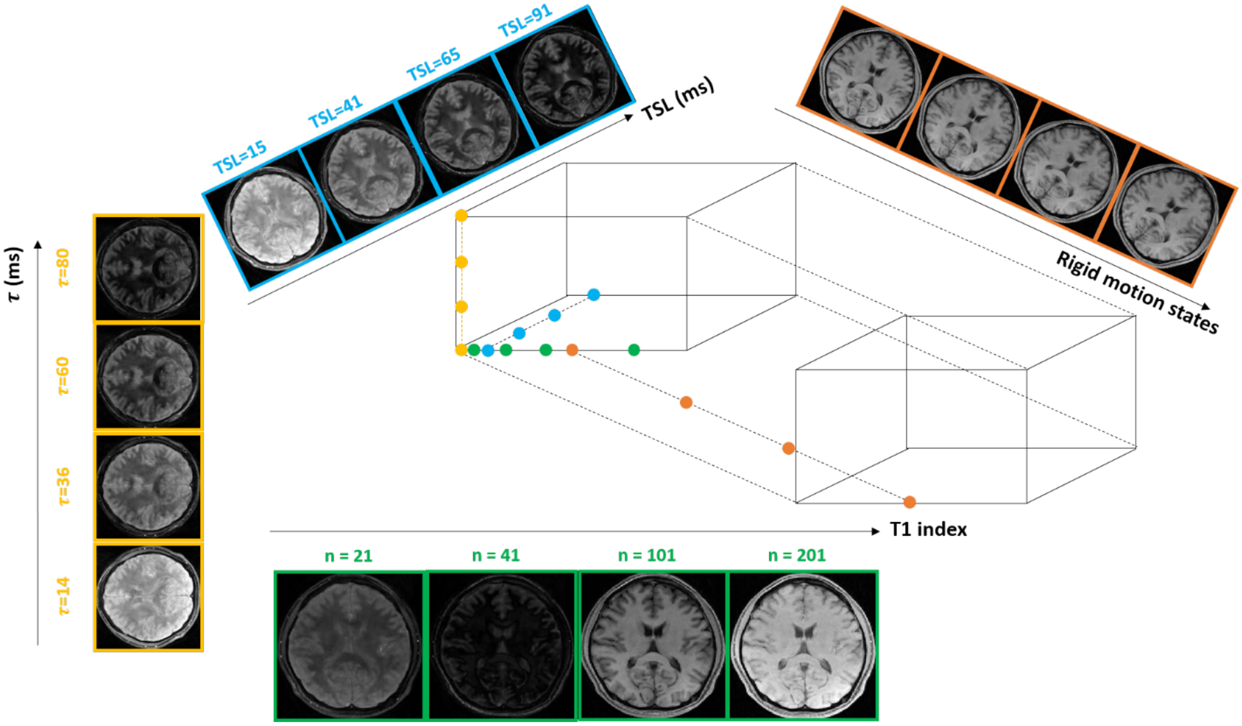

Figure 29. Demonstration of the multidimensional tensor formulation for simultaneous T1, T2, and T1ρ mapping in the brain. Green color represents different T1 weightings. Yellow color represents different T2 weightings. Blue color represents different T1ρ weightings. Orange color represents different rigid motion states. Solid dots represent the locations of the displayed images in the tensor.

The reconstructed image tensor is thus expressed as $\widehat{\mathbf{X}}_{(1)} = \widehat{\mathbf{U}}\mathbf{\Phi}$ in the unfolded matrix form, which can be further reshaped back into a 5-way tensor $\widehat{\mathcal{X}}$ that can individually show the process of T1 recovery, T2 decay, T1ρ decay, and different motion states along the respective time dimensions. An illustration of the multidimensional image tensor is shown in Figure 29.

4.2.5 Multiparametric Mapping

After reconstructing the image tensor, voxel-wise multiparametric mapping can be performed following the signal equation:

$$S_n = A \cdot \frac{1-e^{-\frac{TR}{T1}}}{1-e^{-\frac{TR}{T1}}\cos(\alpha)}[1 + \left(Be^{-\frac{\tau}{T2}}e^{-\frac{\tau_{\mathrm{SL}}}{\mathrm{T1}\rho}} - 1\right)\left(e^{-\frac{TR}{T1}}\cos(\alpha)\right)^n]\sin(\alpha), \tag{4.10}$$

where A absorbs proton density, overall B1 receive field, and T2$*$ weighting, n is the readout index counting from 1 to the number of readouts per preparation pulse, α denotes the FLASH flip angle, and B represents the efficiency factor controlling the mixed effect of the B1 transmit inhomogeneity for the preparation pulse and the incomplete approach to the FLASH steady state.

4.2.6 Imaging Experiments

All imaging experiments were conducted on a 3T clinical scanner (Biograph mMR, Siemens Healthineers, Erlangen, Germany) using a 20-channel head coil.

4.2.6.1 Phantom study

An ISMRM/NIST phantom (model 130, High Precision Devices, Boulder, Colorado) was scanned. Reference protocols for phantom study included IR-SE for T1 mapping, SE for T2 mapping, and 3D T1ρ-prepared FLASH (T1ρ-FLASH) for T1ρ mapping. Scan parameters for Multitasking were: FOV=240x240mm^2, in-plane resolution=1.0x1.0mm^2, slice thickness=3.5mm. The detailed imaging protocol is in Table 8.

Table 8. Phantom imaging protocols and scan parameters for simultaneous T1/T2/T1ρ mapping.

Phantom Study	
Imaging Protocol	**Scan Parameters**
IR-SE (140min)	FOV=210x210mm^2, in-plane resolution=1.6x1.6mm^2, slice thickness=5mm, TIs=[21,100,200,400,800,1600,3200]ms
T2-SE (140min)	FOV=210x210mm^2, in-plane resolution=1.6x1.6mm^2, slice thickness=5mm, TEs=[12,22,42,62,102,152,202]ms
T1ρ-FLASH (3min)	FOV=240x240mm^2, in-plane resolution=1.0x1.0mm^2, slice thickness=3.5mm, TSLs=[15,23,31,51,91,131,171]ms, spin-lock frequency=500Hz
Multitasking (5.5min)	FOV=240x240mm^2, in-plane resolution=1.0x1.0mm^2, slice thickness=3.5mm, τ=[15,40,65,90,115,140,165]ms, τ_{SL}=[15,23,31,51,91,131,171]ms, spin-lock frequency=500Hz, FLASH TR/TE=9.4/4.9ms, flip angle=5°

4.2.6.2 In vivo study

Healthy control and patient studies were approved by the IRB of Cedars-Sinai Medical Center. All subjects gave written informed consent before MRI. *N*=15 age-matched healthy volunteers (6 male, 9 female, age 44.7±15.1) without any brain diseases were recruited. Reference protocols included IR-TSE for T1 mapping, ME-SE for T2 mapping, and 3D T1ρ-FLASH for T1ρ mapping, with a total scan time of 25min. The whole-brain Multitasking sequence was applied twice to test the scan-rescan repeatability, with a scan time of 9min per scan. All scans used FOV=240 mm x 240 mm, in-plane resolution=1.0 mm x 1.0 mm, slice thickness=3.5 mm. The detailed imaging protocol is in Table 10. In addition, N=8 RRMS patients (1 male, 7 females, age 46.8±8.0, disease duration 11.5±7.9 years) who were referred by an MS specialist were enrolled for clinical validation. The Multitasking sequence was incorporated in a clinical MRI study and was run before any contrast agent administered as part of the clinical protocol. The detailed imaging protocol is in Table 9.

Table 9. In vivo imaging protocols and scan parameters for simultaneous $T1/T2/T1\rho$ mapping.

In vivo Study	
Imaging Protocol	**Scan Parameters**
IR-TSE (12min)	FOV=240x240mm^2, in-plane resolution=1.0x1.0mm^2, slice thickness=3.5mm, TIs=[50,200,350,500,1000,1500,2400,3000]ms, GRAPPA factor=2
ME-SE (5min)	FOV=240x240mm^2, in-plane resolution=1.0x1.0mm^2, slice thickness=3.5mm, TEs=[14,28,42,56,70,84]ms, GRAPPA factor=2
$T1\rho$-FLASH (8min)	FOV=240x240mm^2, in-plane resolution=1.0x1.5mm^2, slice thickness=3.5mm, TSLs=[15,41,65,91]ms, spin-lock frequency=500Hz, 2 shots, GRAPPA factor=2
Multitasking (9min)	FOV=240x240mm^2, in-plane resolution=1.0x1.0mm^2, slice thickness=3.5mm, τ=[14,36,60,80]ms, τ_{SL}=[15,41,65,91]ms, spin-lock frequency=500Hz, FLASH TR/TE=9.4/4.9ms, flip angle=5°

4.2.7 Motion Experiments Design

Motion experiments were performed on one volunteer among the 15. First, a motion-free Multitasking scan was performed as a reference. Two rigid motion patterns were investigated – in-plane "shaking" motion that happens in the transverse plane, and through-plane "nodding" motion than happens along the longitudinal direction. Both types may involve translational and rotational head movement. Four Multitasking sessions with motion were implemented: 1) in-plane motion performed once at half of the scan (4.5min, Figure 30A); 2) in-plane motion performed three times at a quarter (2.25min), half (4.5min), and three quarters (6.75min) of the scan (Figure 30B); 3) through-plane motion performed once at half of the scan (4.5min, Figure 30C); 4) through-plane motion performed three times at a quarter (2.25min), half (4.5min), and three quarters (6.75min) of the scan (Figure 30D). Instructions to move were given during the scans. For each motion pattern, once hearing the instruction, the volunteer moved straightly from one position (i.e., motion state) to another position (i.e., motion state) without coming back, and the transition time was determined by the volunteer but should be less than 10s (~4 recovery periods), mimicking the real case in clinical scans when patients feel uncomfortable and want to adjust their position. The volunteer could choose to move either direction (i.e., left or right, up or down) depending on the motion pattern, but each motion should be restricted to an angle $< 30°$ also mimicking the real clinical case, which was achieved by placing stickers inside the head coil indicating the furthest position (nose aligning to the sticker) to reach. After each session, the volunteer was instructed to return to the initial position. The volunteer was trained to perform all types of motion before the scan started.

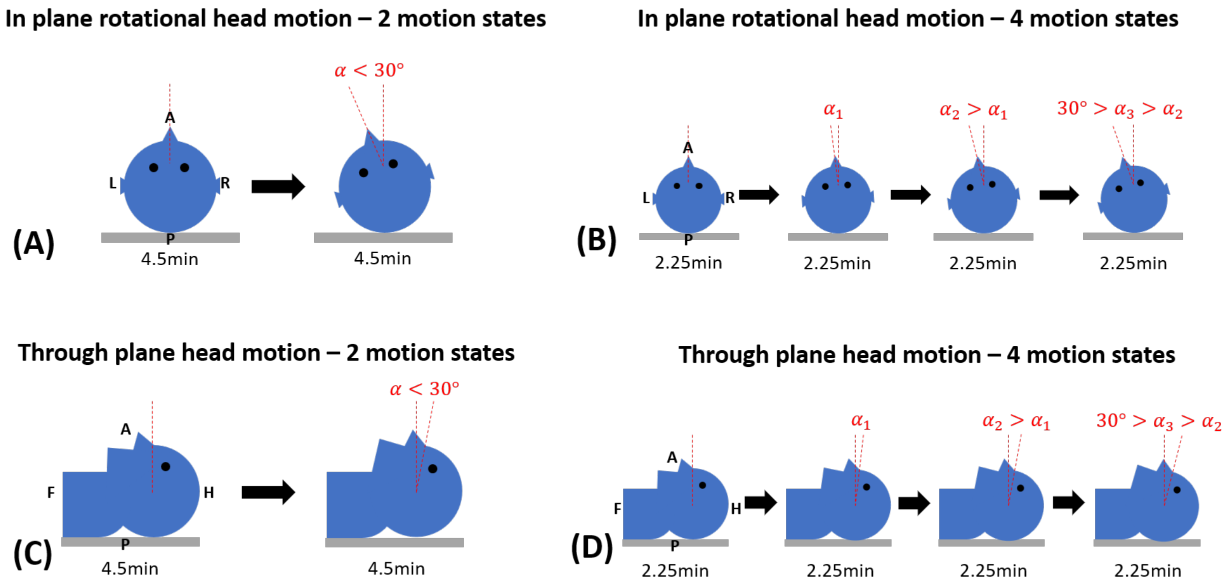

Figure 30. Illustration of the motion patterns for the four different motion experiments.

4.2.8 Image Analysis

All Multitasking image reconstructions were performed on a Linux workstation with a 2.70GHz dual 12-core Intel Xeon processor equipped with 256GB RAM and running MATLAB 2016b (MathWorks, Natick, Massachusetts). The reconstruction time was 0.8–1.5h for each subject. The penalty factor λ for weighting the nuclear norm in the tensor completion step was chosen based on the discrepancy principle[97]. The convex optimizations Eqs. (4.4) and (4.9) were solved via the alternating direction method of multipliers (ADMM) algorithm[148]. The ranks for the spatial dimension and for the T1 relaxation dimension were determined from the –40dB threshold of the normalized singular value curves obtained from the SVD of the completed subspace training data and the training dictionary, respectively. The ranks for the T2 relaxation, T1ρ relaxation, and motion dimensions were not truncated, as these dimensions were already penalized by the nuclear norm constraint in Eq. (4.6).

Voxel-wise quantitative T1/T2/T1ρ maps for all phantom and in vivo cases were obtained by fitting the reconstructed image tensor with Eq. (4.10). For all in vivo studies, image segmentation was performed by manual thresholding of the corresponding reference or Multitasking images. Example regions of interest are shown in Figure 31. Six synthetic qualitative contrast-weighted images were generated using the quantitative maps, where five of them are clinically adopted contrasts including T1w MPRAGE, T2w, proton-density-weighted (PDw), T2w-FLAIR, and double-inversion-recovery (DIR). We also synthesize a novel contrast, T1ρw-FLAIR, which is created by substituting T2 with T1ρ in the standard FLAIR signal model.

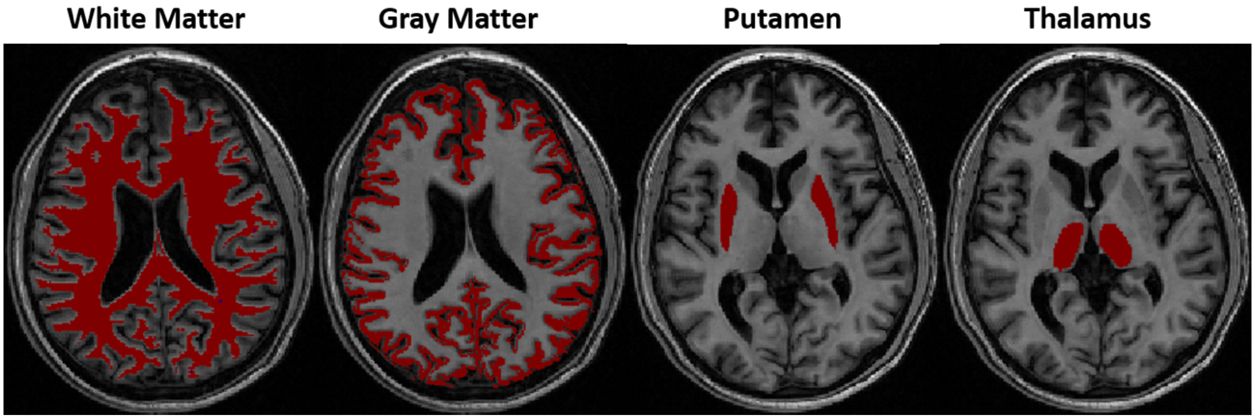

Figure 31. Demonstration of the example thresholding-based four regions of interest.

For each motion session, three comparisons with the reference were made: i) motion-resolved (where the motion state closest to the reference state was picked out); ii) motion-corrupted (where K=1); iii) we retrospectively truncated the k-space data that belonged only to a single motion state at the beginning of the reconstruction, which was feasible with known motion timing, and therefore used K=1 for the following reconstruction (i.e., we used half of the k-space data for the two sessions where the volunteer moved once, and used a quarter of the k-space data for the two sessions where the volunteer moved three times).

4.2.9 Quantitative Analysis

For the phantom study, T1/T2/T1ρ values for each vial were calculated. Linear regression analysis was performed, and ICCs were calculated using IBM SPSS Statistics (Armonk, New York) with a two-way mixed model and 95% confidence level to evaluate the quantitative agreement between Multitasking and the reference.

For the healthy control study, measurement populations of T1/T2/T1ρ for WM, GM, putamen, and thalamus were compared between Multitasking and the references. ICCs between Multitasking and the reference measurements were derived the same way as in the phantom study. Paired t-tests were performed to evaluate the significance between Multitasking and the reference measurements for each parameter in each tissue compartment. The significance level was set as p=0.05. Scan-rescan repeatability was evaluated from the Bland-Altman and ICC analyses of the 1st and 2nd Multitasking scans.

For each comparison in the motion investigation, we evaluated the structural similarity index (SSIM) and mean absolute difference (MAD) against the motion-free reference. Note that the slice position might be different between scans due to inter-scan misplacement, so all images were registered to the reference position before calculating quantitative metrics.

For the patient study, T1/T2/T1ρ measurements of the same four normal appearing (NA) tissue compartments were derived at similar slice locations as in the healthy controls. For each measurement of each tissue, a one-way analysis of variance (ANOVA) was performed to evaluate the statistical significance between patients and healthy controls. The significance level was set as p=0.05. Receiver operating characteristic (ROC) curve analysis with binary logistic regression was performed using IBM SPSS Statistics to evaluate the accuracy in differentiating MS from healthy control based on either a single parameter (i.e., T1, T2, T1ρ) or the combination of three parameters (denoted as T1+T2+T1ρ), as measured by the area under the curve (AUC). A confidence interval (CI) of 95% was used. Measurements for all four tissue compartments were combined to calculate ROC curves.

4.3 Results

4.3.1 Phantom Study

Multitasking T1/T2/T1ρ maps were generated with good image quality and SNR (Figure 32). Multitasking measurements and reference measurements showed excellent correlation with R^2=0.996, 0.999, and 0.998 for T1/T2/T1ρ respectively, as well as excellent agreement with ICC=0.998, 0.996, and 0.998 for T1/T2/T1ρ, respectively.

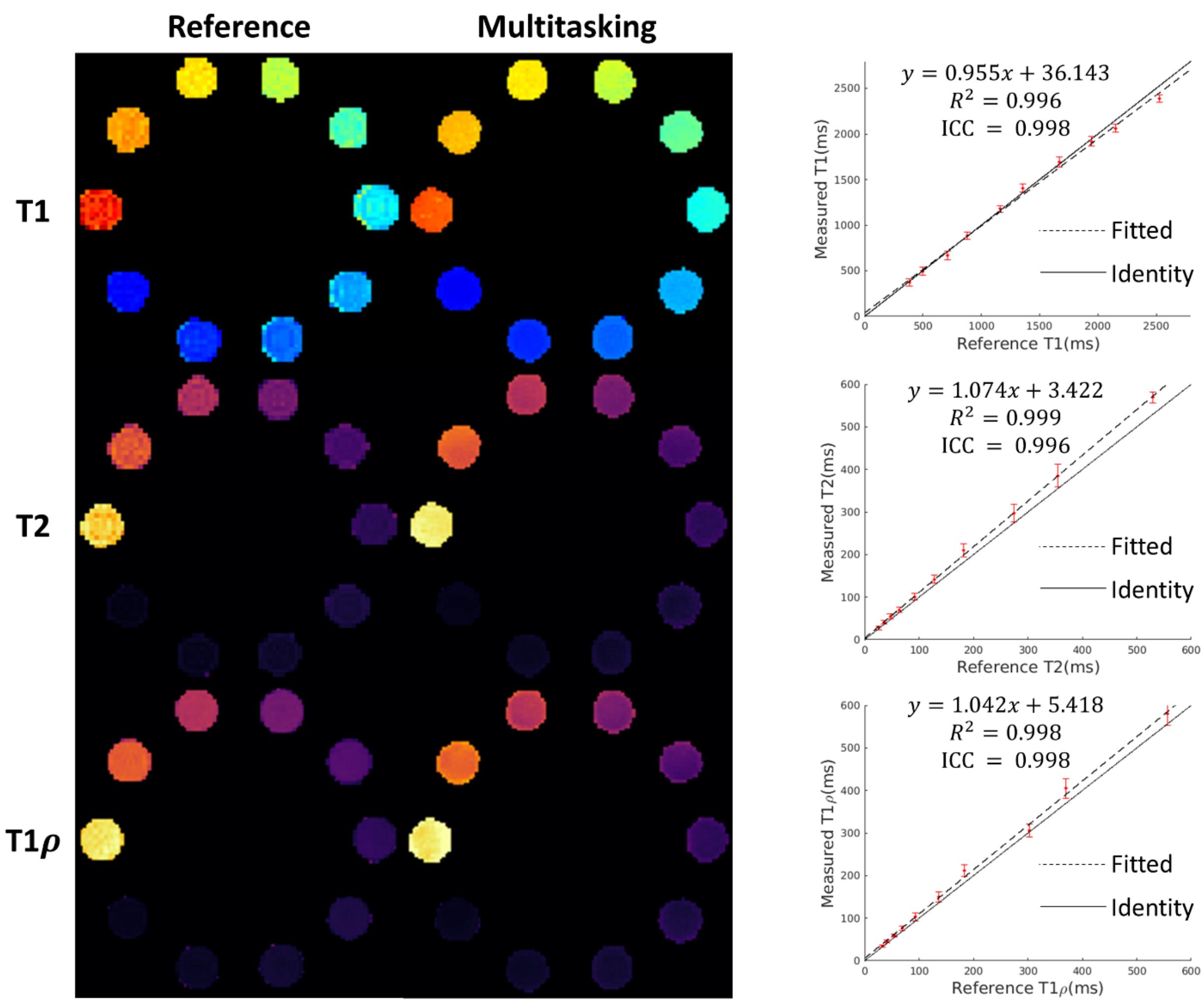

Figure 32. Phantom results of Multitasking and the references. Multitasking produces co-registered T1/T2/T1ρ maps with good image quality. Multitasking T1/T2/T1ρ measurements are in substantial quantitative agreement with reference measurements, as demonstrated by the high R^2 and ICC. The solid line represents identity (y=x) and the dotted line represents linear regression fitting.

4.3.2 Healthy Volunteer Study

Simultaneously acquired Multitasking T1/T2/T1ρ maps were of high quality and comparable with reference maps, with well-preserved brain tissue structure and contrasts (Figure 33). Multitasking measurement distributions in each tissue compartment were: WM (T1:843.6 ± 18.3; T2:75.9 ± 2.8; T1ρ:82.7 ± 3.2), GM (T1:1319.8 ± 28.9; T2:83.9 ± 3.6;

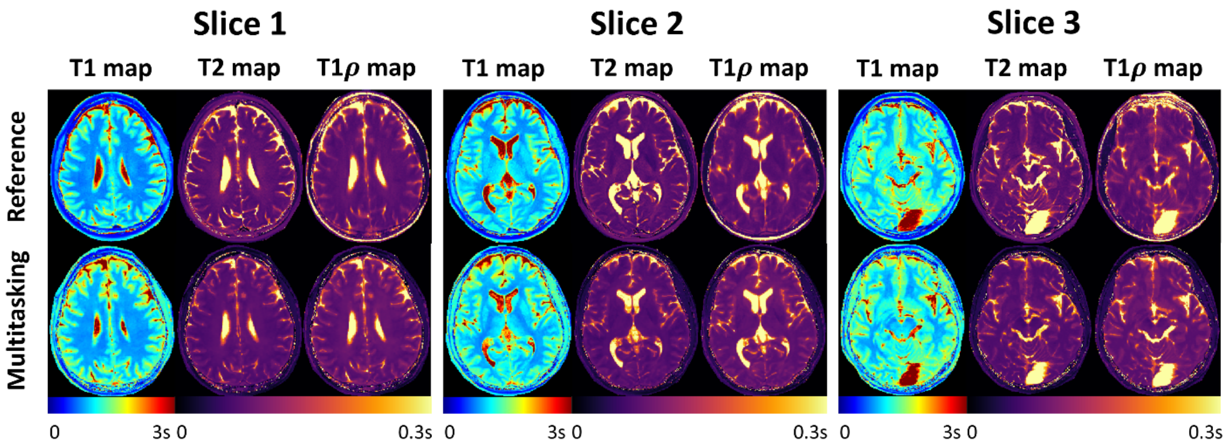

Figure 33. Example T1/T2/T1ρ maps generated by Multitasking and the reference methods in a healthy control. Multitasking maps show good image quality and are comparable with reference maps.

T1ρ:90.9 ± 3.0), putamen (T1:1110.3 ± 43.3; T2:72.0 ± 3.6; T1ρ:77.6 ± 2.7), and thalamus (T1:1041.5 ± 34.1; T2:76.0 ± 3.5; T1ρ:83.7 ± 3.8); Table 10 lists these in comparison to the references. Substantial quantitative agreement between Multitasking and the references was seen for T1/T2/T1ρ in all tissue compartments, with all ICC>0.81 within the "excellent" definition range[102] (Table 11).

Table 10. T1/T2/T1ρ measurements of *N*=14 healthy controls.

Healthy Control Measurements (N=14)		White Matter	Gray Matter	Putamen	Thalamus
Reference Measurements	T1 (ms)	789.6±22.6	1210.8±31.0	1051.8±46.5	987.2±32.7
	T2 (ms)	78.5±3.5	85.3±3.9	74.3±3.8	78.6±3.8
	$T1\rho$ (ms)	80.4±3.3	88.9±3.4	76.1±3.8	81.4±3.6
Multitasking Measurements	T1 (ms)	843.6±18.3	1319.8±28.9	1110.3±43.3	1041.5±34.1
	T2 (ms)	75.9±2.8	83.9±3.6	72.0±3.6	76.0±3.5
	$T1\rho$ (ms)	82.7±3.2	90.9±3.0	77.6±2.7	83.7±3.8

Table 11. Intraclass correlation coefficients between reference and Multitasking T1/T2/T1ρ measurements in four tissue compartments.

		White Matter	Gray Matter	Putamen	Thalamus
ICC (Reference vs Multitasking)	T1	0.86	0.90	0.92	0.92
	T2	0.88	0.87	0.85	0.84
	$T1\rho$	0.87	0.83	0.86	0.81

Small but statistically significant biases were seen between Multitasking and reference measurements: Multitasking T1 and T1ρ values were higher in all compartments (1.1%~9.0% higher for T1, and 2.0%~4.3% higher for T1ρ), while T2 values lower in all compartments

(1.6%~3.3% lower). Despite the measurement biases, values of all tissue compartments were within the literature range[35,98,101,133,149-152] where available. No T1ρ literature values of putamen and thalamus were found.

Bland-Altman plots demonstrated good scan-rescan repeatability of Multitasking experiments for T1/T2/T1ρ measurements on all tissue compartments (Figure 34). For all subjects and tissue compartments, maximum T1, T2 and T1ρ variations were all less than 5%. All ICCs between the 1st and 2nd Multitasking sessions were >0.91, also indicating "excellent" agreement (Table 12).

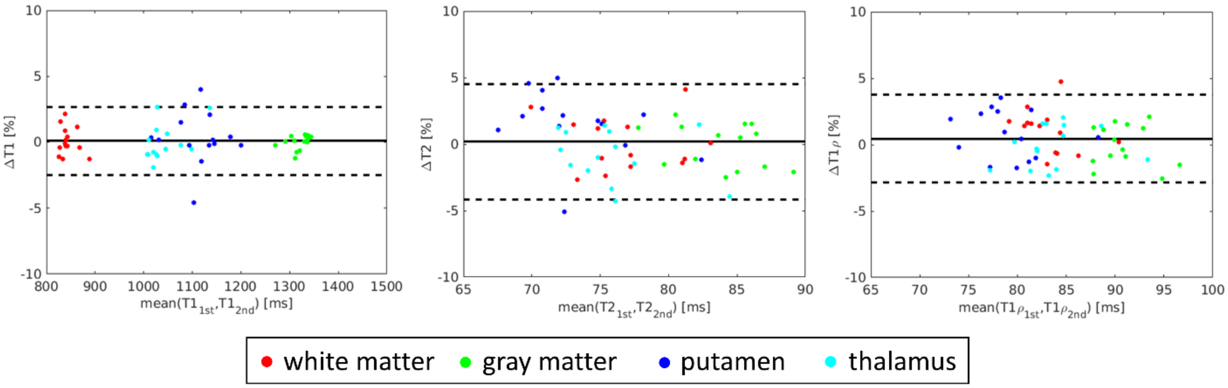

Figure 34. Bland-Altman analysis for the evaluation of scan-rescan repeatability of the 1st and 2nd Multitasking scans. Left to right: T1, T2, and T1ρ. Each tissue compartment corresponds to a single color. The dotted lines represent 95% confidence level. The solid lines represent mean percentage differences.

Table 12. Intraclass correlation coefficients between the 1st and 2nd Multitasking scans in four tissue compartments.

		White Matter	Gray Matter	Putamen	Thalamus
ICC (Multitasking 1st vs 2nd)	T1	0.91	0.96	0.93	0.95
	T2	0.94	0.93	0.90	0.92
	T1ρ	0.93	0.94	0.94	0.96

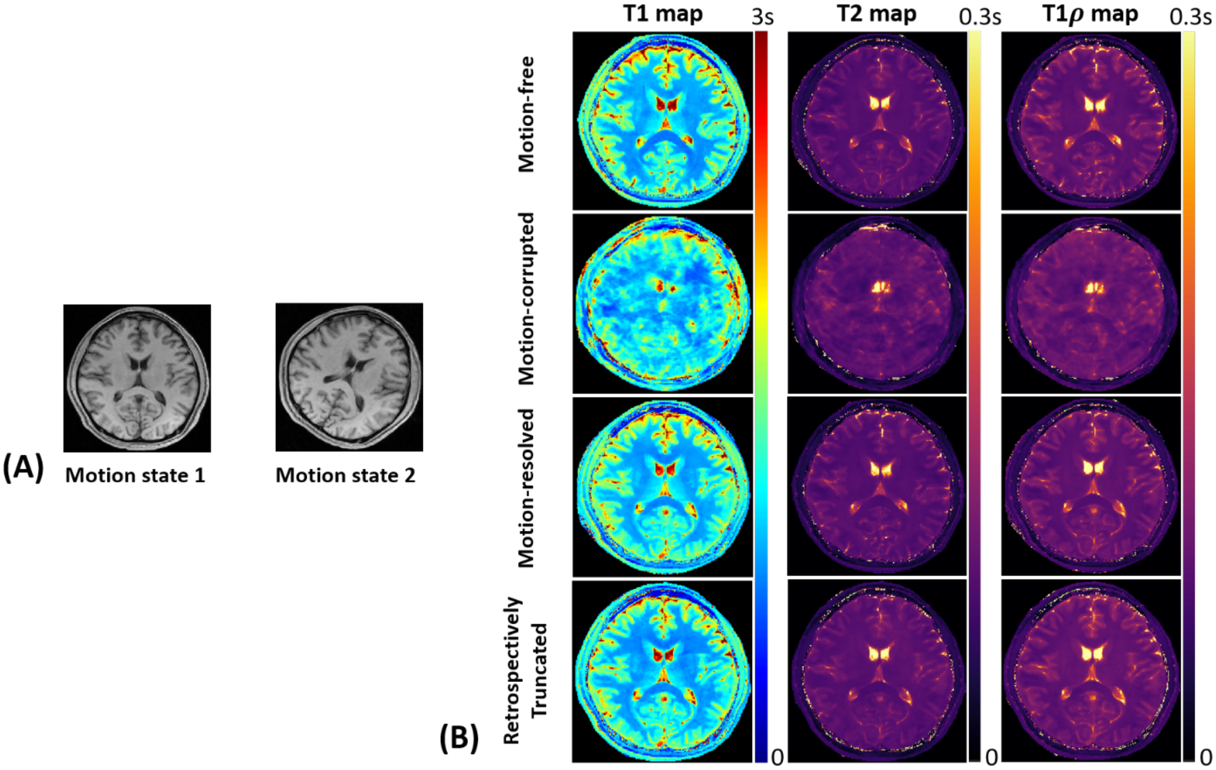

Figure 35. Demonstration of motion session 1 – in-plane "shaking" motion with two motion states. (A) Example frames of Multitasking images for two motion states. (B) Motion-free (reference), motion-corrupted, motion-resolved, and retrospectively truncated (i.e., using half of the k-space data belonging to a single motion state) T1/T2/T1ρ maps. With two in-plane motion states, motion-corrupted maps show substantial blurring and ghosting artifacts, while motion-resolved and retrospectively truncated maps show very good image quality.

4.3.3 Motion Investigation

For all motion experiments, different motion states are demonstrated (Figure 35A-38A) and example motion-free, motion-corrupted, motion-resolved, and retrospectively truncated T1/T2/T1ρ maps are provided (Figure 35B-38B).

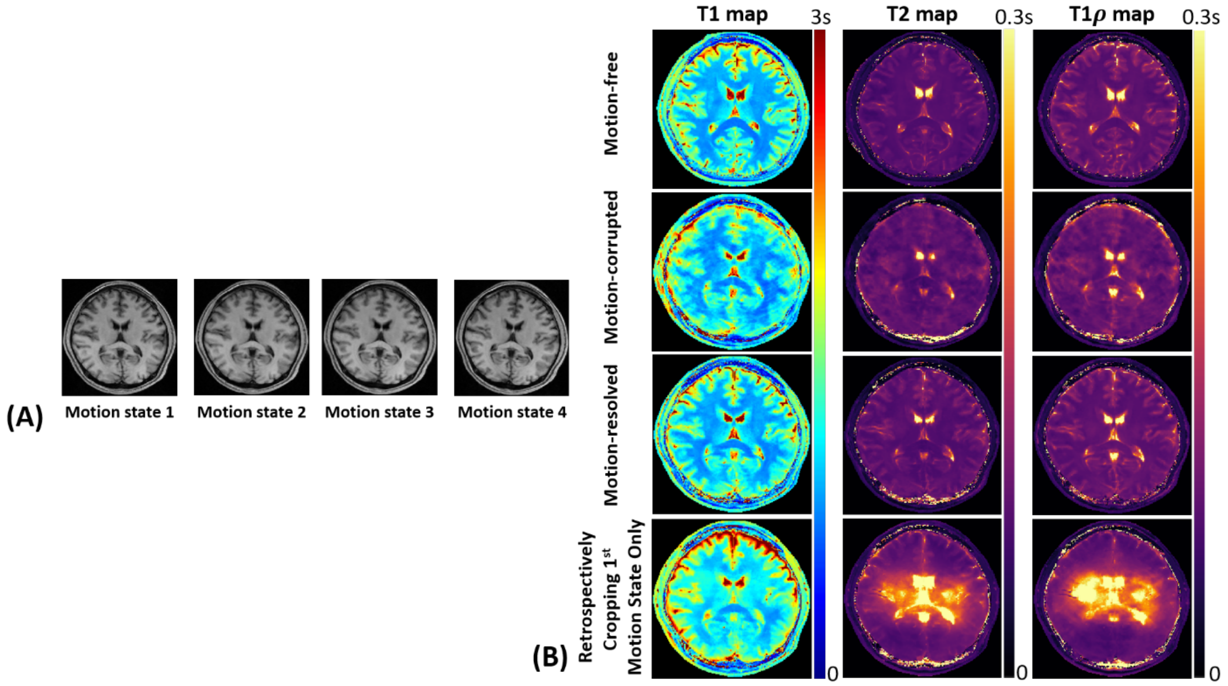

Figure 36. Demonstration of motion session 2 – in-plane "shaking" motion with four motion states. (A) Example frames of Multitasking images for four motion states. (B) Motion-free (reference), motion-corrupted, motion-resolved, and retrospectively truncated (i.e., using a quarter of the k-space data belonging to a single motion state) T1/T2/T1ρ maps. With four in-plane motion states, both motion-corrupted and retrospectively truncated maps show substantial deviation from the reference, as well as blurring and ghosting artifacts, while motion-resolved maps show decent image quality with very mild blurring at tissue boundaries.

For both in-plane and through-plane sessions with two motion states, motion-corrupted T1/T2/T1ρ maps are suffered from substantial ghosting artifacts, lower SSIM (session #1: 0.6615, 0.6259, 0.6458; session #3: 0.6447, 0.6256, 0.6154), and higher MAD (session #1: 239.6ms,

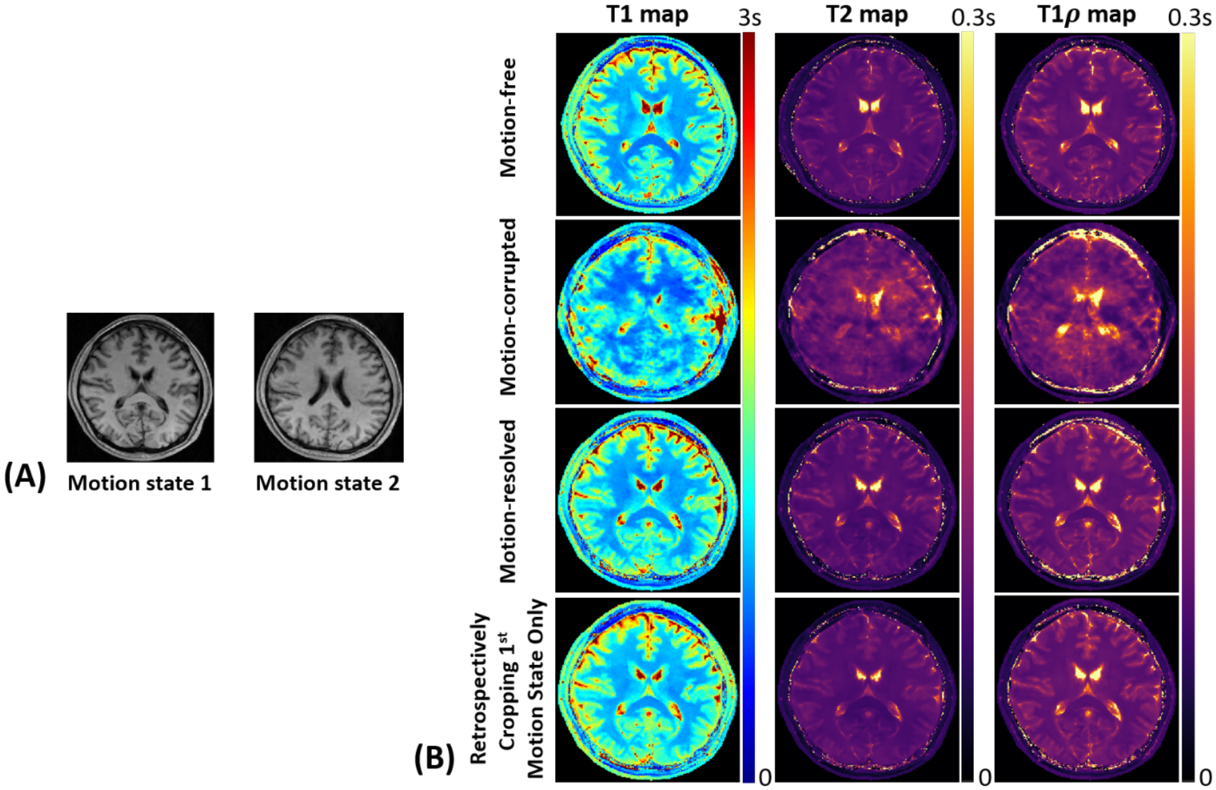

Figure 37. Demonstration of motion session 3 – through-plane "nodding" motion with two motion states. (A) Example frames of Multitasking images for two motion states. (B) Motion-free (reference), motion-corrupted, motion-resolved, and retrospectively truncated (i.e., using half of the k-space data belonging to a single motion state) T1/T2/T1ρ maps. Similar to motion session 1, motion-corrupted maps show substantial blurring and ghosting artifacts, while motion-resolved and retrospectively truncated maps show good image quality.

12.6ms, 11.3ms; session #3: 264.6ms, 16.4ms, 17.7ms). The standard deviation (SD) of all measurements are substantially higher. Motion-resolved and retrospectively truncated T1/T2/T1ρ maps are clean and comparable to the reference, with similar measurement distributions, higher SSIM (session #1 motion-resolved: 0.7714, 0.7352, 0.7461; session #1 retrospectively truncated: 0.7670, 0.7262, 0.7415; session #3 motion-resolved: 0.7040, 0.6879, 0.6870; session #3 retrospectively truncated: 0.6840, 0.6867, 0.6859), and lower MAD (session #1 motion-resolved: 139.1ms, 5.8ms, 6.1ms; session #1 retrospectively truncated: 146.9ms, 6.2ms, 6.8ms; session #3

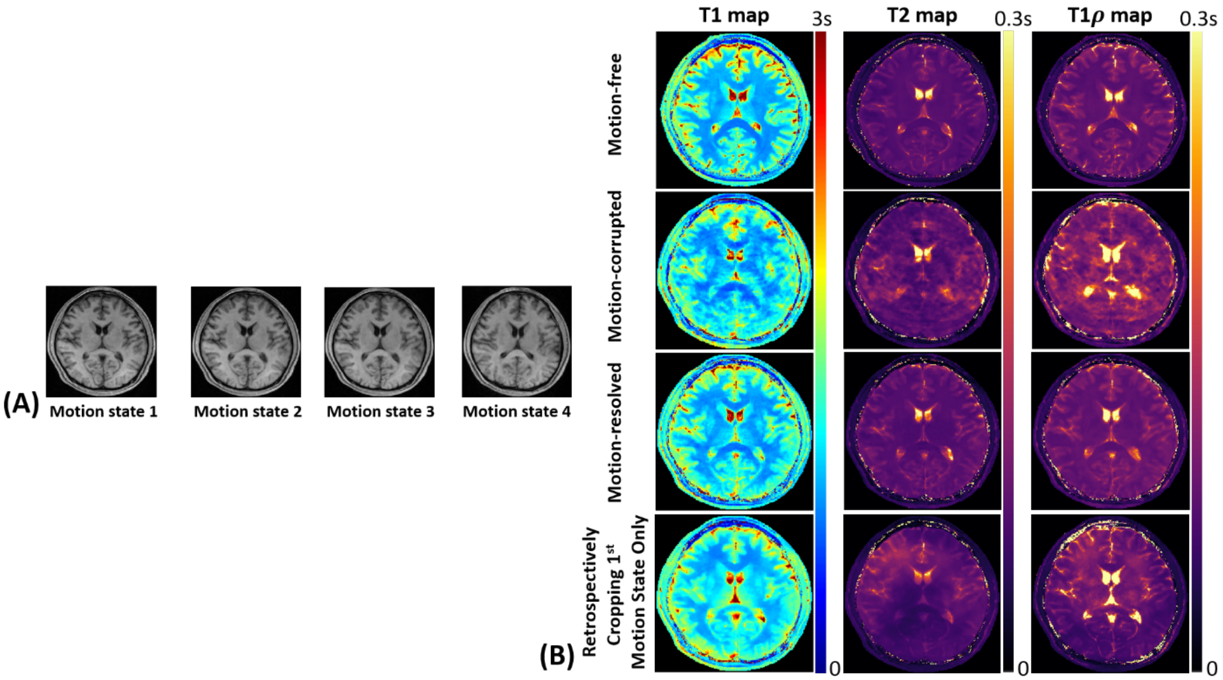

Figure 38. Demonstration of motion session 4 – through-plane "nodding" motion with four motion states. (A) Example frames of Multitasking images for four motion states. (B) Motion-free (reference), motion-corrupted, motion-resolved, and retrospectively truncated (i.e., using a quarter of the k-space data belonging to a single motion state) T1/T2/T1ρ maps. Similar to motion session 2, both motion-corrupted and retrospectively truncated maps show substantial deviation from the reference, as well as blurring and ghosting artifacts, while motion-resolved maps show decent image quality with mild blurring at tissue boundaries.

motion-resolved: 163.3ms, 8.1ms, 9.3ms; session #3 retrospectively truncated: 172.8ms, 8.4ms, 9.6ms).

For both in-plane and through-plane sessions with four motion states, both motion-corrupted and retrospectively truncated T1/T2/T1ρ maps exhibit substantial ghosting or undersampling artifacts, lower SSIM (session #2 motion-corrupted: 0.6509, 0.6423, 0.6444; session #2 retrospectively truncated: 0.6202, 0.6379, 0.6435; session #4 motion-corrupted: 0.6642, 0.6256, 0.6293; session #4 retrospectively truncated: 0.7199, 0.6459, 0.6480), and higher MAD (session #2 motion-corrupted: 192.3ms, 14.6ms, 13.0ms; session #2 retrospectively truncated: 281.9ms, 49.9ms, 45.7ms; session #4 motion-corrupted: 187.5ms, 13.9ms, 21.3ms; session #4 retrospectively truncated: 177.7ms, 12.2, 19.5ms). The SD of all measurements are substantially higher. Motion-resolved T1/T2/T1ρ maps are clean with values comparable to reference values. SSIM is much higher (session #2: 0.7348, 0.7052, 0.7095; session #4: 0.7315, 0.6992, 0.7015) and MAD is much lower (session #2: 157.2ms, 8.6ms, 9.2ms; session #4: 152.3ms, 8.0ms, 8.9ms). However, compared to two motion states, four motion states lead to less sharp and more blurring WM boundaries for both motion types.

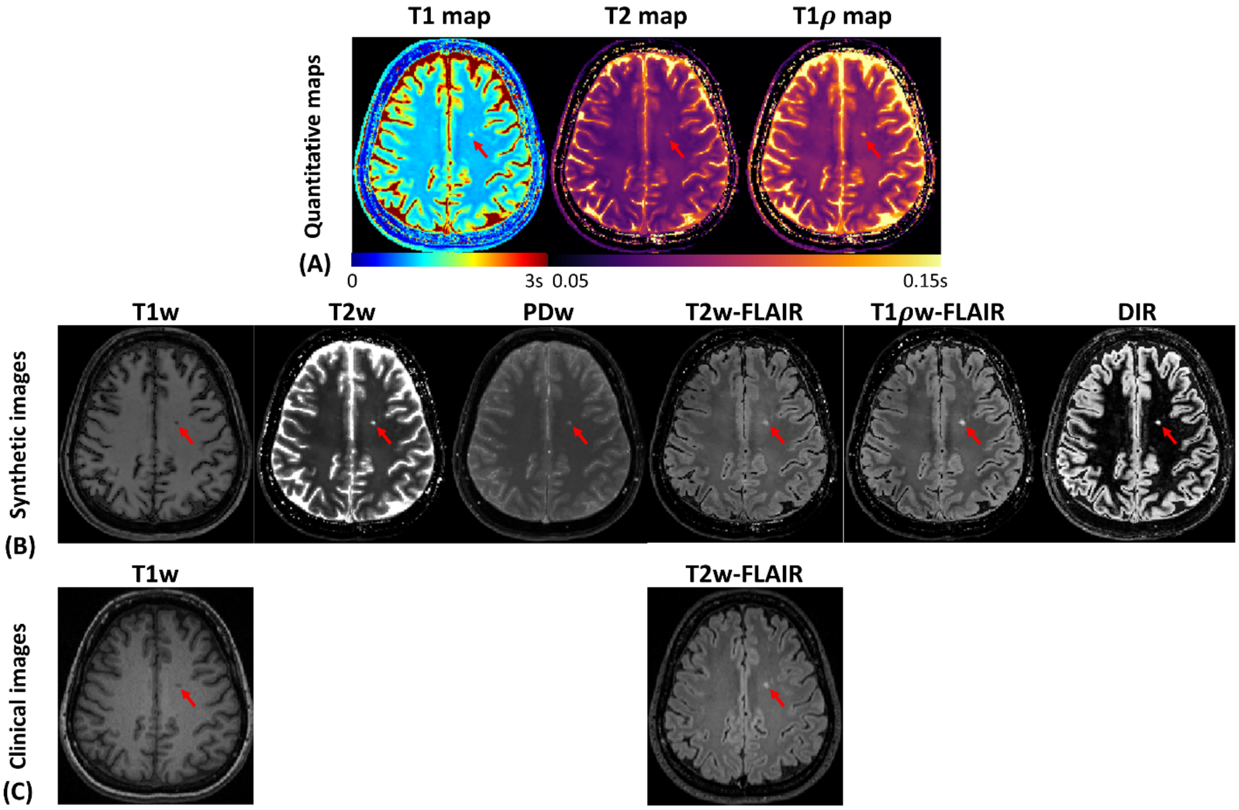

Figure 39. Clinical demonstration of a 56-year-old female RRMS patient with 20 years disease duration. (A) Multitasking T1/T2/T1ρ maps. (B) Synthetic T1w, T2w, PDw, T2w-FLAIR, T1ρw-FLAIR, and DIR images. (C) Clinical T1w and T2w-FLAIR images (the only clinical images available) which are comparable with the synthetic images. One white matter lesion (red arrow) is clearly delineated on both quantitative maps and synthetic images, among which T1ρ shows better lesion contrast than T2. T2w-FLAIR, T1ρw-FLAIR, and DIR show better lesion contrast with nulled CSF than T1w, T2w, and PDw.

4.3.4 Patient Study

Figure 39 showed example quantitative maps as well as synthetic and clinical weighted images of a 56-year-old female RRMS patient who had 20 years disease duration. The WM lesion was clearly delineated on Multitasking T1/T2/T1ρ maps (Figure 39A). Also note that the T1ρ map showed better lesion contrast against NAWM than the T2 map. Figure 39B demonstrated synthetic weighted images, where the lesion was clearly shown on T2w, T2w-FLAIR, T1ρw-FLAIR, and DIR. CSF was nulled on T2w-FLAIR, T1ρw-FLAIR, and DIR, yielding better delineation of lesion than other synthetic contrast-weighted images. It seemed that the lesion is most conspicuous on T1ρw-FLAIR and DIR. T1w and T2w-FLAIR were the only available corresponding clinical images with which the corresponding synthetic ones were comparable (Figure 39C).

Table 13. Patient T1/T2/T1ρ measurements in four tissue compartments. Statistical significance against healthy controls (HC) is evaluated. Asterisk (*) indicates significant difference (*p*<0.05).

RRMS Patients Measurements (N=8)	White Matter	Gray Matter	Putamen	Thalamus
T1 (ms)	900.1±13.0	1333.9±28.1	1095.7±36.9	1017.3±22.2
P-value vs. HC	3.9×10^{-7}*	0.179	0.498	0.102
T2 (ms)	78.7±1.9	86.5±1.3	73.2±1.7	77.8±2.4
P-value vs. HC	0.019*	0.063	0.409	0.850
T1ρ (ms)	86.9±2.5	95.8±3.0	80.5±2.1	86.5±2.5
P-value vs. HC	0.005*	0.001*	0.016*	0.024*

Table 13 showed population statistics for Multitasking measurements in RRMS patients and the results of comparisons against healthy controls. We found significant differences for T1 in NAWM (900.1±13.0, p=3.9x10^{-7}) compared to healthy controls. T2 was also significantly higher in NAWM of patients (78.7±1.9, p=0.019). Significantly higher T1ρ was observed in all four compartments: NAWM (86.9±2.5, p=0.005), NAGM (95.8±3.0, p=0.001), putamen (80.5±2.1, p=0.016), and thalamus (86.5±2.5, p=0.024).

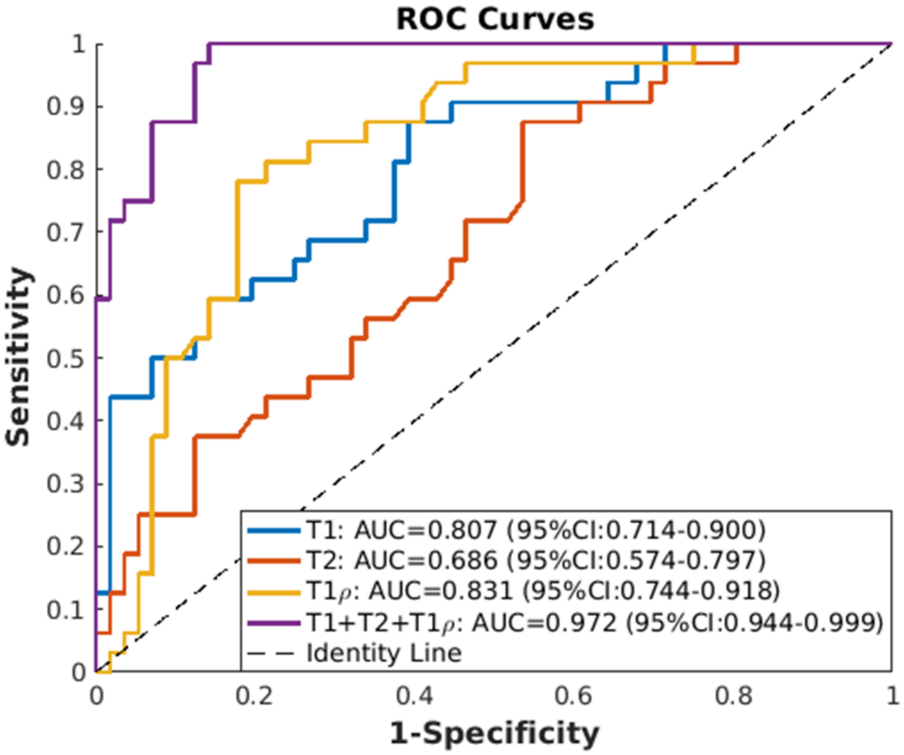

Figure 40. Receiver operation characteristic (ROC) curves in differentiating RRMS patients with healthy controls, using either single parameter or the combination of three parameters. The area under the curve (AUC) are: T1: AUC=0.807 (95%CI: 0.714-0.900), T2: AUC=0.686 (95%CI: 0.574-0.797), T1ρ: AUC=0.831 (95%CI: 0.744-0.918), T1+T2+T1ρ: AUC=0.972 (95%CI: 0.944-0.999). The dotted line represents identity reference line.

ROC analysis (Figure 40) showed that when using a single parameter, T1ρ had the highest AUC point estimate for discriminating MS with healthy control with AUC=0.831 (95%CI: 0.744-

0.918), followed by T1 with AUC=0.807 (95%CI: 0.714-0.900) and T2 with AUC=0.686 (95%CI: 0.574-0.797). The combination of all three parameters had significantly higher accuracy than any individual parameter, with AUC=0.972 (95%CI: 0.944-0.999).

4.4 Discussion

We extended the existing MR Multitasking technique to achieve simultaneous quantification of T1/T2/T1ρ with whole-brain coverage in a clinically feasible scan time. By modeling the underlying image as a multidimensional tensor, characterizing each relaxation process as a different time dimension, and exploiting the strong spatiotemporal correlations along and across dimensions, this framework is capable of accelerating the imaging session, thus producing an efficient MR exam in clinical settings.

Simultaneous multiparametric mapping approaches have been widely explored in recent years, as they have several significant merits: i) production of quantitative information rarely available in conventional clinical MR exams, which has the potential to have higher sensitivity, specificity, and reproducibility beneficial to inter-subject or inter-site comparison, longitudinal follow-up, and detection of biological tissue changes; ii) production of quantitative biomarkers that allow comprehensive measurement of tissue properties under various diseases; and iii) substantial acceleration compared to conventional quantitative MRI methods which are usually performed in separate scans, leading to shortened MR sessions, co-registered measurements, and significantly reduced motion artifacts. Popular approaches that quantify proton density, T1, T2, T2*, ADC, and perfusion and vascular permeability parameters have been proposed and drawn extensive interests, using MR fingerprinting, MR Multitasking, and more[58,62,69,71,72,84,86,153]. As an emerging contrast mechanism specially characterizing low-frequency biochemical motional process, T1ρ has yet to be fully explored, while the acquisition can be extremely inefficient (10-

20min) especially when whole anatomical coverage is desired[154-157]. Furthermore, with such a long scan time, clinical scans could be prone to motion artifacts. This work for the first time quantifies whole-brain T1ρ along with T1 and T2 simultaneously in 9min which is significantly shorter than separate reference T1/T2/T1ρ acquisition performed in 25min in this study, thus being promising for clinical research.

The proposed method produced high quality and co-registered multiparametric maps and T1/T2/T1ρ measurements; phantom vials and brain tissue compartments showed substantial quantitative agreement with reference measurements. Significantly different measurement biases were seen between Multitasking and the reference methods, which may be due to several factors. Firstly, the T1 differences could be related to both preparation scheme differences (IR vs. T2-IR/T1ρ-IR) and readout differences (TSE vs. FLASH). Furthermore, it has been shown that IR-TSE could lead to T1 underestimation in the brain compared to the traditional “gold standard” IR-SE[58]. Secondly, T2-preparations might lead to T2 underestimation due to B1 inhomogeneities as previously reported[71,103], while ME-SE was likely to cause T2 overestimation due to stimulated echo contamination[158]. Lastly, reference T1ρ mapping was subject to T1 contamination during the FLASH readouts, despite the implementation of multi-shot acquisition with 2x GRAPPA acceleration to allow fewer phase encoding lines per shot.

In this work, we investigated two commonly occurred types of motion — in-plane “shaking” motion and through-plane “nodding” motion, as well as motion timings during the scan. The results indicated that in-plane and through-plane motion did not make a difference in terms of the motion-resolved image quality, and thus could be treated equally in the imaging framework which was probably because of the 3D acquisition. However, the number of identified motion states mattered, as it was clear that when the subject moved three times, the resulting motion-resolved maps showed more blurring of the WM boundaries, compared against when the subject moved only once. This was probably because the head motion pattern was discrete rather than continuous or periodical, thus with the complicated brain tissue structure, if there were more motion states, more voxels close to tissue boundaries could belong to different tissues under different motion states, and the image tensor would have less correlation to be exploited along the motion dimension. For similar reason, the motion-resolved mapping quality could have also been degraded if the rotation angle was too large. Luckily, patients' head would be stabilized with cushions during clinical settings, preventing substantial motion from happening. On the other hand, we noted that by exploring the signal correlation between motion states, the proposed framework better recovered T1/T2/T1ρ maps than retrospectively truncating one motion state for image reconstruction, indicating that the signal correlation was exploited to help recover useful information. However, it seemed that the differences would be small if one motion state took up more than half of the scan duration.

It is reasonable to assume that the motion-resolved results would be improved if all the images were registered to one motion state before tensor subspace estimation as demonstrated in our abdominal work[73], as it would greatly restore the signal correlation. However, in the presence of rotational motion, image registration with affine transform would create non-Cartesian coordinates not inherently compatible with our Cartesian trajectory, leading to a much longer reconstruction time. Future works may investigate image registration with radial- or spiral-based trajectories which are more compatible with translational and rotational image registration in the k-space. Besides, future works will also include more subjects for statistical comparisons and other simultaneous multiparametric mapping techniques.

In our study, we generated six synthetic contrast-weighted images along with three quantitative maps, which in the future have the potential to replace conventional qualitative scans in the clinical workflow. Future work will compare the diagnostic accuracy of the synthetic and clinical images as further validation. In the results of this study, the MS lesion was conspicuous on all three parametric maps, among which T1ρ seemed to provide better lesion contrast than T2. As a result, the lesion on synthetic T1ρw-FLAIR appeared more prominent than in synthetic T2w-FLAIR. This was consistent to previous findings where T1ρ demonstrated 25% increased lesion CNR compared to T2[35]. T1-based synthetic DIR also showed excellent lesion contrast. However, whether T1 or T1ρ is better in terms of lesion characterization and diagnostic values needs further investigation. T1w, T2w, and PDw appeared to have less diagnostic value compared to the other three synthetic images due to reduced lesion contrast, but could still be important in other neurological diseases.

Consistent with previous findings, the significant differences for T1/T2/T1ρ in NAWM could indicate WM damage caused by demyelination, axonal degeneration, and inflammation[35,121,159,160]. Cortical and deep GM pathologies are also prominent but are less detected with conventional MRI techniques due to low myelin densities and reduced number of axons in GM cellular matrices[161,162]. Inflammation of GM is less pronounced than WM during progressive stages of MS, and GM damages could involve more subtle tissue changes[161,162]. In our study, only T1ρ showed significant differences in NA cortical and deep GM, suggesting the presence of GM damage could possibly be associated with low-frequency pathological processes and chemical exchanges. However, the intrinsic mechanism of increased T1ρ in NAGM remains unknown. These results indicated the potential of T1ρ for the evaluation of MS, especially cortical and deep gray matter pathologies since accurate detection of lesions in these brain regions still remains an unmet need currently in MS. Furthermore, ROC analysis suggested that T1ρ may better discriminate RRMS patients from healthy controls than T1 and T2, and showed that the combination of T1/T2/T1ρ was better than using either a single parameter alone. This indicates that T1/T2/T1ρ offer complementary tissue information and could serve as potential tissue biomarkers for diagnosis and treatment monitoring of MS. Future works will focus on a more comprehensive clinical validation on a larger cohort with other MS phenotypes.

One major limitation of this work is that we have yet to achieve ≤1.0mm slice resolution in a reasonable scan time, which is a common practice in clinical brain MRI, especially targeting MS. Whole-brain coverage cannot be sacrificed because MS lesions are likely to occur throughout the brain and down to the spinal cord. The current 3.5mm slice thickness may lead to missed detection of small lesions, or inaccurate lesion characterization due to partial volume effects. Future technical improvement will focus on shortening the scan time for higher-resolution imaging, for example by deep-learning super-resolution in the slice direction[163,164].

4.5 Conclusion

Three-dimensional, motion-resolved, whole-brain simultaneous T1/T2/T1ρ quantification is achieved in 9min with MR Multitasking. This novel technique produces T1/T2/T1ρ values in substantial quantitative agreement with reference methods, demonstrates excellent scan-rescan repeatability, and provides synthetic contrast-weighted images in addition to the three quantitative maps. Multitasking produces artifact-free multiparametric maps under in-plane and through-plane motion, which offers novel insights to handle motion in brain MRI exams. The combination of T1/T2/T1ρ better discriminates MS patients from healthy controls as compared to using a single measurement alone. Future work will focus on achieving higher slice resolution, dealing with motion, and more comprehensive clinical studies with larger cohorts.

Chapter V Translation of the Proposed Quantitative Multiparametric MRI Techniques to Potential Applications in Other Body Organs

5.1 B1+-Compensated, 3D Whole-Breast T1, T2, and ADC Mapping with MR Multitasking

5.1.1 Introduction

Currently clinical breast MRI mostly adopt qualitative imaging techniques such as T1w dynamic contrast enhanced (DCE) imaging and T2w imaging. Qualitative T1w DCE and T2w imaging have shown promise for clinical breast tumor diagnosis. For example, T1W DCE enables the detection and assessment of morphological and kinetic patterns of benign and malignant breast tumors with high sensitivity (over 90%)[165]. T2w imaging provides information that contributes to benign and malignant lesion characterization[166]. However, qualitative imaging is subject to major limitations. T1w DCE has low to moderate specificity (72%) for lesion characterization[167], and T2w imaging is challenging to discriminate benign lesions, mucinous carcinoma and necrotic tumors that all produce high signal intensity on T2w images[168]. On the other hand, quantitative MRI that measures T1, T2, and ADC has significant clinical benefits in breast MRI. For instance, dynamic T1 mapping would contribute to direct quantification of contrast agent concentration curves in clinical DCE MRI[72]. T2 mapping has the potential for characterizing breast lesion stages and monitoring cancer progression after chemotherapy[169,170]. ADC mapping has been used for prediction of pathologic response in breast cancer[171], tumor detection with higher accuracy than mammography and comparable sensitivity and specificity than contrast-enhanced MRI[172,173], and non-contrast screening on regular basis[24]..

Despite the significant potential of T1, T2, and ADC quantification in clinical breast MRI, there are two major challenges. First, conventional quantitative T1, T2, and ADC mapping are typically acquired in separate 2D scans which have the disadvantages of inefficient acquisition, mis-registration due to intra-scan misplacement, and image distortion. Second, the presence of notable nonuniformity of the B1+ field in breast coils causes the actual flip angle to be deviated from the nominal flip angle[174-176]. This B1+ field inhomogeneity is mostly caused by large FOV in bilateral breast MRI, as well as the off-center breast positions in the coils. At 3T, ~40% flip angle variation across the breast and 30%-50% flip angle variation across the chest can be expected which results in inaccurate T1 measurements[177,178].

In this section, we extend the simultaneous T1/T2/ADC quantification technique proposed in Chapter 3 to the breast, which allows co-registered and distortion-free T1, T2, and ADC maps with whole-breast coverage in a single 8min scan. We especially incorporate a separately acquired B1+ map into the multiparametric fitting process to compensate for the nonuniform B1+ variation, and thus improve T1 quantification accuracy.

5.1.2 Methods

5.1.2.1 Pulse Sequence Design

The design of the pulse sequence extends from Chapter 3, except that all preparation pulses are implemented in an interleaved manner throughout the entire scan to make the acquisition more motion robust (Figure 41). Data acquisition follows the strategy introduced in Chapter 3.

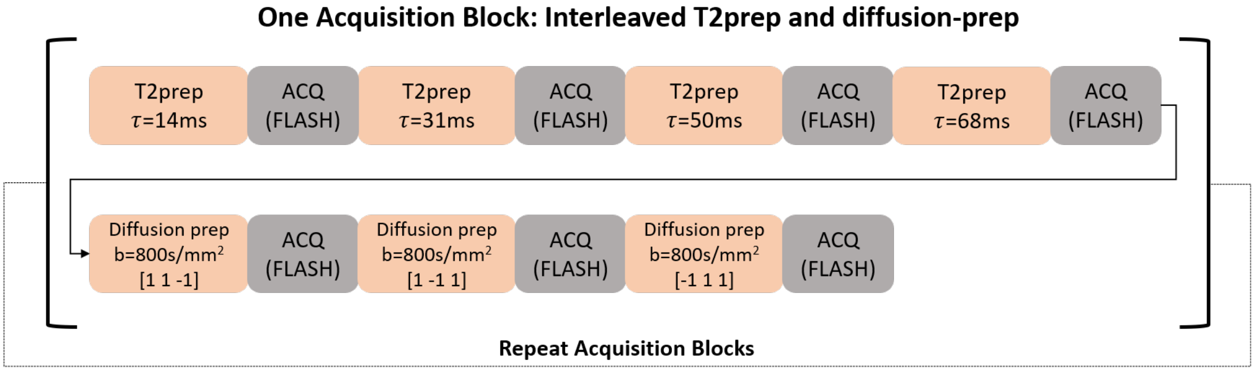

Figure 41. The pulse sequence diagram for whole-breast T1/T2/ADC Multitasking. Four T2-preparation modules and three diffusion-preparation modules are interleaved to form one acquisition block which repeats multiple times so that all preparations cycle throughout the entire scan for data acquisition.

5.1.2.2 B1+ Field Inhomogeneity Compensation

B1+ information will be separately obtained using a turbo FLASH sequence preceded by a target pre-saturation pulse with a nominal flip angle α_{B1+}[179]. The actual flip angle of this pulse can be calculated voxel-by-voxel as:

$$\hat{\alpha}_{B1+} = \arccos(\frac{I_\alpha}{I_0}), \tag{5.1}$$

where I_α and I_0 represent the signal intensities of the two images with and without the pre-saturation pulse. A spatial variation map can be derived by normalizing the actual flip angle with the nominal flip angle α_{B1+} of the pre-saturation pulse:

$$c = \frac{\hat{\alpha}_{B1+}}{\alpha_{B1+}}, \tag{5.2}$$

which is then applied to the nominal FLASH flip angle α used in the Multitasking sequence (i.e., $c \cdot \alpha$) as an initial guess for the multiparametric fitting process described in Eqs. (3.1) and (3.2).

5.1.2.3 Phantom Study

Data were collected on a 3T clinical scanner (MAGNETOM Vida, Siemens Heathineers, Erlangen, Germany) equipped with a 16-channel breast coil on a homemade T1 phantom[70] to evaluate the B1+-compensated T1 mapping accuracy. The reference T1 map was collected using an IR-TSE sequence with FOV=320x240mm^2, in-plane resolution=1.6x1.6mm^2, slice thickness=5mm, 9 inversion times TI=[50, 200, 275, 350, 500, 1000, 1500, 2400, 3000]ms. The reference B1+ map was collected with nominal flip angle $\alpha_{B1+} = 80°$ with the same FOV and in-plane resolution as the reference T1 map. The Multitasking imaging protocol was: FOV=320x240x50mm^3, voxel size=1.6x1.6x5mm^2, 4 T2-prep with durations τ=[14, 31, 50, 68]ms, 3 D-prep with one b-value b=800s/mm^2 and 3 noncolinear diffusion directions d=[1 1 -1], [1 -1 1], [-1 1 1], the duration of the D-prep was 31ms with a 55mT/m gradient amplitude on each axis, FLASH TR/TE=11.1/5.8ms, nominal FLASH flip angle $\alpha = 5°$, and repetition time (the time between two preparation pulses)=2600ms with an 1000ms gap.

5.1.2.4 In vivo Study

The in vivo study was approved by the IRB of our institute. All volunteers gave written informed consent before the study. N=13 healthy volunteers were recruited and were scanned on the MAGNETOM Vida scanner. In vivo protocols included a 3-view localizer, a fat-saturated T1-weighted sequence, a fat-saturated T2-STIR sequence, an ME-SE sequence with 6 echo times TE=[14, 28, 42, 56, 70, 84]ms for reference T2 mapping, a DW-RSEPI sequence with b-values=[50, 800]s/mm^2 and 3 noncolinear directions for reference ADC mapping, and reference B1+ maps that were collected with nominal flip angle $\alpha_{B1+} = 80°$. There is no widely accepted T1 mapping method in breast MRI as a reference. ME-SE, DW-RSEPI, and B1+ maps were all acquired with FOV=320x240mm^2, in-plane resolution=1.6x1.6mm^2, slice thickness=5mm. The Multitasking imaging protocol was: FOV=320x240x160mm^3, voxel size=1.6x1.6x5mm^2, 4 T2-prep with durations τ=[14, 31, 50, 68]ms, 3 D-prep with one b-value b=800s/mm^2 and 3 noncolinear diffusion directions d=[1 1 -1], [1 -1 1], [-1 1 1], the duration of the D-prep was 31ms with a 55mT/m gradient amplitude on each axis, FLASH TR/TE=11.1/5.8ms, nominal FLASH flip angle $\alpha = 5°$, and repetition time (the time between two preparation pulses)=2600ms with an 1000ms gap. The Multitasking sequence was run twice on each volunteer to test the in vivo repeatability, with a scan time of 8min each.

5.1.2.5 Image Analysis

All the reconstructions were performed on a Linux workstation with a 2.70GHz dual 12-core Intel Xeon processor equipped with 256GB RAM and running MATLAB 2017a. The spatial factor matrix **U** was solved by directly incorporating the model-based phase correction into the optimization problem described in Eq. (3.9) and using a 16GB GPU to improve the reconstruction speed. Voxel-wise multiparametric fitting of A, α, T1, T2, and the diffusion coefficients of 3 directions D_1, D_2 and D_3 was performed based on Eqs. (3.1)-(3.2), both with B1+ compensation (i.e., using the B1+-modulated flip angle as the initial guess of α) and without B1+ compensation (i.e., using the nominal 5° flip angle as the initial guess of α).

5.1.2.6 Quantitative Analysis

For phantom study, T1 values for each vial were calculated both with and without B1+ compensation. Linear regression was performed to evaluate the correlation between Multitasking

T1 mapping and reference T1 mapping. ICCs were calculated using IBM SPSS Statistics (Armonk, New York) with a two-way mixed model and a confidence level of 95% to evaluate the quantitative agreement between Multitasking T1 mapping and reference T1 mapping.

For in vivo study, the ROI was selected as the breast tissues in three slices located at the upper, mid, and lower regions of the acquired 3D volume. Measurement populations of T1/T2/ADC within the breast tissue were compared between Multitasking and the references. ICC was computed also using IBM SPSS Statistics to evaluate the quantitative agreement between Multitasking and reference T1/T2/ADC measurements. Bland-Altman analysis was performed to evaluate the in vivo repeatability between the two Multitasking scans.

5.1.3 Results

5.1.3.1 Phantom Study

Figure 42 shows the normalized B1+ map of the phantom over the nominal 80° flip angle of the pre-saturation pulse. Substantial B1+ variation was observed across the FOV, where the actual flip angle had a ∼10% increase over the left vials and a ∼10% decrease on average over the right vials, compared to the nominal flip angle. As a result, without B1+ compensation, Multitasking T1 values on both sides substantially deviated from the reference T1 values, with very poor correlation (R^2=0.503) and moderate quantitative agreement[102] (ICC=0.72). With B1+ compensation, Multitasking T1 values were comparable with reference T1 values on both sides, with very good correlation (R^2=0.973) and excellent quantitative agreement[102] (ICC=0.99). T2 maps and ADC maps were identical with or without B1+ compensation (results not shown here).

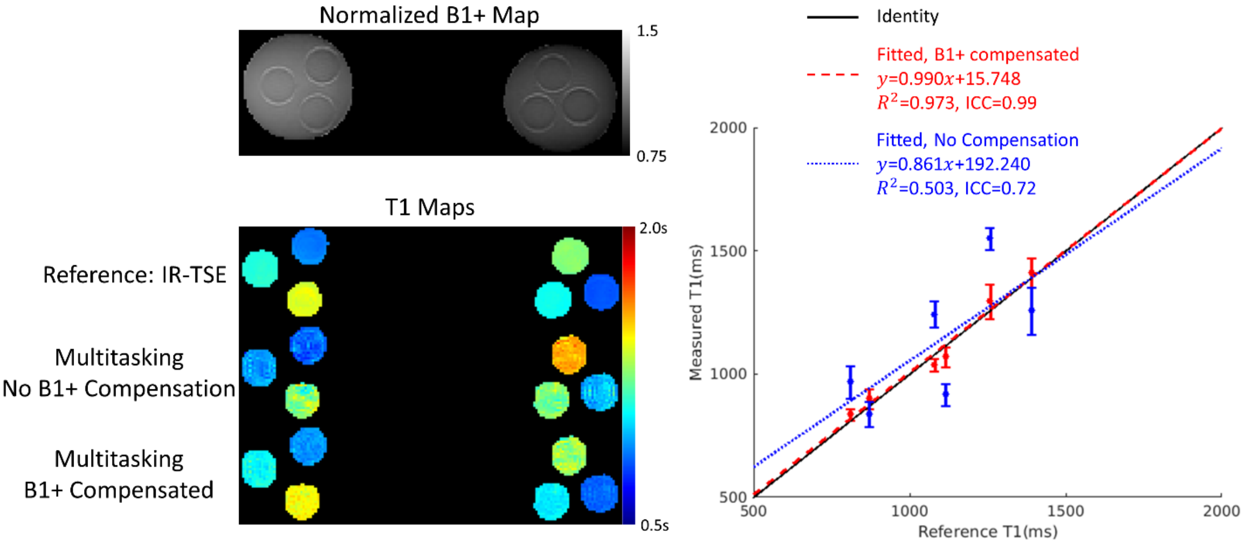

Figure 42. Demonstration of B1+ compensation in the phantom. Left top: The normalized B1+ map demonstrates the nonuniform B1+ field across the FOV. Left bottom: T1 maps generated from IR-TSE, Multitasking without B1+ compensation, and Multitasking with B1+ compensation. With B1+ compensation, the estimated T1 map is comparable with the reference. Right: regression analysis between reference and Multitasking T1 measurements with and without B1+ compensation. With B1+ compensation, T1 measurements show better correlation and agreement with the reference than without B1+ compensation with substantially higher R^2 and ICC.

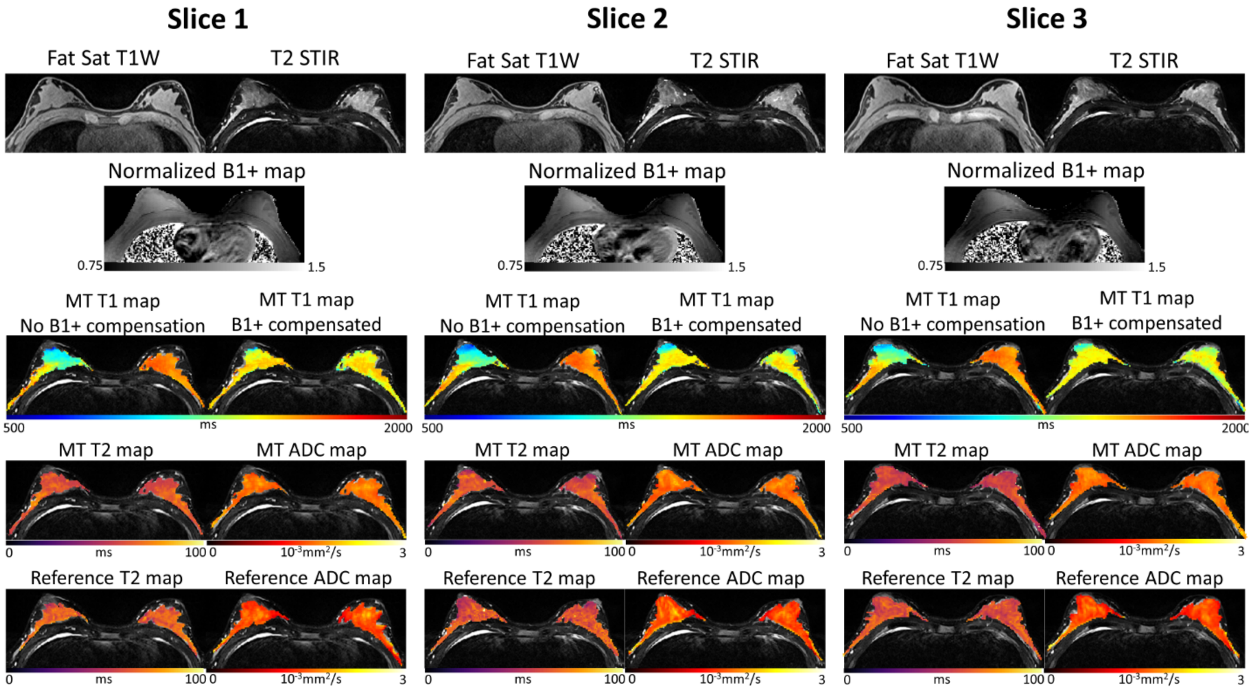

Figure 43. In vivo demonstration on a healthy volunteer for simultaneous T1/T2/ADC mapping of three slices. For each slice, the first row shows the clinically adopted fat saturated T1-weighted image and STIR image. The second row shows the separately acquired B1+ map (normalized with the prescribed 5° flip angle) which demonstrates the nonuniform B1+ field across the FOV. The third and fourth rows show the T1/T2/ADC maps generated from the Multitasking framework, where specifically, the third row shows the fitted T1 maps without and with B1+ compensation. Uniform T1 maps are produced with B1+ compensation, while substantial T1 variation is present without B1+ compensation. The T2/ADC maps are the same with or without B1+ compensation, as the flip angle term only interact with T1. The fifth row shows the reference T2 and ADC maps. Multitasking T2/ADC maps are consistent with the reference T2/ADC maps.

5.1.3.2 In vivo Study

Figure 43 shows example in vivo T1W and T2-STIR images, normalized B1+ maps over the nominal 80° flip angle of the pre-saturation pulse, as well as Multitasking and reference quantitative maps overlaid on T2-STIR in one healthy volunteer. Notable B1+ variation was observed in vivo across the FOV, with ~15% increase in the flip angle over the left breast, and ~10% decrease over the right breast. Multitasking T1/T2/ADC maps were co-registered. T2/ADC maps were consistent with the references. Without B1+ compensation, Multitasking T1 map was

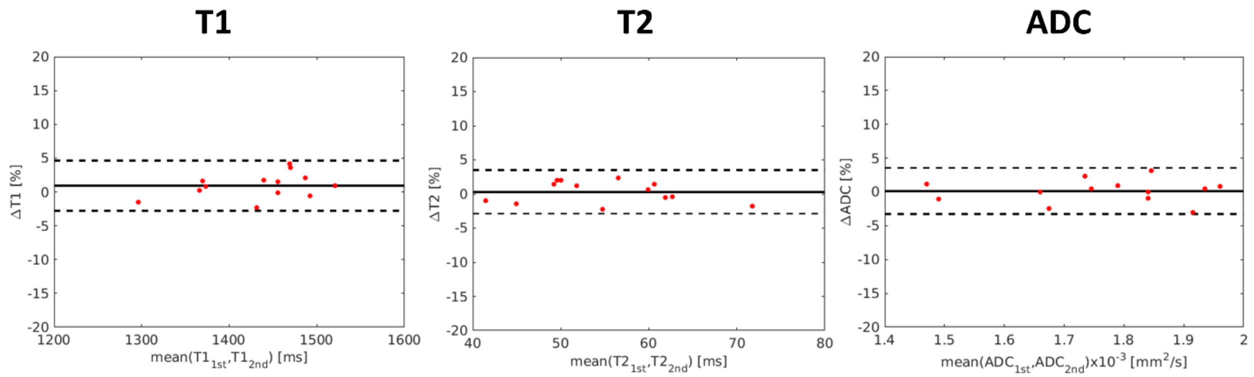

Figure 44. Bland-Altman plots showing the in vivo repeatability of T1/T2/ADC measurements between the first and second Multitasking experiments. All three parameters demonstrate good repeatability.

subject to B1+ inhomogeneity, leading to nonuniform T1 values on each side of the breast with a mean difference ~700ms. B1+ compensation produced uniform T1 values on both sides, which was reasonable for a healthy person. Bland-Altman plots demonstrated excellent in vivo repeatability between the 1st and 2nd Multitasking sessions, with maximum variations <5% for T1/T2/ADC measurements (Figure 44). Multitasking T1/T2/ADC measurements (T1: 1432.6 ± 63.2ms; T2: 55.0 ± 8.3ms; ADC: 1.76 ± 0.15x10^{-3}mm^2/s) and reference T2/ADC measurements (T2: 58.1 ± 7.9ms; ADC: 1.70 ± 0.15x10^{-3}mm^2/s) were all within literature range[24,36,174,180]. Multitasking T2/ADC were in excellent quantitative agreement with reference values, with ICC>0.94[102] (Table 14).

Table 14. T1/T2/ADC values of literature range, measurement population of T1/T2/ADC from B1+-compensated Multitasking, and T2/ADC from reference approaches on n=13 healthy volunteers.

	Literature Range	Reference (n=13)	Multitasking (n=13)	ICC (Reference vs Multitasking)
T1 (ms)	1049~1680		1432.6±63.2	
T2 (ms)	46~71	58.1±7.9	55.0±8.3	0.941
ADC (x10^{-3}mm^2/s)	1.51~2.09	1.70±0.15	1.76±0.15	0.953

5.1.4 Discussion and Conclusion

The proposed simultaneous T1, T2, and ADC mapping technique was translated to the breast. Multiparametric fitting was performed with prior knowledge of B1+ field information across the bilateral breast FOV, which compensated for the substantial B1+ inhomogeneity in the breast coil, leading to accurate, repeatable, and co-registered T1/T2/ADC measurements consistent with reference methods where available.

The most efficient approach clinically to achieve T1/T2/ADC mapping of the breast so far is to combine a 3D MR Fingerprinting approach which has been proposed for breast lesion characterization with a 6min scan time[36], and a separate DWI acquisition which uses the RESOLVE technique to conquer the image distortion[54] with another 6min scan time, adding up to 12min scan in total. The proposed method enabled the quantification of T1/T2/ADC with who-breast coverage in only 8min.

The substantial B1+ field inhomogeneity across the entire FOV has been a long standing problem in breast MRI. Pineda et al. calculated a partial B1+ map from the fat in the breast as a reference tissue, as fat is an ideal reference tissue with spatially homogeneous T1 and low interpatient variability, which was subsequently interpolated over the breast tissue regions to acquire the entire B1+ map across the whole FOV[174]. Sung et al. systematically evaluated the impact of B1+ correction on the T1 mapping accuracy, and found 52% T1 estimation bias in fat between breasts using variable flip angle T1 mapping without proper B1+ correction, while the T1 variation reduced to 7% with B1+ correction[175]. In this work, we found notable B1+ variation with ~10%-15% increase over the left breast and ~10%-15% decrease over the right breast. Our solution was simple and convenient, which used a separately acquired B1+ map to modulate the nominal flip angle as the initial guess of the multiparametric fitting, reducing T1 bias substantially.

This also indicated that our nonlinear fitting was sensitive to the choice of initial guess, as different T1 and flip angle combinations might give the same results. In the future, other B1+ robust T1 mapping methods will be explored, such as double flip angle configuration[181].

We extended the simultaneous T1/T2/ADC mapping technique to the breast with 3D whole-breast coverage. The substantial transmit field inhomogeneity in the breast coil was compensated by incorporating the prior knowledge of a separately acquired B1+ map, which substantially improved the T1 mapping accuracy. High quality, co-registered T1/T2/ADC maps were generated without image distortion. Future work will focus on clinical validation on tissue characterization of breast cancer patients.

5.2 Non-ECG, Free-Breathing Simultaneous Myocardial T1 and T1ρ mapping with MR Multitasking

5.2.1 Introduction

Quantitative cardiovascular magnetic resonance imaging techniques have been widely adopted in clinical research and diagnosis of various cardiovascular diseases. For example, myocardial T1 and T2 mapping allow quantitative assessment of myocardial abnormalities such as focal or diffusion fibrosis, myocarditis, ischemic diseases, and non-ischemic cardiomyopathies[18]. T1ρ is sensitive to tissue composition of fibrosis and normal cardiomyocytes, allowing enhanced scar contrast at high spin-lock frequency compared to T2[182]. T1ρ also shows promise as a non-contrast alternative for the detection and clinical evaluation of acute and chronic myocardial infarction[183].

One major technical challenge for quantitative cardiovascular MRI is to handle multiple overlapping dynamic processes during data acquisition. Physical image contrasts to be quantified (i.e., T1, T2, T1ρ) are mixed with physiological motion (i.e., cardiac and respiratory motion). Established solutions to address this issue would be to freeze cardiac and respiratory motion using ECG, breath-hold short sequences, or respiratory navigator techniques. Clinical T1, T2, and T1ρ maps are typically obtained separately with these freezing mechanisms using modified look-locker inversion recovery (MOLLI)[41], T2-prepared FLASH/bSSFP[184], or T1ρ-prepared FLASH/bSSFP sequences[182,183], which may lead to inefficient imaging sessions, complicated clinical workflows, and misaligned images due to multiple breath holds. Furthermore, it would be especially challenging on patients with cardiac arrhythmias or irregular breathing patterns.

In this section, we propose to simultaneously resolve four overlapping image dynamics, namely, T1, T1ρ, cardiac motion, and respiratory motion, in a single continuously acquired, free-breathing MR exam with no reliance on ECG triggering, by extending the technique introduced in Chapter 4 to especially take care of cardiac and respiratory motion, which enables a "push-button" cardiac MR exam that simplifies the clinical workflow, eliminating the need for multiple inter-scan set-ups.

5.2.2 Methods

5.2.2.1 Pulse Sequence and Data Acquisition

T1 and T1ρ weightings are generated by cycling through multiple B0- and B1-insensitive T1ρ-IR preparations with different spin-lock times at one spin-lock frequency. Imaging data $\mathbf{d}_{\text{img}}$ are collected with a golden-angle radial trajectory (θ=111.2467°). Subspace training data $\mathbf{d}_{\text{tr}}$ are collected periodically for every three readouts at the center k-space line (θ=0°) which serves dual purposes: i) for multidimensional temporal subspace modeling in the LRT image model; and ii) for cardiac and respiratory binning. Figure 45 shows the sequence diagram and sampling strategy.

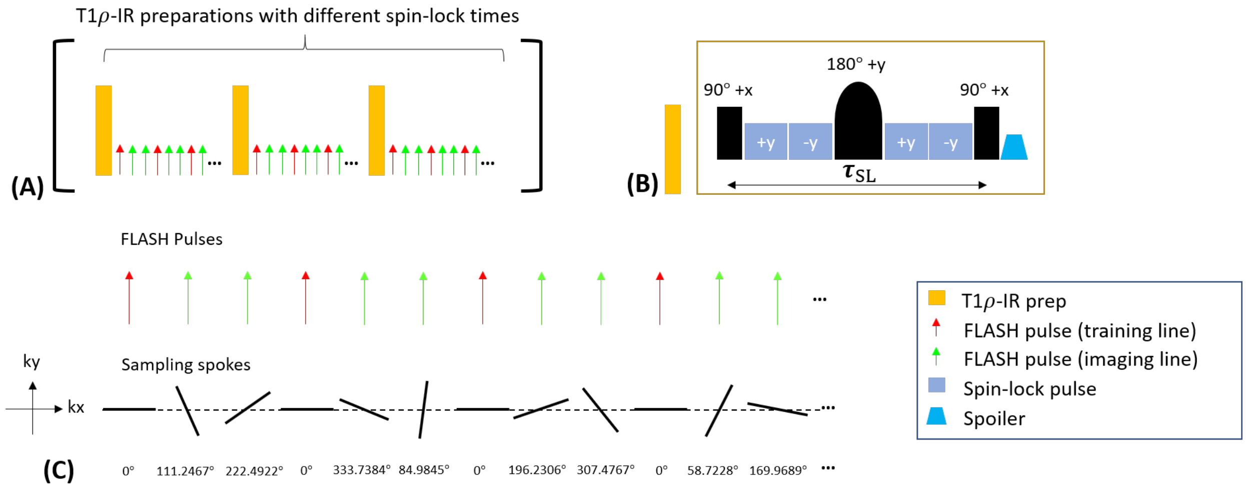

Figure 45. Pulse sequence and data acquisition for myocardial T1/T1ρ mapping. (A) T1ρ-IR preparations with different spin-lock times are cycled through to generate different T1ρ weightings. (B) Specific structure of the paired self-compensated T1ρ-IR preparation. (C) Data acquisition scheme, where the training data are sampled every 3 readouts with a constant 0° spoke, and the imaging data are sampled with a golden angle radial trajectory.

5.2.2.2 Image Model

The underlying image can be represented as a 5-way tensor $\mathcal{X}$ with the first dimension concatenating three spatial dimensions $\mathbf{r} = [x, y, z]$, and four time dimensions indexing T1 relaxation (t_{T1}), T1ρ relaxation ($t_{\mathrm{T1\rho}}$), cardiac phase (t_{c}), and respiratory phase (t_{r}). $\mathcal{X}$ is an LRT due to the strong spatiotemporal correlation along and across each dimension, resulting in the explicit LRT decomposition as:

$$\mathbf{X}_{(1)} = \mathbf{U}\boldsymbol{\Phi}, \tag{5.3}$$

$$\boldsymbol{\Phi} = \mathbf{C}_{(1)}(\mathbf{H} \otimes \mathbf{G} \otimes \mathbf{Z} \otimes \mathbf{V})^{T}, \tag{5.4}$$

where $\mathbf{U}$ is the spatial factor matrix whose columns are the spatial basis functions, $\mathbf{V}$, $\mathbf{Z}$, $\mathbf{G}$, and $\mathbf{H}$ are the temporal factor matrices for the four time dimensions whose columns are the corresponding temporal basis functions. Figure 46 demonstrates multiple time dimensions of the LRT image model for non-ECG, free-breathing myocardial T1 and T1ρ mapping.

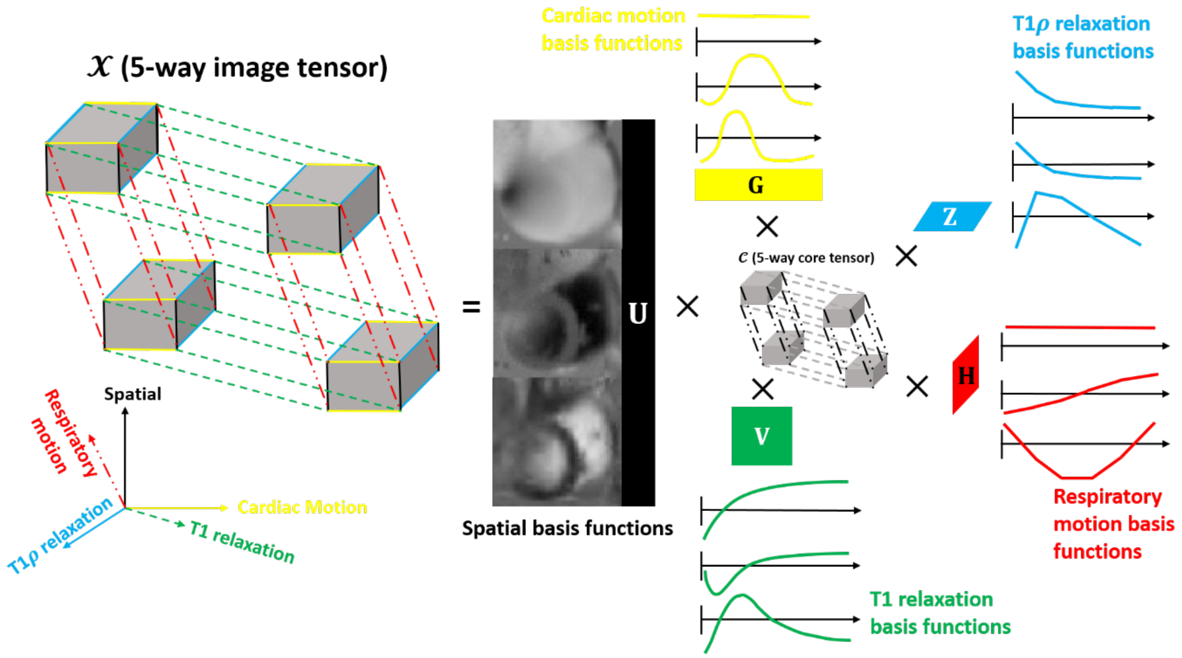

Figure 46. Illustration of multiple temporal dimensions of the 5-way low-rank tensor for myocardial T1/T1ρ mapping. The 5-way image tensor contains spatial, T1 relaxation, T1ρ relaxation, cardiac motion, and respiratory motion dimensions. The low-rank tensor structure can be explicitly expressed through tensor factorization between 5 sets of basis functions assigned to each dimension and the 5-way core tensor governing the interaction between different basis functions. Here only the three most significant basis functions describing each dimension of the tensor are provided.

5.2.2.3 Cardiac and Respiratory Motion Binning

Cardiac and respiratory binning (i.e., determine respiratory positions and cardiac phases) are performed in order to construct the multidimensional tensor. As reported in previous studies[69], we use an unsupervised machine learning approach to automatically cluster cardiac and respiratory motion states. This method employs a modified k-means algorithm incorporating a low-rank relaxation model to correct for the dynamic contrast weightings caused by T1 and T1ρ relaxation. For in vivo experiments, we choose 20 cardiac bins comparable to typical CINE images which allows for functional analysis, and 6 respiratory bins based on a with-in cluster sum of squares analysis[69,70]. Cardiac bins and respiratory bins are set to 1 for phantom experiments.

5.2.2.4 Phantom Study

An ISMRM/NIST phantom (model 130, High Precision Devices, Boulder, Colorado) was scanned on a 3T clinical scanner (Biograph mMR, Siemens Healthineers, Erlangen, Germany) using a 20-channel body coil. A reference T1 map was obtained using an IR-SE sequence with FOV=210x210mm^2, in-plane resolution=1.6x1.6mm^2, slice thickness=5mm, TIs=[21,100,200,400,800,1600,3200]ms. A reference T1□map was obtained using T1ρ-FLASH sequence with FOV=240x240mm^2, in-plane resolution=1.0x1.0mm^2, slice thickness=3.5mm, TSL=[15,23,31,51,91,131,171]ms, spin-lock frequency=500Hz. The Multitasking sequence consisted of 7 T1ρ-IR preparation pulses with TSL=[15,23,31,51,91,131,171]ms and spin-lock frequency=500Hz, and each preparation pulse was followed by 492 FLASH pulses, spanning an inversion recovery period of 2.5s. Other Multitasking parameters were: FOV=240x240mm^2, in-plane resolution=1.5x1.5mm^2, slice thickness=3.5mm, echo spacing=5.0ms, nominal FLASH flip angle=5°, scan time=120s.

5.2.2.5 In vivo Study

The in vivo study was approved by the IRB of our institute. All volunteers gave written informed consent before the study. As a preliminary study, *N*=3 healthy volunteers were recruited and were scanned on the Biograph mMR scanner. For each subject, reference T1 maps of one mid left ventricle slice at two cardiac phases (end-systole and end-diastole) were obtained using a

MOLLI sequence with a 9s breath hold each. MOLLI in-plane resolution=1.4x1.4mm^2, slice thickness=8mm; reference T1ρ maps of the same slice at end-systole and end-diastole phases were obtained using a T1ρ-FLASH sequence with a 7.2s breath hold each. T1ρ-FLASH in-plane resolution=1.9x1.9mm^2, slice thickness=8mm; the Multitasking sequence consisted of 5 T1ρ-IR preparation pulses with TSL=[4.1,18.1,30.1,42.1,58.1]ms and spin-lock frequency=500Hz, and each preparation pulse was followed by 492 FLASH pulses, spanning an inversion recovery period of 2.5s. Other Multitasking parameters were: FOV=270x270mm^2, in-plane resolution=1.7x1.7mm^2, slice thickness=8mm, echo spacing=5ms, nominal FLASH flip angle=5°, scan time=87s.

5.2.2.6 Image Analysis

All the reconstructions were performed on a Linux workstation with a 2.70GHz dual 12-core Intel Xeon processor equipped with 256GB RAM and running MATLAB 2018a (Mathworks, Natick, Massachusetts). The reconstruction time was 30min per subject using a 12GB memory GPU. T1 and T1ρ were obtained by a nonlinear least-squares multiparametric fitting according to Eq. (4.10) with the T2 component removed. For in vivo cases, we picked the end-expiration position and performed the fitting 20 times to obtain cardiac-resolved T1 and T1ρ maps. For phantom study, ROI were drawn for each vial. For in vivo study, T1 and T1ρ maps of end-systole and end-diastole phases were picked out for analysis. The global ROI was drawn for the entire myocardium, while the regional ROI corresponded to the 6 segments according to the American Heart Association's 17-segment model in the mid left ventricular short axis slice (Figure 47).

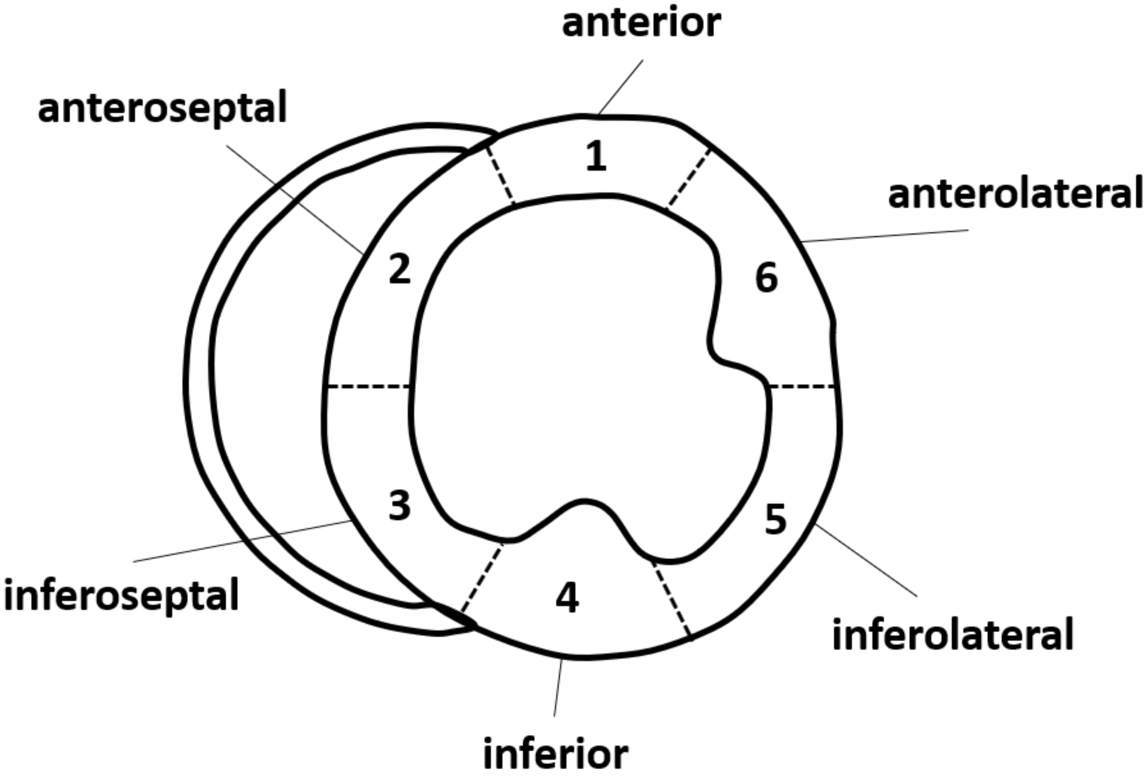

Figure 47. Demonstration of the regional ROI, which is drawn based on the AHA 17-segment model in the mid short-axis slice.

5.2.2.7 Quantitative Analysis

For phantom study, the mean and standard deviation of T1 and T1ρ for each vial were calculated. Linear regression analysis was performed, and ICCs were calculated using IBM SPSS Statistics (Armonk, New York) with a two-way mixed model and 95% confidence level to evaluate the quantitative agreement between Multitasking and the reference methods.

For in vivo study, both global and regional T1 and T1ρ values were calculated and compared between Multitasking and the reference methods for end-systole and end-diastole cardiac phases for each subject.

5.2.3 Results

5.2.3.1 Phantom Study

Figure 48 shows the phantom results. Multitasking T1 and T1ρ maps were comparable with corresponding reference maps. Multitasking T1 and T1ρ measurements were in substantial correlation (R^2=0.999) with reference measurements and demonstrated excellent quantitative agreement (ICC=0.999) with reference measurements.

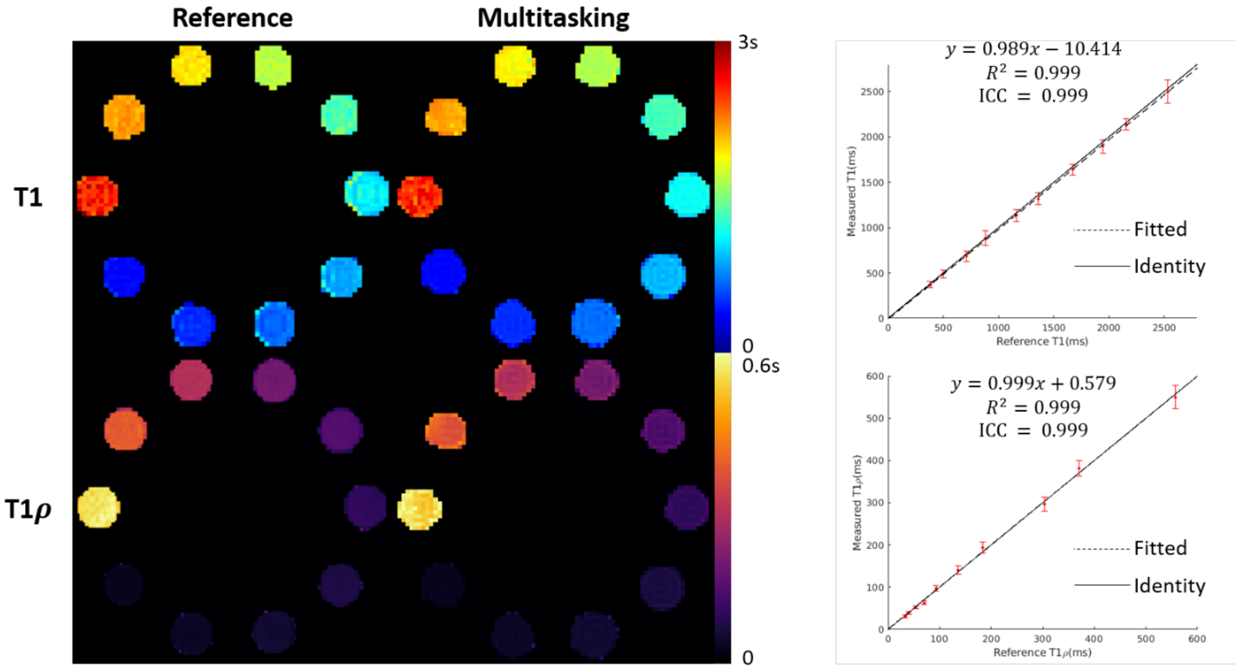

Figure 48. Phantom results. Multitasking produces co-registered T1/T1ρ maps with good image quality. Multitasking T1/T1ρ measurements are in substantial quantitative agreement with reference measurements, as demonstrated by the high R^2 and ICC. The solid line represents identity (y=x) and the dotted line represents linear regression fitting.

5.2.3.2 In vivo Study

Figure 49 illustrates the multidimensional image formulation with respect to each time dimension. When showing image dynamics along one time dimension, the other three time dimensions were at fixed temporal indexes. The temporal evolution for each time dimension was displayed only for the horizontal or vertical profile marked in yellow dash lines. Clear temporal profiles of inversion recovery, T1ρ decay, respiratory motion, and cardiac motion were observed, as demonstrated in Figure 49A – 49D.

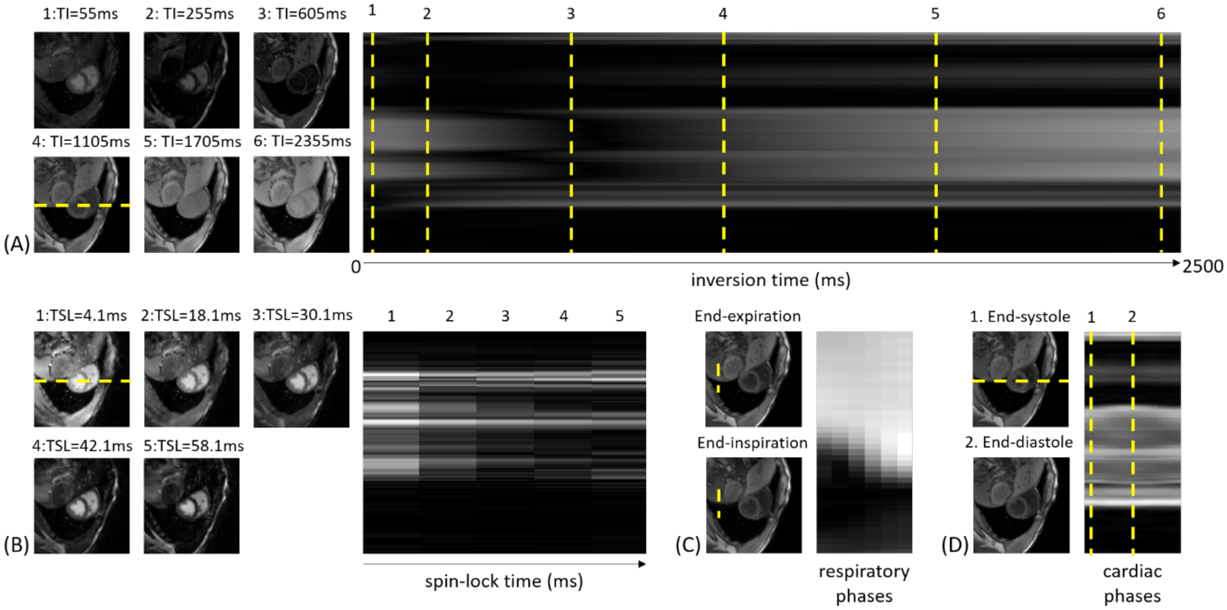

Figure 49. Multidimensional tensor illustration for the myocardial T1/T1ρ mapping. (A) Images at 6 different Tis, as well as the T1 relaxation process of a horizontal profile. (B) Images at 5 different TSLs, as well as the T1ρ relaxation process of a horizontal profile. (C) Images at the end-expiration and end-inspiration positions, as well as the respiratory motion of a vertical profile across the liver. (D) Images at end-systole and end-diastole, as well as the cardiac motion of a horizontal profile.

Figure 50 shows example MOLLI T1 maps and T1ρ-FLASH T1ρ maps at end-systole and end-diastole, as well as cardiac-resolved Multitasking T1 and T1ρ maps at 20 cardiac phases during end-expiration. Multitasking maps were generated with good image quality. Multitasking T1 maps showed elevated T1 values in the blood pool compared to MOLLI T1 maps. Multitasking T1ρ maps were comparable with T1ρ-FLASH T1ρ maps.

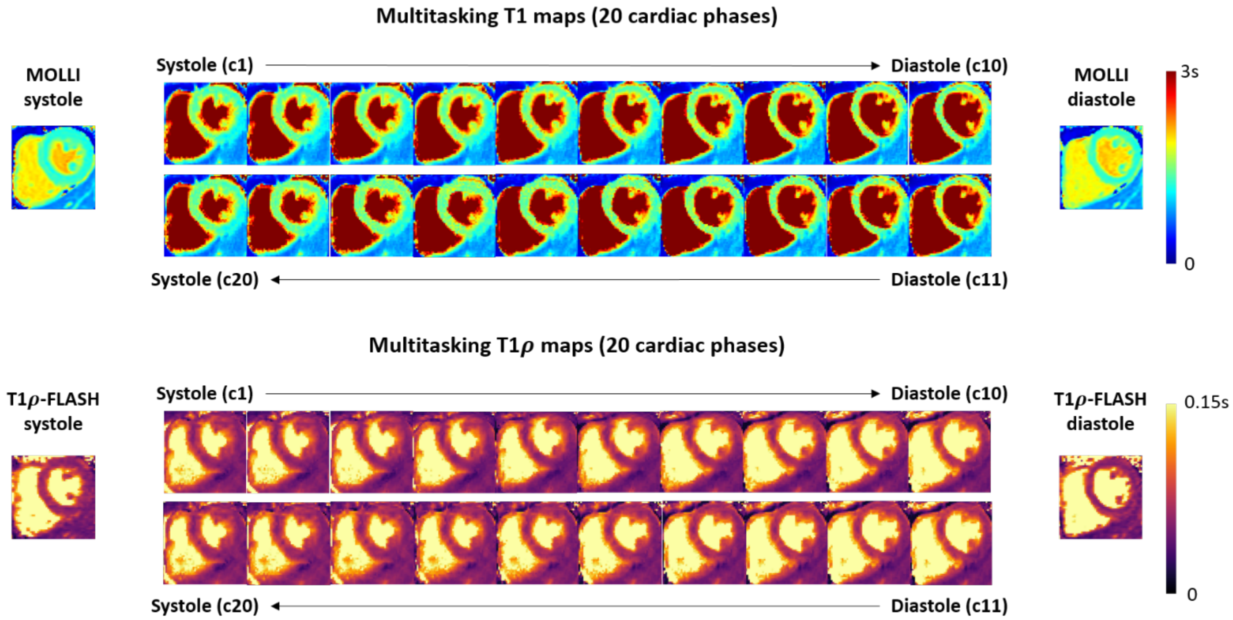

Figure 50. Top: MOLLI T1 maps at end-systole and end-diastole, as well as cardiac-resolved Multitasking T1 maps of 20 cardiac phases. Bottom: T1ρ-FLASH T1ρ maps at end-systole and end-diastole, as well as cardiac-resolved Multitasking T1ρ maps of 20 cardiac phases.

Table 15 shows both global and regional T1 measurement populations of MOLLI and Multitasking. Systole T1 values were 1200.7±42.5ms and 1279.8±30.8ms with MOLLI and Multitasking, respectively. Diastole T1 values were 1205.1±67.3ms and 1300.6±14.6ms with MOLLI and Multitasking, respectively. Table 16 shows both global and regional T1ρ measurement populations of T1ρ-FLASH and Multitasking. Systole T1ρ values were 61.7±4.7ms and 62.0±4.0ms with T1ρ-FLASH and Multitasking, respectively. Diastole T1ρ values were

59.6±6.9ms and 61.8±6.9ms with T1ρ-FLASH and Multitasking, respectively. All T1 and T1ρ measurements were within literature ranges[40,41,69,70,154,185-188].

Table 15. Global and regional MOLLI and Multitasking myocardial T1 values.

MOLLI T1 (ms)	Systole			Diastole		
Global	1200.7±42.5			1205.1±67.3		
Regional	#1: 1160.3±80.9	#2: 1233.2±47.4	#3: 1239.9±29.9	#1: 1175.5±82.5	#2: 1235.7±35.7	#3: 1241.0±30.5
	#4: 1222.6±53.4	#5: 1148.4±56.9	#6: 1177.1±26.1	#4: 1203.2±68.8	#5: 1186.3±77.3	#6: 1167.7±69.6
Multitasking T1 (ms)	**Systole**			**Diastole**		
Global	1279.8±30.8			1300.6±14.6		
Regional	#1: 1252.3±51.0	#2: 1301.7±53.7	#3: 1315.8±83.3	#1: 1259.9±35.9	#2: 1316.3±37.1	#3: 1321.1±65.9
	#4: 1310.6±91.8	#5: 1229.2±50.4	#6: 1242.8±37.4	#4: 1303.3±79.2	#5: 1265.5±39.0	#6: 1285.4±27.3

Table 16. Global and regional T1ρ-FLASH and Multitasking myocardial T1ρ values

T1ρ-FLASH T1ρ (ms)	Systole			Diastole		
Global	61.7±4.7			59.6±6.9		
Regional	#1: 63.6±5.0	#2: 63.9±5.1	#3: 60.6±6.5	#1: 60.3±8.8	#2: 61.9±6.2	#3: 60.3±4.8
	#4: 57.9±6.5	#5: 62.5±3.0	#6: 60.2±6.5	#4: 56.7±6.3	#5: 55.7±4.1	#6: 60.7±7.4
Multitasking T1ρ (ms)	**Systole**			**Diastole**		
Global	62.0±2.0			61.8±6.9		
Regional	#1: 62.2±2.5	#2: 63.0±2.6	#3: 62.7±5.9	#1: 60.6±7.1	#2: 63.6±7.1	#3: 62.5±8.6
	#4: 59.2±4.7	#5: 60.5±5.4	#6: 61.3±3.3	#4: 58.0±8.0	#5: 59.4±6.4	#6: 62.0±6.6

5.2.4 Discussion and Conclusion

In this section, the technique introduced in Chapter 4 was translated to the heart for simultaneous myocardial T1 and T1ρ mapping in a single, continuous acquisition that did not rely on external ECG triggering, breath-holds, or respiratory navigators. Phantom study showed good accuracy of Multitasking T1 and T1ρ maps compared to gold standard IR-SE and T1ρ-FLASH, as well as excellent correlation with the reference maps. Cardiac-resolved Multitasking T1 and T1ρ maps were generated with good image quality. Myocardial T1 and T1ρ measurements were comparable with reference measurements obtained with MOLLI and T1ρ-FLASH respectively.

Commonly adopted T1 mapping techniques in clinical studies, such as MOLLI[41], shortened MOLLI (shMOLLI)[187], saturation recovery single shot acquisition (SASHA)[40], attempt to “freeze” cardiac motion by acquiring one single shot image per cardiac cycle at a fixed cardiac phase targeted by the ECG signal, and mitigate respiratory motion with breath-holds, respiratory navigators or gating methods. Myocardial T1ρ mapping is usually performed in a similar manner. Although free-breathing T1ρ mapping techniques has been proposed with respiratory motion correction or compensation, the use of ECG is still crucial in these studies[154,185,188]. Previously proposed advanced myocardial mapping techniques, such as cardiac MRF, also use ECG to target one cardiac phase in a breath-holding scan[63]. Recently a free-running cardiac MRF technique was proposed using a transient bSSFP acquisition that retrospectively gated the acquired data into multiple cardiac phases[189]. However, it suffered from low temporal resolution (between 125ms to 270 ms for a heartbeat of 60bpm).

The major advantage of the proposed method is the ability to perform cardiac and respiratory motion-resolved quantitative mapping in the heart without “freezing” these physiological motion using devices and techniques such as ECG, breath-holds, and respiratory navigators, which provides a potential avenue for conveniently imaging patients with cardiac arrhythmia and/or difficulties holding their breaths with improved efficiency and success rate. Another advantage of the proposed method is the high temporal resolution. Compared to existing

SR- or IR-based methods that have limited samples along the recovery curve (i.e., 4 samples for 3D-QALAS[186], 11 samples for MOLLI[41]), we have 492 samples equally spaced by 5ms in a 2.5s recovery period. Subspace training data were periodically collected every 3 readouts, resulting in a temporal resolution of 15ms which is higher than conventional CINE functional imaging (~50ms). The cardiac-resolved, CINE-like dynamic myocardial T1 and T1ρ maps with high temporal resolution will be applied for functional analysis in future work.

In vivo Multitasking T1ρ values were comparable to T1ρ-FLASH. However, difference will be expected under a larger sample size primarily due to the difference in the preparation modules (T1ρ-IR in Multitasking vs. T1ρ-prep in T1ρ-FLASH). Multitasking T1 values in the myocardium showed a higher trend compared to MOLLI. While it would require a larger sample size to test the statistical significance, it has been widely reported that MOLLI would lead to T1 underestimation in the myocardium due to T2-dependence, magnetization transfer effect, and the inversion efficiency[190,191]. On the other hand, the spatiotemporal B1+ inhomogeneity in flowing blood may have a confounding influence on Multitasking T1 accuracy of the myocardium. This can be mitigated by introducing a second flip angle that cycles for every inversion recovery period, which aims at B1+-robust T1 mapping[181]. This option will be investigated in future work. On the other hand, Multitasking T1 values in the blood pool were notably higher than MOLLI, which was probably because the 2D acquisition was sensitive to the blood inflow effect which primarily affected the T1 accuracy of the blood. We could extend to 3D acquisition to mitigate this effect and reduce the T1 bias for blood, which will also be explored in future work.

In conclusion, we presented a non-ECG, free-breathing method to simultaneously quantify myocardial T1 and T1ρ using MR Multitasking. Cardiac-resolved, CINE-like myocardial T1 and T1ρ maps were generated with good image quality and high temporal resolution. Functional analysis and the ability for myocardial disease characterization will be investigated in future work. The proposed method provides a potential avenue for imaging patients with arrhythmia and/or difficulties for breath-holds.

Chapter VI Conclusions and Future Innovation

6.1 Dissertation Summary

Quantitative MRI has advantages over conventional qualitative MRI that is currently widely adopted in clinical systems in several aspects: i) quantitative MRI produces meaningful variables with physical units that are more reproducible across sites, vendors, and subjects; ii) quantitative physical variables are more sensitive to subtle alternation of tissues that may indicate the occurrence or progression of diseases; iii) quantitative physical variables can produce higher specificity in terms of disease characterization; iv) quantitative MRI can establish a normal range of tissue parameters on healthy conditions, which provides foundations for disease diagnosis and reveals physiological abnormalities not available on qualitative images; and v) quantitative variables are directly associated with tissue states and can serve as candidate tissue biomarkers for early detection, diagnosis, prognosis, and treatment monitoring. In addition, the quantification of most tissue parameters does not require gadolinium-based contrast agent administration, which better suits patients with renal insufficiency and relieves concern for contrast agent deposition and toxicity. Different quantitative parameters can offer complementary information about tissue properties, and the combination of multiple quantitative parameters allows comprehensive tissue characterization and may improve diagnosis accuracy. However, several technical challenges prevent the wide adaptation of quantitative MRI in clinical practices: i) multiparametric quantification leads to lengthy and impractical scan time which can cause patient discomfort and increase costs; ii) it is difficult to handle patient movement during the scan which can cause image artifacts and loss of diagnostic information; and iii) multiparametric MRI are usually performed in separate acquisitions, which produces misaligned parametric maps that complicate the joint analysis. This dissertation aimed at tacking these technical challenges with a novel quantitative

MRI imaging framework named as Magnetic Resonance Multitasking which incorporates multiple capabilities in a single continuous acquisition, producing co-registered parametric maps while handling potential physiological and physical motion patterns with various solutions. Because MR Multitasking employs an LRT image model that explores multidimensional signal correlations to reduce sampling requirements, it successfully bypasses the curve of dimensionality, allowing efficient acquisition while simplifying clinical workflows. Furthermore, MR Multitasking has intrinsic advantages to handle different kinds of motion–either pseudo-periodic motion (cardiac motion and respiratory motion) or random and discrete motion (bulk motion in the brain)–by capturing them in different time dimensions, making it more suitable in clinical practices when scanning aging patients who are unable to stay still for a long time, or patients with certain physiological abnormalities such as dyspnea, arrhythmia, or Parkinson's disease that may cause irregular or uncontrolled motion.

Chapters 3 introduces a simultaneous T1, T2, ADC mapping approach with MR Multitasking that is applied to the brain. Technical validation was performed, where Multitasking T1, T2, and ADC measurements were comparable and in substantial quantitative agreement with those collected with reference methods where available. Multitasking T1, T2, and ADC maps were co-registered and were all free from image distortion which was conspicuous on DW-SSEPI ADC maps. For this technique, we chose an easy strategy to handle motion, where the motion-corrupted data were simply discarded from the image reconstruction, which improved the quantification accuracy of all three measurements. Clinical feasibility was demonstrated in the brain on post-surgery brain tumor patients where Multitasking T1, T2, and ADC maps reflected tissue characteristics of the recurrent tumor, edema, and non-tumoral WM. Comprehensive clinical validation in the brain will be carried out in the future.

Chapter 4 introduces a simultaneous T1, T2, T1ρ mapping approach with MR Multitasking that is applied to the brain with 3D whole-brain coverage. We demonstrated the in vivo repeatability of this technique, as well as the quantitative agreement between Multitasking and the reference methods. One major technical advancement of this technique is that we have made a fresh attempt for motion-resolved imaging in the brain, where different motion states (i.e., head positions during the scan) are also captured in the LRT image model. By exploiting the correlation not only across contrast-weighting time dimensions but also between different motion states, we were able to recover clean motion-resolved parametric maps no matter the motion occurred as in-plane or through-plane. This strategy offers novel insight and potential to tackle brain motion without reacquisition or data rejection in a clinical scan. Another technical advancement is that synthetic contrast-weighted images that are comparable to clinical images can be generated using the quantitative maps, which has great potential to replace all conventional MRI scans with a single Multitasking scan in the future for disease assessment. The clinical benefit of simultaneous T1, T2, T1ρ mapping has been demonstrated in an RRMS patient cohort, as the combination of three parameters had the best discriminating accuracy between healthy control and MS with significantly higher AUC than using either single parameter alone. This suggested that T1, T2, T1ρ can act as tissue biomarkers in characterizing MS.

Chapter 5 introduces potential applications in other body organs with two preliminary studies. First, we translated the simultaneous T1, T2, and ADC mapping technique to the breast with 3D whole-breast coverage with a clinically acceptable scan time. The notable nonuniform B1+ inhomogeneity across the bilateral breast FOV was addressed with a B1+-compensated multiparametric fitting approach that incorporated prior knowledge of B1+ field information. High quality, co-registered whole-breast T1, T2, and ADC maps were produced with repeatable quantitative measurements that showed substantial agreement with reference measurements. Second, we translated the simultaneous T1, T2, and T1ρ mapping technique to the heart to achieve a non-ECG, free-breathing acquisition of myocardial T1 and T1ρ. The different frequency range of cardiac motion (0.6Hz to 3Hz) and respiratory motion (0.1Hz to 0.5Hz) allows them to be separated and simultaneously captured in two time dimensions in the LRT image model. Unlike the random and discrete head motion pattern, both cardiac and respiratory motion patterns are continuous and pseudo-random, making it more suitable to regularize the temporal continuity. MR Multitasking enables cardiac- and respiratory-resolved T1 and T1ρ mapping with high temporal resolution in a single scan, which not only simplifies the workflow by removing ECG and the set-ups for running multiple separate sequences, but also shows a potential avenue for scanning patients who have difficulties holding their breaths or suffer from cardiac arrhythmias. These ongoing, preliminary studies will be continuously carried out for further technical advancement and clinical validation.

6.2 Potential Avenues for Future Innovation

6.2.1 Whole-Body Non-Contrast Quantitative Tissue Characterization with MR Multitasking

The projects in this dissertation will serve as a stepping stone to the long-term objective of whole-body non-contrast quantitative tissue characterization using MRI, which has significant clinical potential for risk assessment, early detection, diagnosis, outcome prediction, and treatment monitoring in all body organs and structures including head, neck, breast, heart, abdominal organs, prostate, muscles, and spines. MR Multitasking is well-suited for this purpose, as it provides co-registered multiparametric maps for comprehensive assessment of tissue properties with unique abilities to handle motion in an efficient, push-button MR exam. Besides, this framework allows the scan time and data storage memory to scale approximately linearly, making it practical to quantify many parameters all at once with the use of high number of dimensions. The parameters to be quantified will be specifically organ-dependent and will be based on corresponding clinical recommendations. Example architectures of the whole-body quantitative tissue characterization protocols may include:

- Head: T1, T2, T1ρ, ADC, T2*, QSM – 15min;
- Neck (carotid): T1, T2, ADC – 5min;
- Breast: T1, T2, ADC – 6min;
- Heart: T1, T2, T2*, QSM, T1ρ, and separate ADC – 15min;
- Abdomen (liver, pancreas): T1, T2, T1ρ, T2*, PDFF, and separate ADC – 15min;
- Prostate: T1, T2, ADC – 6min;

which add up to 56min for both male subjects (excluding breast) and female subjects (excluding prostate) in terms of whole-body quantitative tissue characterization. All these protocols are available with MR Multitasking, and many of them are under active development[56,69-71,115,192-196]. The scan time estimation is based on the current scan time with reasonable acceleration using techniques that will be introduced in section 7.2.2.

6.2.2 Further Scan Time Reduction with Advanced MRI and Computer Science Techniques

Despite that MR Multitasking employs the LRT image model to accelerate the scan time and reduce the memory usage, for certain applications however, in order to meet the clinical imaging requirements such as whole anatomical coverage and high resolution, the scan time still turns out impractical to be accepted for clinical practices. For example, according to Chapter 5, we can achieve simultaneous T1, T2, T1ρ mapping with spatial resolution 1.0x1.0x3.5mm^3 for whole brain coverage (~140mm) in 9min. If we were to meet the clinical requirements for imaging MS patients, the spatial resolution should be at least 1.0x1.0x1.0mm^3 with even slightly larger coverage (e.g., ~176mm) to include the brain stem because MS lesions are likely to occur throughout the brain and down to the spinal cord. In this case, we are facing a scan time of 9x(176/1.0)/(140/3.5)=39.6min! Even if it can be done in 4.5min for 3.5mm thickness and 140mm coverage, as demonstrated in Figure 35 – Figure 38 in Chapter 4 as a reasonable lower bound, achieving 1mm thickness and 176mm coverage still would take 19.8min. As a result, other technical advancements would be desired to further shorten the scan time.

One possible way to go is to further enforce 2D parallel imaging along phase and partition encoding directions in 3D volumetric imaging. In Multitasking image reconstruction, the sensitivity encoding is mainly used for SNR purposes rather than explicit spatial modeling. However, vast amounts of previous works have demonstrated the effectiveness of parallel imaging in scan time acceleration, provided special sampling patterns are designed to allow the separation of aliased slices by efficiently exploiting the sensitivity variation produced by the receiver coil distribution[197-204]. A good example is demonstrated in 2D CAIPIRINHA for volumetric imaging, where aliasing is controlled by shifting sampling positions along phase or partition encoding directions in a well-directed manner[198]. Following the sampling strategy in 2D CAIPIRINHA, the Multitasking sampling can be adjusted such that the phase and partition encoding directions are still sampled with Gaussian variable density but the sampling positions in k-space can only belong to the CAIPIRINHA-type lattices. It also needs to be ensured that an auto-calibrated center k-space region is densely sampled for the purpose of sensitivity estimation. Such sampling pattern can be retrospectively simulated with our existing datasets, by manually setting all the non-CAIPIRINHA k-space locations to 0. Furthermore, currently we are implementing a constrained blind deconvolution (CBD) algorithm for calculating the sensitivity map, but other methods are also worth investigating, such as ESPIRiT[204], as we would lean towards better sensitivity encoding to resolve aliasing voxels. A preliminary test of the effectiveness of ESPIRiT and CAIPIRINHA is demonstrated in Figure 51, where ESPIRiT reconstruction using data of 7min scan time (Figure 51A) produces T1/T2/T1ρ maps with no visible differences compared to the original reconstruction using data of 9.8min scan time (Figure 51C). Using data of 2.5min scan time, the original reconstruction (Figure 51B) yields notably degraded maps, while ESPIRiT reconstruction maintains relatively good image quality (Figure 51D). What's more exciting, combining ESPIRiT and CAIPIRINHA for image reconstruction allows us to use only a small portion of the data of only 1.5min with acceptable image quality (Figure 51F)!

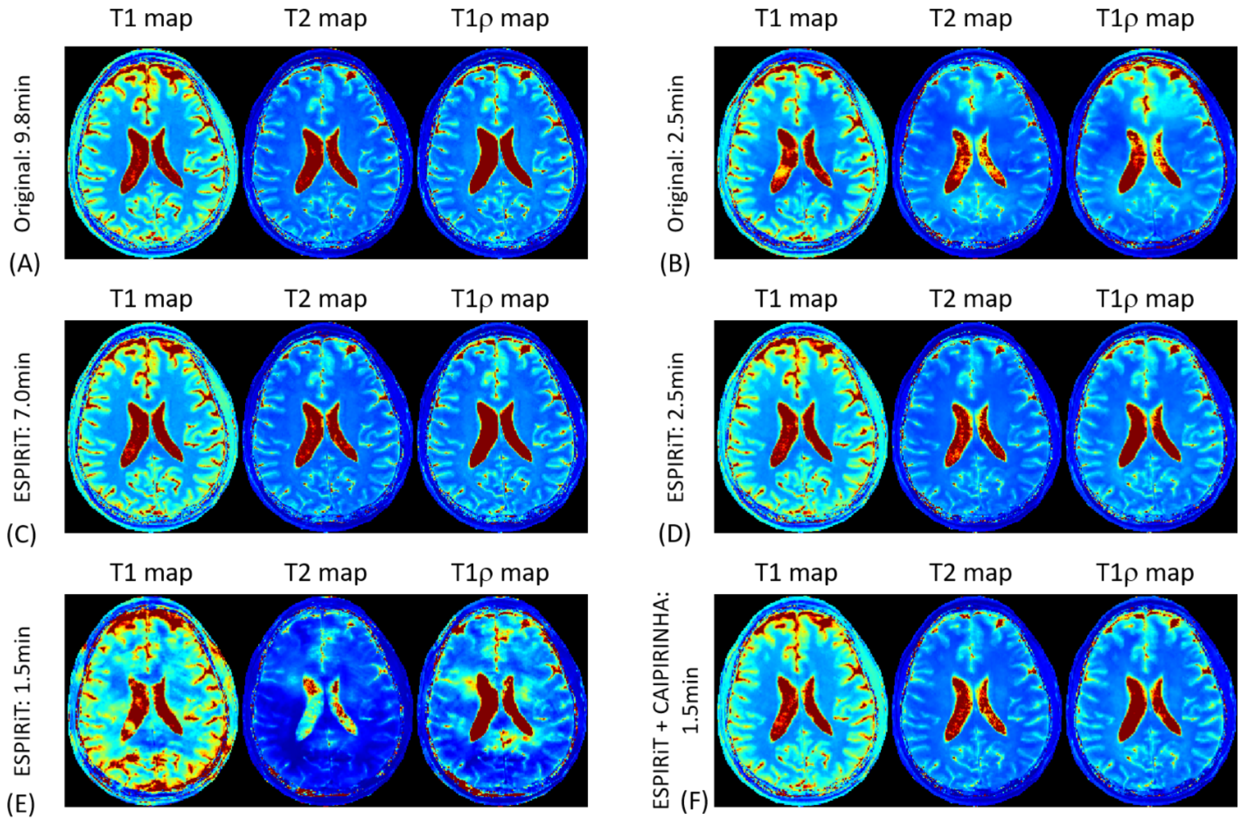

Figure 51. Comparison between the original reconstruction using CBD, ESPIRiT reconstruction, and ESPIRiT reconstruction with retrospective 2D CAIPIRINHA sampling pattern. (A) CBD reconstruction using a 9.8min data. (B) CBD reconstruction using a 2.5min data. (C) ESPIRiT reconstruction using a 7min data. (D) ESPIRiT reconstruction using a 2.5min data. (E) ESPIRiT reconstruction using a 1.5min data. (F) ESPIRiT reconstruction with a retrospective 2D CAIPIRINHA sampling using a 1.5min data.

Another possible approach is deep learning image reconstruction. Consider in general the conventional Multitasking image reconstruction, as described in Eq. (2.14), from the k-space data acquired with a scan (assuming scan time=T) long enough to recover a clean spatial factor matrix (we ignore the spatial regularization function $R_s(\cdot)$ for simplicity):

$$\mathbf{U}_T = \arg\min_{\mathbf{U}} \|\mathbf{d}_T - \Omega(\mathbf{FSU\Phi}_T)]\|^2, \tag{7.1}$$

where $\mathbf{d}_T$ is the k-space data collected with scan time T, and $\mathbf{\Phi}_T$ is the multidimensional temporal factor matrix corresponding to scan time T. The recovered $\mathbf{U}_T$ may be noisy without sparsity regularization, but it should be free from artifacts with enough data to explore the multidimensional correlation. The pulse sequence introduced in Chapters 4 and 5 with interleaved magnetization preparations allow the truncation of the first $1/R$ k-space data which is equivalent to an R-fold prospectively accelerated scan with scan time T/R. Using only this subset of k-space data, the image reconstruction problem is:

$$\mathbf{U}_{T/R} = \arg\min_{\mathbf{U}} \left\| \mathbf{d}_{T/R} - \Omega(\mathbf{FSU\Phi}_{T/R})] \right\|^2, \tag{7.2}$$

where $\mathbf{d}_{T/R}$ is the first $1/R$ k-space data, and $\mathbf{\Phi}_{T/R}$ is the multidimensional temporal factor matrix corresponding to scan time T/R. Because the amount of k-space data is drastically reduced, Eq. (7.2) is thus an undersampled image reconstruction problem, and the resulting $\mathbf{U}_{T/R}$ could be corrupted by extra noise and artifacts. Deep learning image reconstruction techniques are trying to find a mapping function $f\colon \mathbf{U}_{T/R} \to \mathbf{U}_T$ that effectively removes the noise and artifacts to output a high quality spatial factor matrix. Once the network is established, a simple forward pass through the network will suffice. Deep learning undersampled MRI reconstruction with various learning methods and network structures has been widely explored in recent years[205-209]. We plan to implement a multi-level densely connected network (mDCN) that we recently developed for patch-based image-to-image processing[164]. The patch-based nature of this network allows high quality training with fewer images. This network structure reduces the length of network paths and number of weights, which reduces the training time and the amount of training data. To expand the training data size, the 3D datasets that we possess will be broken down in 2D slice by slice, and the network input will be the noisy, artifact-corrupted $\mathbf{U}_{T/R}$ while the network output will be the clean $\mathbf{U}_T$. We also make sure that the 2D slices from the same 3D dataset will either all go on training side or all go on testing side during cross validation.

6.2.3 Comprehensive Motion Handling Solution in Brain MRI

Unlike the continuous, periodical physiological motion patterns such as cardiac motion and respiratory motion in the heart and abdomen region that can be addressed with motion-freezing mechanisms, head motion usually happens in a random, abrupt, and uncontrolled manner which almost solely relies on reacquisition in routine clinical practices. In Chapters 3 and 4, we have introduced two potential solutions – motion-removed imaging and motion-resolved imaging – to handle different types of motion in brain MRI. In future works, we will aim at developing a comprehensive solution to automatically handle various types of head motion. For example, a possible motion handling streamline would consist of three stages: i) abrupt motion detection, where the sudden, abrupt motion (e.g., itching, coughing, sudden tremoring) can be automatically detected from the single-time temporal basis functions as abnormal peaks and spikes[72]; ii) motion states identification, where the shaking and/or nodding patterns involving a large shift of the volume position that creates different motion states are automatically identified according the algorithms proposed in Chapter 4; and iii) motion registration, where different motion states are registered to a single target motion state to increase the correlation between different states, which further facilitates the low-rankness of the image tensor[73]. With the different potential strategies provided by the Multitasking framework, we anticipate a comprehensive solution to address the motion issue in future brain MRI.

6.2.4 One-For-All: Replacing Conventional Clinical MRI Scans with a Single Quantitative Protocol

In Chapter 4, we have demonstrated that some commonly used qualitative contrast-weighted images for clinical practices could be generated with the quantitative parameter maps. Moreover, other novel image contrasts could also be synthesized which may have the potential to provide better visualization of the tissue abnormalities compared to existing image contrasts, thus improving the diagnostic utility for better image-guided patient care. With various quantitative parameters (e.g., T1, T2, T1ρ, T2*, QSM, ADC, etc.) that could potentially be quantified all in one scan, not only could all the conventional qualitative images (i.e., T1w, T2w, PDw, FLAIR, DIR, SWI, DWI, etc.) be generated offline, but it also allows the adjustment of the tissue contrast for each image by manually selecting the sequence parameters (i.e., TR, TE, TI, b-value, etc.) that are used to create the images, providing significant flexibility for the clinicians to adjust the image contrast for better visualization, assessment, and decision-making. Therefore, comprehensive clinical diagnosis and evaluation could possibly be achieved with only a single quantitative protocol. To achieve this goal, our future work will focus on specializing potential patient cohorts (e.g., brain tumor, MS, or Parkinson's disease) and validate the diagnostic utility of the synthetic images against current clinical images.

6.3 Peek into The Future

It has been nearly 40 years since the notion of quantitative MRI was first introduced to medical practices that used NMR relaxation times to differentiate tissue states around mid-1980s. With the radical technological advancement of hardware and software in recent years, it has come to an exciting era when this powerful tool can be finally brought into routine clinical use to aid diagnosis and improve patient care. The invention of MR Multitasking has successfully tackled many technical challenges that have been troubled scientists and physicians for years, paving a bright avenue for the simultaneous acquisition of multiple quantitative tissue parameters in a single push-button MRI exam. In the near future, it can be expected that these quantitative parameters are available for clinicians to achieve comprehensive tissue assessment and whole-body quantitative screening, and can be used to replace all the conventional MRI scans with a single quantitative protocol, thus fundamentally improving the clinical management and patient outcome with better diagnostic decision-making, as well as greatly reducing the scan time and imaging costs. In the meantime, technicians can look forward to eventually being relieved from complex workflows in regular MRI exams with minimal interactions with the MRI scanner.

BIBLIOGRAPHY

1. Pierpaoli C. Quantitative brain MRI. *Top Magn Reson Imaging.* 2010;21(2):63.
2. Akella SV, Regatte RR, Wheaton AJ, Borthakur A, Reddy R. Reduction of residual dipolar interaction in cartilage by spin-lock technique. *Magn Reson Med.* 2004;52(5):1103-1109.
3. Inglese M, Ge Y. Quantitative MRI: hidden age-related changes in brain tissue. *Top Magn Reson Imaging.* 2004;15(6):355-363.
4. Singh P, Kaur R, Saggar K, Singh G, Kaur A. Qualitative and quantitative hippocampal MRI assessments in intractable epilepsy. *Biomed Res Int.* 2013;2013:480524.
5. Korzdorfer G, Kirsch R, Liu K, Pfeuffer J, Hensel B, Jiang Y, et al. Reproducibility and Repeatability of MR Fingerprinting Relaxometry in the Human Brain. *Radiology.* 2019;292(2):429-437.
6. Metere R, Kober T, Moller HE, Schafer A. Simultaneous Quantitative MRI Mapping of T1, T2* and Magnetic Susceptibility with Multi-Echo MP2RAGE. *PLoS One.* 2017;12(1):e0169265.
7. Xiao YD, Paudel R, Liu J, Ma C, Zhang ZS, Zhou SK. MRI contrast agents: Classification and application (Review). *Int J Mol Med.* 2016;38(5):1319-1326.
8. Carr DH, Brown J, Bydder GM, Weinmann HJ, Speck U, Thomas DJ, et al. Intravenous chelated gadolinium as a contrast agent in NMR imaging of cerebral tumours. *Lancet.* 1984;1(8375):484-486.
9. Tang JB, Sheng YQ, Hu HJ, Shen YQ. Macromolecular MRI contrast agents: Structures, properties and applications. *Prog Polym Sci.* 2013;38(3-4):462-502.
10. Geith T, Schmidt G, Biffar A, Dietrich O, Durr HR, Reiser M, et al. Comparison of qualitative and quantitative evaluation of diffusion-weighted MRI and chemical-shift imaging in the differentiation of benign and malignant vertebral body fractures. *AJR Am J Roentgenol.* 2012;199(5):1083-1092.

11. Law M, Yang S, Wang H, Babb JS, Johnson G, Cha S, et al. Glioma grading: sensitivity, specificity, and predictive values of perfusion MR imaging and proton MR spectroscopic imaging compared with conventional MR imaging. *AJNR Am J Neuroradiol.* 2003;24(10):1989-1998.
12. Grobner T. Gadolinium--a specific trigger for the development of nephrogenic fibrosing dermopathy and nephrogenic systemic fibrosis? *Nephrol Dial Transplant.* 2006;21(4):1104-1108.
13. Darrah TH, Prutsman-Pfeiffer JJ, Poreda RJ, Ellen Campbell M, Hauschka PV, Hannigan RE. Incorporation of excess gadolinium into human bone from medical contrast agents. *Metallomics.* 2009;1(6):479-488.
14. McDonald RJ, McDonald JS, Kallmes DF, Jentoft ME, Murray DL, Thielen KR, et al. Intracranial Gadolinium Deposition after Contrast-enhanced MR Imaging. *Radiology.* 2015;275(3):772-782.
15. Ramalho J, Semelka RC, Ramalho M, Nunes RH, AlObaidy M, Castillo M. Gadolinium-Based Contrast Agent Accumulation and Toxicity: An Update. *AJNR Am J Neuroradiol.* 2016;37(7):1192-1198.
16. Rogosnitzky M, Branch S. Gadolinium-based contrast agent toxicity: a review of known and proposed mechanisms. *Biometals.* 2016;29(3):365-376.
17. Gadolinium Toxicity: A Survey of the Chronic Effects of Retained Gadolinium from Contrast MRIs. https://gdtoxicity.files.wordpress.com/2014/09/gd-symptom-survey.pdf. 2015.
18. Kim PK, Hong YJ, Im DJ, Suh YJ, Park CH, Kim JY, et al. Myocardial T1 and T2 Mapping: Techniques and Clinical Applications. *Korean J Radiol.* 2017;18(1):113-131.
19. Messroghli DR, Moon JC, Ferreira VM, Grosse-Wortmann L, He T, Kellman P, et al. Clinical recommendations for cardiovascular magnetic resonance mapping of T1, T2, T2* and extracellular volume: A consensus statement by the Society for Cardiovascular Magnetic Resonance (SCMR) endorsed by the European Association for Cardiovascular Imaging (EACVI). *J Cardiovasc Magn Reson.* 2017;19(1):75.

20. Radenkovic D, Weingartner S, Ricketts L, Moon JC, Captur G. T1 mapping in cardiac MRI. *Heart Fail Rev.* 2017;22(4):415-430.

21. Barentsz JO, Weinreb JC, Verma S, Thoeny HC, Tempany CM, Shtern F, et al. Synopsis of the PI-RADS v2 Guidelines for Multiparametric Prostate Magnetic Resonance Imaging and Recommendations for Use. *Eur Urol.* 2016;69(1):41-49.

22. Barral M, Taouli B, Guiu B, Koh DM, Luciani A, Manfredi R, et al. Diffusion-weighted MR imaging of the pancreas: current status and recommendations. *Radiology.* 2015;274(1):45-63.

23. Maier SE, Sun Y, Mulkern RV. Diffusion imaging of brain tumors. *NMR Biomed.* 2010;23(7):849-864.

24. Partridge SC, McDonald ES. Diffusion weighted magnetic resonance imaging of the breast: protocol optimization, interpretation, and clinical applications. *Magn Reson Imaging Clin N Am.* 2013;21(3):601-624.

25. Yamasaki F, Kurisu K, Satoh K, Arita K, Sugiyama K, Ohtaki M, et al. Apparent diffusion coefficient of human brain tumors at MR imaging. *Radiology.* 2005;235(3):985-991.

26. Hattingen E, Jurcoane A, Daneshvar K, Pilatus U, Mittelbronn M, Steinbach JP, et al. Quantitative T2 mapping of recurrent glioblastoma under bevacizumab improves monitoring for non-enhancing tumor progression and predicts overall survival. *Neuro Oncol.* 2013;15(10):1395-1404.

27. Lescher S, Jurcoane A, Veit A, Bahr O, Deichmann R, Hattingen E. Quantitative T1 and T2 mapping in recurrent glioblastomas under bevacizumab: earlier detection of tumor progression compared to conventional MRI. *Neuroradiology.* 2015;57(1):11-20.

28. Badve C, Yu A, Dastmalchian S, Rogers M, Ma D, Jiang Y, et al. MR Fingerprinting of Adult Brain Tumors: Initial Experience. *AJNR Am J Neuroradiol.* 2017;38(3):492-499.

29. Wang L, Gaddam S, Wang N, Xie Y, Deng Z, Zhou Z, et al. Multiparametric Mapping Magnetic Resonance Imaging of Pancreatic Disease. *Front Physiol.* 2020;11:8.

30. Yu AC, Badve C, Ponsky LE, Pahwa S, Dastmalchian S, Rogers M, et al. Development of a Combined MR Fingerprinting and Diffusion Examination for Prostate Cancer. *Radiology.* 2017;283(3):729-738.

31. Banerjee R, Pavlides M, Tunnicliffe EM, Piechnik SK, Sarania N, Philips R, et al. Multiparametric magnetic resonance for the non-invasive diagnosis of liver disease. *J Hepatol.* 2014;60(1):69-77.

32. McDonald N, Eddowes PJ, Hodson J, Semple SIK, Davies NP, Kelly CJ, et al. Multiparametric magnetic resonance imaging for quantitation of liver disease: a two-centre cross-sectional observational study. *Sci Rep.* 2018;8(1):9189.

33. Reeder SB, Sirlin CB. Quantification of liver fat with magnetic resonance imaging. *Magn Reson Imaging Clin N Am.* 2010;18(3):337-357, ix.

34. Bonnier G, Roche A, Romascano D, Simioni S, Meskaldji D, Rotzinger D, et al. Advanced MRI unravels the nature of tissue alterations in early multiple sclerosis. *Ann Clin Transl Neurol.* 2014;1(6):423-432.

35. Gonyea JV, Watts R, Applebee A, Andrews T, Hipko S, Nickerson JP, et al. In vivo quantitative whole-brain T1 rho MRI of multiple sclerosis. *J Magn Reson Imaging.* 2015;42(6):1623-1630.

36. Chen Y, Panda A, Pahwa S, Hamilton JI, Dastmalchian S, McGivney DF, et al. Three-dimensional MR Fingerprinting for Quantitative Breast Imaging. *Radiology.* 2019;290(1):33-40.

37. Haaf P, Garg P, Messroghli DR, Broadbent DA, Greenwood JP, Plein S. Cardiac T1 Mapping and Extracellular Volume (ECV) in clinical practice: a comprehensive review. *J Cardiovasc Magn Reson.* 2016;18(1):89.

38. Thompson RB, Chow K, Khan A, Chan A, Shanks M, Paterson I, et al. T(1) mapping with cardiovascular MRI is highly sensitive for Fabry disease independent of hypertrophy and sex. *Circ Cardiovasc Imaging.* 2013;6(5):637-645.

39. Bloch F. The Principle of Nuclear Induction. *Science.* 1953;118(3068):425-430.

40. Chow K, Flewitt JA, Green JD, Pagano JJ, Friedrich MG, Thompson RB. Saturation recovery single-shot acquisition (SASHA) for myocardial T(1) mapping. *Magn Reson Med.* 2014;71(6):2082-2095.

41. Messroghli DR, Radjenovic A, Kozerke S, Higgins DM, Sivananthan MU, Ridgway JP. Modified Look-Locker inversion recovery (MOLLI) for high-resolution T1 mapping of the heart. *Magn Reson Med.* 2004;52(1):141-146.

42. Zhu DC, Penn RD. Full-brain T1 mapping through inversion recovery fast spin echo imaging with time-efficient slice ordering. *Magn Reson Med.* 2005;54(3):725-731.

43. Giri S, Chung YC, Merchant A, Mihai G, Rajagopalan S, Raman SV, et al. T2 quantification for improved detection of myocardial edema. *J Cardiovasc Magn Reson.* 2009;11:56.

44. Noth U, Shrestha M, Schure JR, Deichmann R. Quantitative in vivo T2 mapping using fast spin echo techniques - A linear correction procedure. *Neuroimage.* 2017;157:476-485.

45. Chavhan GB, Babyn PS, Thomas B, Shroff MM, Haacke EM. Principles, techniques, and applications of T2*-based MR imaging and its special applications. *Radiographics.* 2009;29(5):1433-1449.

46. Deistung A, Schweser F, Reichenbach JR. Overview of quantitative susceptibility mapping. *NMR Biomed.* 2017;30(4).

47. Liu W, Soderlund K, Senseney JS, Joy D, Yeh PH, Ollinger J, et al. Imaging Cerebral Microhemorrhages in Military Service Members with Chronic Traumatic Brain Injury. *Radiology.* 2016;278(2):536-545.

48. Deistung A, Schweser F, Wiestler B, Abello M, Roethke M, Sahm F, et al. Quantitative susceptibility mapping differentiates between blood depositions and calcifications in patients with glioblastoma. *PLoS One.* 2013;8(3):e57924.

49. Acosta-Cabronero J, Williams GB, Cardenas-Blanco A, Arnold RJ, Lupson V, Nestor PJ. In vivo quantitative susceptibility mapping (QSM) in Alzheimer's disease. *PLoS One.* 2013;8(11):e81093.

50. Chen W, Gauthier SA, Gupta A, Comunale J, Liu T, Wang S, et al. Quantitative susceptibility mapping of multiple sclerosis lesions at various ages. *Radiology.* 2014;271(1):183-192.

51. Wang YX, Zhang Q, Li X, Chen W, Ahuja A, Yuan J. T1rho magnetic resonance: basic physics principles and applications in knee and intervertebral disc imaging. *Quant Imaging Med Surg.* 2015;5(6):858-885.

52. Hagmann P, Jonasson L, Maeder P, Thiran JP, Wedeen VJ, Meuli R. Understanding diffusion MR imaging techniques: from scalar diffusion-weighted imaging to diffusion tensor imaging and beyond. *Radiographics.* 2006;26 Suppl 1:S205-223.

53. Bammer R, Keeling SL, Augustin M, Pruessmann KP, Wolf R, Stollberger R, et al. Improved diffusion-weighted single-shot echo-planar imaging (EPI) in stroke using sensitivity encoding (SENSE). *Magn Reson Med.* 2001;46(3):548-554.

54. Porter DA, Heidemann RM. High resolution diffusion-weighted imaging using readout-segmented echo-planar imaging, parallel imaging and a two-dimensional navigator-based reacquisition. *Magn Reson Med.* 2009;62(2):468-475.

55. Nguyen C, Fan Z, Sharif B, He Y, Dharmakumar R, Berman DS, et al. In vivo three-dimensional high resolution cardiac diffusion-weighted MRI: a motion compensated diffusion-prepared balanced steady-state free precession approach. *Magn Reson Med.* 2014;72(5):1257-1267.

56. Nguyen C, Fan Z, Xie Y, Pang J, Speier P, Bi X, et al. In vivo diffusion-tensor MRI of the human heart on a 3 tesla clinical scanner: An optimized second order (M2) motion compensated diffusion-preparation approach. *Magn Reson Med.* 2016;76(5):1354-1363.

57. Serai SD, Dillman JR, Trout AT. Proton Density Fat Fraction Measurements at 1.5- and 3-T Hepatic MR Imaging: Same-Day Agreement among Readers and across Two Imager Manufacturers. *Radiology.* 2017;284(1):244-254.

58. Deoni SC, Rutt BK, Peters TM. Rapid combined T1 and T2 mapping using gradient recalled acquisition in the steady state. *Magn Reson Med.* 2003;49(3):515-526.

59. Li X, Wyatt C, Rivoire J, Han E, Chen W, Schooler J, et al. Simultaneous acquisition of T1rho and T2 quantification in knee cartilage: repeatability and diurnal variation. *J Magn Reson Imaging.* 2014;39(5):1287-1293.

60. Zhang Y, Wells SA, Hernando D. Stimulated echo based mapping (STEM) of T1 , T2 , and apparent diffusion coefficient: validation and protocol optimization. *Magn Reson Med.* 2018.

61. Marty B, Baudin PY, Reyngoudt H, Azzabou N, Araujo EC, Carlier PG, et al. Simultaneous muscle water T2 and fat fraction mapping using transverse relaxometry with stimulated echo compensation. *NMR Biomed.* 2016;29(4):431-443.

62. Ma D, Gulani V, Seiberlich N, Liu K, Sunshine JL, Duerk JL, et al. Magnetic resonance fingerprinting. *Nature.* 2013;495(7440):187-192.

63. Hamilton JI, Jiang Y, Chen Y, Ma D, Lo WC, Griswold M, et al. MR fingerprinting for rapid quantification of myocardial T1 , T2 , and proton spin density. *Magn Reson Med.* 2017;77(4):1446-1458.

64. Liu Y, Hamilton J, Rajagopalan S, Seiberlich N. Cardiac Magnetic Resonance Fingerprinting: Technical Overview and Initial Results. *JACC Cardiovasc Imaging.* 2018;11(12):1837-1853.

65. Chen Y, Jiang Y, Pahwa S, Ma D, Lu L, Twieg MD, et al. MR Fingerprinting for Rapid Quantitative Abdominal Imaging. *Radiology.* 2016;279(1):278-286.

66. Cruz G, Jaubert O, Schneider T, Botnar RM, Prieto C. Rigid motion-corrected magnetic resonance fingerprinting. *Magn Reson Med.* 2019;81(2):947-961.

67. Mehta BB, Ma D, Pierre EY, Jiang Y, Coppo S, Griswold MA. Image reconstruction algorithm for motion insensitive MR Fingerprinting (MRF): MORF. *Magn Reson Med.* 2018;80(6):2485-2500.

68. Yu Z, Zhao T, Asslander J, Lattanzi R, Sodickson DK, Cloos MA. Exploring the sensitivity of magnetic resonance fingerprinting to motion. *Magn Reson Imaging.* 2018;54:241-248.

69. Christodoulou AG, Shaw JL, Nguyen C, Yang Q, Xie YB, Wang N, et al. Magnetic resonance multitasking for motion-resolved quantitative cardiovascular imaging. *Nat Biomed Eng.* 2018;2(4):215-226.

70. Shaw JL, Yang Q, Zhou Z, Deng Z, Nguyen C, Li D, et al. Free-breathing, non-ECG, continuous myocardial T1 mapping with cardiovascular magnetic resonance multitasking. *Magn Reson Med.* 2019;81(4):2450-2463.

71. Ma S, Nguyen CT, Han F, Wang N, Deng Z, Binesh N, et al. Three-dimensional simultaneous brain T1 , T2 , and ADC mapping with MR Multitasking. *Magn Reson Med.* 2020;84(1):72-88.

72. Wang N, Christodoulou AG, Xie Y, Wang Z, Deng Z, Zhou B, et al. Quantitative 3D dynamic contrast-enhanced (DCE) MR imaging of carotid vessel wall by fast T1 mapping using Multitasking. *Magn Reson Med.* 2019;81(4):2302-2314.

73. Wang N, Gaddam S, Wang L, Xie Y, Fan Z, Yang W, et al. Six-dimensional quantitative DCE MR Multitasking of the entire abdomen: Method and application to pancreatic ductal adenocarcinoma. *Magn Reson Med.* 2020.

74. Liang Z-P. Spatiotemporal imaging with partially separable functions. *In Proceedings of the 4th IEEE International Symposium on Biomedical Imaging: From Nano to Macro*, Arlington, Virginia, USA, 2007. p. 988-991.

75. He J, Liu Q, Christodoulou A, Ma C, Lam F, Liang Z-P. Accelerated high-dimensional MR imaging with sparse sampling using low-rank tensors. *IEEE Trans Med Imaging.* 2016;35(9):2119-2129.

76. Tucker LR. Some mathematical notes on three-mode factor analysis. *Psychometrika.* 1966;31(3):279-311.

77. Kolda TG, Bader BW. Tensor Decompositions and Applications. *Siam Rev.* 2009;51(3):455-500.

78. De Lathauwer L, De Moor B, Vandewalle J. A multilinear singular value decomposition. *Siam J Matrix Anal A.* 2000;21(4):1253-1278.

79. Ellingson BM, Lai A, Nguyen HN, Nghiemphu PL, Pope WB, Cloughesy TF. Quantification of Nonenhancing Tumor Burden in Gliomas Using Effective T2 Maps Derived from Dual-Echo Turbo Spin-Echo MRI. *Clin Cancer Res.* 2015;21(19):4373-4383.

80. Muller A, Jurcoane A, Kebir S, Ditter P, Schrader F, Herrlinger U, et al. Quantitative T1-mapping detects cloudy-enhancing tumor compartments predicting outcome of patients with glioblastoma. *Cancer Med.* 2017;6(1):89-99.

81. Maier SE, Bogner P, Bajzik G, Mamata H, Mamata Y, Repa I, et al. Normal brain and brain tumor: multicomponent apparent diffusion coefficient line scan imaging. *Radiology.* 2001;219(3):842-849.

82. Higano S, Yun X, Kumabe T, Watanabe M, Mugikura S, Umetsu A, et al. Malignant astrocytic tumors: clinical importance of apparent diffusion coefficient in prediction of grade and prognosis. *Radiology.* 2006;241(3):839-846.

83. Murakami R, Hirai T, Sugahara T, Fukuoka H, Toya R, Nishimura S, et al. Grading astrocytic tumors by using apparent diffusion coefficient parameters: superiority of a one- versus two-parameter pilot method. *Radiology.* 2009;251(3):838-845.

84. Gras V, Farrher E, Grinberg F, Shah NJ. Diffusion-weighted DESS protocol optimization for simultaneous mapping of the mean diffusivity, proton density and relaxation times at 3 Tesla. *Magn Reson Med.* 2017;78(1):130-141.

85. Jiang Y, Hamilton J, Lo W. Simultaneous T1, T2 and diffusion quantification using multiple contrast prepared magnetic resonance fingerprinting. *In Proceedings of the 25th Annual Meeting of ISMRM*, Honolulu, HI, 2017. p. 1171.

86. Hutter J, Slator PJ, Christiaens D, Teixeira R, Roberts T, Jackson L, et al. Integrated and efficient diffusion-relaxometry using ZEBRA. *Sci Rep.* 2018;8(1):15138.

87. Gao H, Li L, Zhang K, Zhou W, Hu X. PCLR: phase-constrained low-rank model for compressive diffusion-weighted MRI. *Magn Reson Med.* 2014;72(5):1330-1341.

88. Ma S, Nguyen CT, Christodoulou AG, Luthringer D, Kobashigawa J, Lee SE, et al. Accelerated Cardiac Diffusion Tensor Imaging Using Joint Low-Rank and Sparsity Constraints. *IEEE Trans Biomed Eng.* 2018;65(10):2219-2230.

89. Gao Y, Han F, Zhou Z, Zhong X, Bi X, Neylon J, et al. Multishot diffusion-prepared magnitude-stabilized balanced steady-state free precession sequence for distortion-free diffusion imaging. *Magn Reson Med.* 2019;81(4):2374-2384.

90. Van AT, Cervantes B, Kooijman H, Karampinos DC. Analysis of phase error effects in multishot diffusion-prepared turbo spin echo imaging. *Quant Imaging Med Surg.* 2017;7(2):238-250.

91. Parrish T, Hu X. A new T2 preparation technique for ultrafast gradient-echo sequence. *Magn Reson Med.* 1994;32(5):652-657.

92. Huang C, Graff CG, Clarkson EW, Bilgin A, Altbach MI. T2 mapping from highly undersampled data by reconstruction of principal component coefficient maps using compressed sensing. *Magn Reson Med.* 2012;67(5):1355-1366.

93. McGivney DF, Pierre E, Ma D, Jiang Y, Saybasili H, Gulani V, et al. SVD Compression for Magnetic Resonance Fingerprinting in the Time Domain. *IEEE Trans Med Imaging.* 2014;33(12):2311-2322.

94. Zhao B, Setsompop K, Adalsteinsson E, Gagoski B, Ye H, Ma D, et al. Improved magnetic resonance fingerprinting reconstruction with low-rank and subspace modeling. *Magn Reson Med.* 2018;79(2):933-942.

95. Zhao B, Haldar JP, Christodoulou AG, Liang Z-P. Image Reconstruction From Highly Undersampled (k,t)-Space Data With Joint Partial Separability and Sparsity Constraints. *IEEE Trans Med Imaging.* 2012;31(9):1809-1820.

96. Tamir JI, Uecker M, Chen W, Lai P, Alley MT, Vasanawala SS, et al. T2 shuffling: Sharp, multicontrast, volumetric fast spin-echo imaging. *Magn Reson Med.* 2017;77(1):180-195.

97. Morozov VA. On the solution of functional equations by the method of regularization. *Soviet Math Dokl*. 1966; 7:414-417.

98. Wansapura JP, Holland SK, Dunn RS, Ball WS, Jr. NMR relaxation times in the human brain at 3.0 tesla. *J Magn Reson Imaging.* 1999;9(4):531-538.

99. Helenius J, Soinne L, Perkio J, Salonen O, Kangasmaki A, Kaste M, et al. Diffusion-weighted MR imaging in normal human brains in various age groups. *AJNR Am J Neuroradiol.* 2002;23(2):194-199.

100. Sener RN. Diffusion MRI: apparent diffusion coefficient (ADC) values in the normal brain and a classification of brain disorders based on ADC values. *Comput Med Imaging Graph.* 2001;25(4):299-326.

101. Stanisz GJ, Odrobina EE, Pun J, Escaravage M, Graham SJ, Bronskill MJ, et al. T1, T2 relaxation and magnetization transfer in tissue at 3T. *Magn Reson Med.* 2005;54(3):507-512.

102. Cicchetti DV. Guidelines, criteria, and rules of thumb for evaluating normed and standardized assessment instruments in psychology. *Psychological assessment.* 1994;6(4):284.

103. Jiang Y, Ma D, Keenan KE, Stupic KF, Gulani V, Griswold MA. Repeatability of magnetic resonance fingerprinting T1 and T2 estimates assessed using the ISMRM/NIST MRI system phantom. *Magn Reson Med.* 2017;78(4):1452-1457.

104. Miller KL, Pauly JM. Nonlinear phase correction for navigated diffusion imaging. *Magn Reson Med.* 2003;50(2):343-353.

105. O'Halloran RL, Holdsworth S, Aksoy M, Bammer R. Model for the correction of motion-induced phase errors in multishot diffusion-weighted-MRI of the head: are cardiac-motion-induced phase errors reproducible from beat-to-beat? *Magn Reson Med.* 2012;68(2):430-440.

106. Skare S, Andersson JL. On the effects of gating in diffusion imaging of the brain using single shot EPI. *Magn Reson Imaging.* 2001;19(8):1125-1128.

107. Jeong HK, Gore JC, Anderson AW. High-resolution human diffusion tensor imaging using 2-D navigated multishot SENSE EPI at 7 T. *Magn Reson Med.* 2013;69(3):793-802.

108. Liu C, Bammer R, Kim DH, Moseley ME. Self-navigated interleaved spiral (SNAILS): application to high-resolution diffusion tensor imaging. *Magn Reson Med.* 2004;52(6):1388-1396.

109. Ordidge RJ, Helpern JA, Qing ZX, Knight RA, Nagesh V. Correction of motional artifacts in diffusion-weighted MR images using navigator echoes. *Magn Reson Imaging.* 1994;12(3):455-460.

110. Chen NK, Guidon A, Chang HC, Song AW. A robust multi-shot scan strategy for high-resolution diffusion weighted MRI enabled by multiplexed sensitivity-encoding (MUSE). *Neuroimage.* 2013;72:41-47.

111. Chu ML, Chang HC, Chung HW, Truong TK, Bashir MR, Chen NK. POCS-based reconstruction of multiplexed sensitivity encoded MRI (POCSMUSE): A general algorithm for reducing motion-related artifacts. *Magn Reson Med.* 2015;74(5):1336-1348.

112. Mani M, Jacob M, Kelley D, Magnotta V. Multi-shot sensitivity-encoded diffusion data recovery using structured low-rank matrix completion (MUSSELS). *Magn Reson Med.* 2017;78(2):494-507.

113. Kickingereder P, Burth S, Wick A, Gotz M, Eidel O, Schlemmer HP, et al. Radiomic Profiling of Glioblastoma: Identifying an Imaging Predictor of Patient Survival with Improved Performance over Established Clinical and Radiologic Risk Models. *Radiology.* 2016;280(3):880-889.

114. Zhou M, Scott J, Chaudhury B, Hall L, Goldgof D, Yeom KW, et al. Radiomics in Brain Tumor: Image Assessment, Quantitative Feature Descriptors, and Machine-Learning Approaches. *AJNR Am J Neuroradiol.* 2018;39(2):208-216.

115. Xie Y, Christodoulou AG, Wang N, Li D. Quantitative Multi-Contrast Atherosclerosis Characterization (qMATCH): Comprehensive Quantitative Evaluation of Atherosclerosis in a Single-Scan. *In Proceedings of the 25th Annual Meeting of ISMRM*, Honolulu, HI, 2017. p. 3122.

116. Prakkamakul S, Witzel T, Huang S, Boulter D, Borja MJ, Schaefer P, et al. Ultrafast Brain MRI: Clinical Deployment and Comparison to Conventional Brain MRI at 3T. *J Neuroimaging.* 2016;26(5):503-510.

117. Blystad I, Hakansson I, Tisell A, Ernerudh J, Smedby O, Lundberg P, et al. Quantitative MRI for Analysis of Active Multiple Sclerosis Lesions without Gadolinium-Based Contrast Agent. *AJNR Am J Neuroradiol.* 2016;37(1):94-100.

118. Bonnier G, Marechal B, Fartaria MJ, Falkowskiy P, Marques JP, Simioni S, et al. The Combined Quantification and Interpretation of Multiple Quantitative Magnetic Resonance Imaging Metrics Enlightens Longitudinal Changes Compatible with Brain Repair in Relapsing-Remitting Multiple Sclerosis Patients. *Front Neurol.* 2017;8:506.

119. Manfredonia F, Ciccarelli O, Khaleeli Z, Tozer DJ, Sastre-Garriga J, Miller DH, et al. Normal-appearing brain t1 relaxation time predicts disability in early primary progressive multiple sclerosis. *Arch Neurol.* 2007;64(3):411-415.

120. Tardif CL, Bedell BJ, Eskildsen SF, Collins DL, Pike GB. Quantitative magnetic resonance imaging of cortical multiple sclerosis pathology. *Mult Scler Int.* 2012;2012:742018.

121. Vrenken H, Rombouts SA, Pouwels PJ, Barkhof F. Voxel-based analysis of quantitative T1 maps demonstrates that multiple sclerosis acts throughout the normal-appearing white matter. *AJNR Am J Neuroradiol.* 2006;27(4):868-874.

122. Bartzokis G, Cummings JL, Sultzer D, Henderson VW, Nuechterlein KH, Mintz J. White matter structural integrity in healthy aging adults and patients with Alzheimer disease: a magnetic resonance imaging study. *Arch Neurol.* 2003;60(3):393-398.

123. Knight MJ, McCann B, Tsivos D, Dillon S, Coulthard E, Kauppinen RA. Quantitative T2 mapping of white matter: applications for ageing and cognitive decline. *Phys Med Biol.* 2016;61(15):5587-5605.

124. Luo Z, Zhuang X, Kumar D, Wu X, Yue C, Han C, et al. The correlation of hippocampal T2-mapping with neuropsychology test in patients with Alzheimer's disease. *PLoS One.* 2013;8(9):e76203.

125. Baudrexel S, Nurnberger L, Rub U, Seifried C, Klein JC, Deller T, et al. Quantitative mapping of T1 and T2* discloses nigral and brainstem pathology in early Parkinson's disease. *Neuroimage.* 2010;51(2):512-520.

126. Focke NK, Helms G, Pantel PM, Scheewe S, Knauth M, Bachmann CG, et al. Differentiation of typical and atypical Parkinson syndromes by quantitative MR imaging. *AJNR Am J Neuroradiol.* 2011;32(11):2087-2092.

127. Vymazal J, Righini A, Brooks RA, Canesi M, Mariani C, Leonardi M, et al. T1 and T2 in the brain of healthy subjects, patients with Parkinson disease, and patients with multiple system atrophy: relation to iron content. *Radiology.* 1999;211(2):489-495.

128. Le J, Peng Q, Sperling K. Biochemical magnetic resonance imaging of knee articular cartilage: T1rho and T2 mapping as cartilage degeneration biomarkers. *Ann N Y Acad Sci.* 2016;1383(1):34-42.

129. Li X, Benjamin Ma C, Link TM, Castillo DD, Blumenkrantz G, Lozano J, et al. In vivo T(1rho) and T(2) mapping of articular cartilage in osteoarthritis of the knee using 3 T MRI. *Osteoarthritis Cartilage.* 2007;15(7):789-797.

130. Stahl R, Luke A, Li X, Carballido-Gamio J, Ma CB, Majumdar S, et al. T1rho, T2 and focal knee cartilage abnormalities in physically active and sedentary healthy subjects versus early OA patients--a 3.0-Tesla MRI study. *Eur Radiol.* 2009;19(1):132-143.

131. Witschey WR, Borthakur A, Fenty M, Kneeland BJ, Lonner JH, McArdle EL, et al. T1rho MRI quantification of arthroscopically confirmed cartilage degeneration. *Magn Reson Med.* 2010;63(5):1376-1382.

132. Borthakur A, Sochor M, Davatzikos C, Trojanowski JQ, Clark CM. T1rho MRI of Alzheimer's disease. *Neuroimage.* 2008;41(4):1199-1205.

133. Haris M, Yadav SK, Rizwan A, Singh A, Cai K, Kaura D, et al. T1rho MRI and CSF biomarkers in diagnosis of Alzheimer's disease. *Neuroimage Clin.* 2015;7:598-604.

134. Haris M, Singh A, Cai K, Davatzikos C, Trojanowski JQ, Melhem ER, et al. T1rho (T1rho) MR imaging in Alzheimer's disease and Parkinson's disease with and without dementia. *J Neurol.* 2011;258(3):380-385.

135. Nestrasil I, Michaeli S, Liimatainen T, Rydeen CE, Kotz CM, Nixon JP, et al. T1rho and T2rho MRI in the evaluation of Parkinson's disease. *J Neurol.* 2010;257(6):964-968.

136. Jokivarsi KT, Hiltunen Y, Grohn H, Tuunanen P, Grohn OH, Kauppinen RA. Estimation of the onset time of cerebral ischemia using T1rho and T2 MRI in rats. *Stroke.* 2010;41(10):2335-2340.

137. Mangia S, Carpenter AF, Tyan AE, Eberly LE, Garwood M, Michaeli S. Magnetization transfer and adiabatic T1rho MRI reveal abnormalities in normal-appearing white matter of subjects with multiple sclerosis. *Mult Scler.* 2014;20(8):1066-1073.

138. Andre JB, Bresnahan BW, Mossa-Basha M, Hoff MN, Smith CP, Anzai Y, et al. Toward Quantifying the Prevalence, Severity, and Cost Associated With Patient Motion During Clinical MR Examinations. *J Am Coll Radiol.* 2015;12(7):689-695.

139. Godenschweger F, Kagebein U, Stucht D, Yarach U, Sciarra A, Yakupov R, et al. Motion correction in MRI of the brain. *Phys Med Biol.* 2016;61(5):R32-56.

140. Pipe JG. Motion correction with PROPELLER MRI: application to head motion and free-breathing cardiac imaging. *Magn Reson Med.* 1999;42(5):963-969.

141. Thesen S, Heid O, Mueller E, Schad LR. Prospective acquisition correction for head motion with image-based tracking for real-time fMRI. *Magn Reson Med.* 2000;44(3):457-465.

142. Maclaren J, Herbst M, Speck O, Zaitsev M. Prospective motion correction in brain imaging: a review. *Magn Reson Med.* 2013;69(3):621-636.

143. Bookwalter CA, Griswold MA, Duerk JL. Multiple overlapping k-space junctions for investigating translating objects (MOJITO). *IEEE Trans Med Imaging.* 2010;29(2):339-349.

144. Zaitsev M, Maclaren J, Herbst M. Motion artifacts in MRI: A complex problem with many partial solutions. *J Magn Reson Imaging.* 2015;42(4):887-901.

145. Nezafat R, Stuber M, Ouwerkerk R, Gharib AM, Desai MY, Pettigrew RI. B1-insensitive T2 preparation for improved coronary magnetic resonance angiography at 3 T. *Magn Reson Med.* 2006;55(4):858-864.

146. Brown R, Nguyen TD, Spincemaille P, Cham MD, Choi G, Winchester PA, et al. Effect of blood flow on double inversion recovery vessel wall MRI of the peripheral arteries: quantitation with T2 mapping and comparison with flow-insensitive T2-prepared inversion recovery imaging. *Magn Reson Med.* 2010;63(3):736-744.

147. Mitrea BG, Krafft AJ, Song R, Loeffler RB, Hillenbrand CM. Paired self-compensated spin-lock preparation for improved T1rho quantification. *J Magn Reson.* 2016;268:49-57.

148. Boyd S, Parikh N, Chu E, Peleato B, Eckstein J. Distributed optimization and statistical learning via the alternating direction method of multipliers. *Foundations and Trends® in Machine Learning.* 2011;3(1):1-122.

149. Borthakur A, Wheaton AJ, Gougoutas AJ, Akella SV, Regatte RR, Charagundla SR, et al. In vivo measurement of T1rho dispersion in the human brain at 1.5 tesla. *J Magn Reson Imaging.* 2004;19(4):403-409.

150. Kumar R, Delshad S, Macey PM, Woo MA, Harper RM. Development of T2-relaxation values in regional brain sites during adolescence. *Magn Reson Imaging.* 2011;29(2):185-193.

151. Ma D, Jiang Y, Chen Y, McGivney D, Mehta B, Gulani V, et al. Fast 3D magnetic resonance fingerprinting for a whole-brain coverage. *Magn Reson Med.* 2018;79(4):2190-2197.

152. Okubo G, Okada T, Yamamoto A, Fushimi Y, Okada T, Murata K, et al. Relationship between aging and T1 relaxation time in deep gray matter: A voxel-based analysis. *J Magn Reson Imaging.* 2017;46(3):724-731.

153. Wyatt CR, Smith TB, Sammi MK, Rooney WD, Guimaraes AR. Multi-parametric T2 * magnetic resonance fingerprinting using variable echo times. *NMR Biomed.* 2018;31(9):e3951.

154. Iyer SK, Moon B, Hwuang E, Han YC, Solomon M, Litt H, et al. Accelerated free-breathing 3D T1 cardiovascular magnetic resonance using multicoil compressed sensing. *Journal of Cardiovascular Magnetic Resonance.* 2019;21.

155. Menon RG, Sharafi A, Windschuh J, Regatte RR. Bi-exponential 3D-T1rho mapping of whole brain at 3 T. *Sci Rep.* 2018;8(1):1176.

156. Sharafi A, Xia D, Chang G, Regatte RR. Biexponential T1rho relaxation mapping of human knee cartilage in vivo at 3 T. *NMR Biomed.* 2017;30(10).

157. Witschey WR, Borthakur A, Elliott MA, Fenty M, Sochor MA, Wang C, et al. T1rho-prepared balanced gradient echo for rapid 3D T1rho MRI. *J Magn Reson Imaging.* 2008;28(3):744-754.

158. McPhee KC, Wilman AH. Limitations of skipping echoes for exponential T2 fitting. *J Magn Reson Imaging.* 2018;48(5):1432-1440.

159. Davies GR, Hadjiprocopis A, Altmann DR, Chard DT, Griffin CM, Rashid W, et al. Normal-appearing grey and white matter T1 abnormality in early relapsing-remitting multiple sclerosis: a longitudinal study. *Mult Scler.* 2007;13(2):169-177.

160. Neema M, Goldberg-Zimring D, Guss ZD, Healy BC, Guttmann CR, Houtchens MK, et al. 3 T MRI relaxometry detects T2 prolongation in the cerebral normal-appearing white matter in multiple sclerosis. *Neuroimage.* 2009;46(3):633-641.

161. Hulst HE, Geurts JJ. Gray matter imaging in multiple sclerosis: what have we learned? *BMC Neurol.* 2011;11:153.

162. Klaver R, De Vries HE, Schenk GJ, Geurts JJ. Grey matter damage in multiple sclerosis: a pathology perspective. *Prion.* 2013;7(1):66-75.

163. Pham CH, Tor-Diez C, Meunier H, Bednarek N, Fablet R, Passat N, et al. Multiscale brain MRI super-resolution using deep 3D convolutional networks. *Comput Med Imaging Graph.* 2019;77:101647.

164. Chen Y, Shi F, Christodoulou AG, Xie Y, Zhou Z, Li D. Efficient and accurate MRI super-resolution using a generative adversarial network and 3D multi-level densely connected network. In: International conference on medical image computing and computer-assisted intervention. Springer, Berlin, 2018. pp 91–99.

165. Kuhl C. The current status of breast MR imaging part I. Choice of technique, image interpretation, diagnostic accuracy, and transfer to clinical practice. *Radiology.* 2007;244(2):356-378.

166. Westra C, Dialani V, Mehta TS, Eisenberg RL. Using T2-weighted sequences to more accurately characterize breast masses seen on MRI. *American Journal of Roentgenology.* 2014;202(3):W183-W190.

167. Menezes GL, Knuttel FM, Stehouwer BL, Pijnappel RM, van den Bosch MA. Magnetic resonance imaging in breast cancer: A literature review and future perspectives. *World J Clin Oncol.* 2014;5(2):61-70.

168. Santamaria G, Velasco M, Bargallo X, Caparros X, Farrus B, Luis Fernandez P. Radiologic and pathologic findings in breast tumors with high signal intensity on T2-weighted MR images. *Radiographics.* 2010;30(2):533-548.

169. Liu L, Yin B, Geng DY, Lu YP, Peng WJ. Changes of T2 Relaxation Time From Neoadjuvant Chemotherapy in Breast Cancer Lesions. *Iran J Radiol.* 2016;13(3):e24014.

170. Chu W, Jin W, Liu D, Wang J, Geng C, Chen L, et al. Diffusion-weighted imaging in identifying breast cancer pathological response to neoadjuvant chemotherapy: A meta-analysis. *Oncotarget.* 2018;9(6):7088-7100.

171. Partridge SC, Zhang Z, Newitt DC, Gibbs JE, Chenevert TL, Rosen MA, et al. Diffusion-weighted MRI Findings Predict Pathologic Response in Neoadjuvant Treatment of Breast Cancer: The ACRIN 6698 Multicenter Trial. *Radiology.* 2018;289(3):618-627.

172. Baltzer PA, Benndorf M, Dietzel M, Gajda M, Camara O, Kaiser WA. Sensitivity and specificity of unenhanced MR mammography (DWI combined with T2-weighted TSE imaging, ueMRM) for the differentiation of mass lesions. *Eur Radiol.* 2010;20(5):1101-1110.

173. Yabuuchi H, Matsuo Y, Sunami S, Kamitani T, Kawanami S, Setoguchi T, et al. Detection of non-palpable breast cancer in asymptomatic women by using unenhanced diffusion-weighted and T2-weighted MR imaging: comparison with mammography and dynamic contrast-enhanced MR imaging. *Eur Radiol.* 2011;21(1):11-17.

174. Pineda FD, Medved M, Fan X, Karczmar GS. B1 and T1 mapping of the breast with a reference tissue method. *Magn Reson Med.* 2016;75(4):1565-1573.

175. Sung K, Daniel BL, Hargreaves BA. Transmit B1+ field inhomogeneity and T1 estimation errors in breast DCE-MRI at 3 tesla. *J Magn Reson Imaging.* 2013;38(2):454-459.

176. Tsai WC, Kao KJ, Chang KM, Hung CF, Yang Q, Lin CE, et al. B1 Field Correction of T1 Estimation Should Be Considered for Breast Dynamic Contrast-enhanced MR Imaging Even at 1.5 T. *Radiology.* 2017;282(1):55-62.

177. Azlan CA, Di Giovanni P, Ahearn TS, Semple SI, Gilbert FJ, Redpath TW. B1 transmission-field inhomogeneity and enhancement ratio errors in dynamic contrast-enhanced MRI (DCE-MRI) of the breast at 3T. *J Magn Reson Imaging.* 2010;31(1):234-239.

178. Kuhl CK, Kooijman H, Gieseke J, Schild HH. Effect of B1 inhomogeneity on breast MR imaging at 3.0 T. *Radiology.* 2007;244(3):929-930.

179. Chung S, Kim D, Breton E, Axel L. Rapid B1+ mapping using a preconditioning RF pulse with TurboFLASH readout. *Magn Reson Med.* 2010;64(2):439-446.

180. Edden RA, Smith SA, Barker PB. Longitudinal and multi-echo transverse relaxation times of normal breast tissue at 3 Tesla. *J Magn Reson Imaging.* 2010;32(4):982-987.

181. Serry FM MS, Li D, Christodoulou AG. Dual Flip-Angle IR-FLASH for B1+ Insensitive T1 Mapping: Application to T1 CMR Multitasking. *In Proceedings of the 28th Annual Meeting of ISMRM*, *Virtual Exhibition*, 2020.

182. Han Y, Liimatainen T, Gorman RC, Witschey WR. Assessing Myocardial Disease Using T1rho MRI. *Curr Cardiovasc Imaging Rep.* 2014;7(2):9248.

183. Witschey WR, Zsido GA, Koomalsingh K, Kondo N, Minakawa M, Shuto T, et al. In vivo chronic myocardial infarction characterization by spin locked cardiovascular magnetic resonance. *J Cardiovasc Magn Reson.* 2012;14:37.

184. Kellman P, Aletras AH, Mancini C, McVeigh ER, Arai AE. T2-prepared SSFP improves diagnostic confidence in edema imaging in acute myocardial infarction compared to turbo spin echo. *Magn Reson Med.* 2007;57(5):891-897.

185. Berisha S, Han J, Shahid M, Han Y, Witschey WR. Measurement of Myocardial T1rho with a Motion Corrected, Parametric Mapping Sequence in Humans. *PLoS One.* 2016;11(3):e0151144.

186. Kvernby S, Warntjes MJ, Haraldsson H, Carlhall CJ, Engvall J, Ebbers T. Simultaneous three-dimensional myocardial T1 and T2 mapping in one breath hold with 3D-QALAS. *J Cardiovasc Magn Reson.* 2014;16:102.

187. Piechnik SK, Ferreira VM, Dall'Armellina E, Cochlin LE, Greiser A, Neubauer S, et al. Shortened Modified Look-Locker Inversion recovery (ShMOLLI) for clinical myocardial T1-mapping at 1.5 and 3 T within a 9 heartbeat breathhold. *J Cardiovasc Magn Reson.* 2010;12:69.

188. Qi H, Bustin A, Kuestner T, Hajhosseiny R, Cruz G, Kunze K, et al. Respiratory motion-compensated high-resolution 3D whole-heart T1rho mapping. *J Cardiovasc Magn Reson.* 2020;22(1):12.

189. Jaubert O, Cruz G, Bustin A, Schneider T, Koken P, Doneva M, et al. Free-running cardiac magnetic resonance fingerprinting: Joint T1/T2 map and Cine imaging. *Magn Reson Imaging.* 2020;68:173-182.

190. Kellman P, Hansen MS. T1-mapping in the heart: accuracy and precision. *J Cardiovasc Magn Reson.* 2014;16:2.

191. Roujol S, Weingartner S, Foppa M, Chow K, Kawaji K, Ngo LH, et al. Accuracy, precision, and reproducibility of four T1 mapping sequences: a head-to-head comparison of MOLLI, ShMOLLI, SASHA, and SAPPHIRE. *Radiology.* 2014;272(3):683-689.

192. Ma S, Christodoulou AG, Wang N, Kaisey M, Sicotte NL, Li D. Motion-Resolved, 3D Whole-Brain Simultaneous T1, T2, and T1ρ Mapping using Multitasking with Application to Multiple Sclerosis: A Pilot Study. *ISMRM.* 2020.

193. Ma S, Wang N, Christodoulou AG, Li D. Rapid 3D B1+-Compensated, Simultaneous Whole Breast T1, T2, and Apparent Diffusion Coefficient Quantification with MR Multitasking. *In Proceedings of the 28th Annual Meeting of ISMRM*, *Virtual Exhibition*, 2020.

194. Nguyen C, Sharif-Afshar AR, Fan Z, Xie Y, Wilson S, Bi X, et al. 3D high-resolution diffusion-weighted MRI at 3T: Preliminary application in prostate cancer patients undergoing active surveillance protocol for low-risk prostate cancer. *Magn Reson Med.* 2016;75(2):616-626.

195. Wang N, Christodoulou, AG, Xie Y, Han F, Zhong X, Ma S, Bi X, Deshpande V, Li D. Three-Dimensional Free-breathing Whole-Liver Simultaneous T1, R2*, and Fat-Fraction Quantification Using MR Multitasking. *In Proceedings of the 28th Annual Meeting of ISMRM*, *Virtual Exhibition*, 2020.

196. Cao T, Christodoulou, AG, Wang N, Ma S, Xie Y, Gharabaghi S, Haacke EM, Li D. Simultaneous Quantitative Mapping of T1, T2*, and Susceptibility with Magnetic Resonance Multitasking. *In Proceedings of the 28th Annual Meeting of ISMRM*, *Virtual Exhibition*, 2020.

197. Breuer FA, Blaimer M, Heidemann RM, Mueller MF, Griswold MA, Jakob PM. Controlled aliasing in parallel imaging results in higher acceleration (CAIPIRINHA) for multi-slice imaging. *Magn Reson Med.* 2005;53(3):684-691.

198. Breuer FA, Blaimer M, Mueller MF, Seiberlich N, Heidemann RM, Griswold MA, et al. Controlled aliasing in volumetric parallel imaging (2D CAIPIRINHA). *Magn Reson Med.* 2006;55(3):549-556.

199. Griswold MA, Jakob PM, Heidemann RM, Nittka M, Jellus V, Wang J, et al. Generalized autocalibrating partially parallel acquisitions (GRAPPA). *Magn Reson Med.* 2002;47(6):1202-1210.

200. Griswold MA, Jakob PM, Nittka M, Goldfarb JW, Haase A. Partially parallel imaging with localized sensitivities (PILS). *Magn Reson Med.* 2000;44(4):602-609.

201. Jakob PM, Griswold MA, Edelman RR, Sodickson DK. AUTO-SMASH: a self-calibrating technique for SMASH imaging. SiMultaneous Acquisition of Spatial Harmonics. *MAGMA.* 1998;7(1):42-54.

202. Pruessmann KP, Weiger M, Scheidegger MB, Boesiger P. SENSE: sensitivity encoding for fast MRI. *Magn Reson Med.* 1999;42(5):952-962.

203. Sodickson DK, Manning WJ. Simultaneous acquisition of spatial harmonics (SMASH): fast imaging with radiofrequency coil arrays. *Magn Reson Med.* 1997;38(4):591-603.

204. Uecker M, Lai P, Murphy MJ, Virtue P, Elad M, Pauly JM, et al. ESPIRiT--an eigenvalue approach to autocalibrating parallel MRI: where SENSE meets GRAPPA. *Magn Reson Med.* 2014;71(3):990-1001.

205. Hammernik K, Klatzer T, Kobler E, Recht MP, Sodickson DK, Pock T, et al. Learning a variational network for reconstruction of accelerated MRI data. *Magn Reson Med.* 2018;79(6):3055-3071.

206. Hyun CM, Kim HP, Lee SM, Lee S, Seo JK. Deep learning for undersampled MRI reconstruction. *Phys Med Biol.* 2018;63(13):135007.

207. Kwon K, Kim D, Park H. A parallel MR imaging method using multilayer perceptron. *Med Phys.* 2017;44(12):6209-6224.

208. Lee DY, J.; Ye, JC. Deep residual learning for compressed sensing MRI. *IEEE 14th International Symposium on Biomedical Imaging.* 2017.

209. Tamada D. Review: Noise and artifact reduction for MRI using deep learning. *arXiv.* 2020.